Fluid Inclusion Characteristics in Magmatic-Hydrothermal Ore Deposits

Stephen P. Becker

Dissertation submitted to the faculty of the Virginia Polytechnic Institute and State University in partial fulfillment of the requirement for the degree of

Doctor of Philosophy in Geosciences

Committee
Robert J. Bodnar, chair
J. Donald Rimstidt
Robert J. Tracy
James J. Student

July 5, 2007
Blacksburg, VA

Keywords:(fluid inclusions, phase equilibria, PVTX properties, experimental, magmatic-hydrothermal, ore deposits)

Fluid Inclusion Characteristics in Magmatic-Hydrothermal Ore Deposits

Stephen P. Becker

ABSTRACT

Magmatic-hydrothermal ore deposits are formed in association with aqueous fluids that exsolve from hydrous silicate melts during ascent and crystallization. These fluids are invariably trapped as inclusions in vein-filling minerals associated with hydrothermal fluid flow, and their composition may be modeled based on the H_2O-NaCl system. Thus, if we know the pressure-volume-temperature-composition (PVTX) properties of H_2O-NaCl solutions, it is possible to interpret the PTX trapping conditions, which is important for understanding the processes leading to the generation of the hydrothermal system and ore mineralization.

High salinity (> 26 wt. % NaCl) fluid inclusions contain liquid, vapor, and halite at room temperature, and are common in magmatic-hydrothermal ore deposits. These inclusions homogenize in one of three ways: A) halite disappearance (Tm_{halite}) followed by liquid-vapor homogenization (Th_{L-V}), B) simultaneous Th_{L-V} and Tm_{halite}, or C) Th_{L-V} followed by Tm_{halite}. The PVTX properties of H_2O-NaCl solutions three phase (L+V+H) and liquid-vapor (L+V) phase boundaries are well constrained, allowing researchers to interpret the minimum trapping pressure of inclusion types A and B. However, data that describe the pressure at Tm_{halite} for inclusion type C are limited to a composition of 40 wt. % NaCl. To resolve this problem, the synthetic fluid inclusion technique was used to determine the relationship between homogenization temperature and minimum trapping pressure for inclusions that homogenize by mode C. These results allow researchers to interpret the minimum trapping pressure of these inclusions, and by extension the depth at which the inclusions formed.

The temporal and spatial distribution of fluid inclusions formed in associated with porphyry copper mineralization has been predicted using a computer model. A simple geologic model of an epizonal intrusion was developed based on a Burnham-style model for porphyry systems and thermal models of the evolution of epizonal intrusions. The phase stability fields and fluid inclusion characteristics at any location and time were predicted based on PVTX properties of H_2O-NaCl solutions. These results provide vectors towards the center of a magmatic-hydrothermal system that allow explorationists to use fluid inclusion petrography to predict position with the overall porphyry environment when other indicators of position are absent.

Acknowledgements

This research would not have been possible without help and support from many people during my time at Virginia Tech. First, I thank my advisor, Dr. Robert J. Bodnar for providing me the opportunity to work with him during the past four years. I am very grateful for his support and for the experience and knowledge I have gained with application to working with fluid inclusions. I also thank him for suggesting projects and for being patient at times while I worked around family issues associated with the birth of my son.

I also thank the other members of my committee for their support and for discussions that improved the quality of my research: J. Donald Rimstidt, Robert J. Tracy, and James J. Student.

The departmental staff has been very helpful, and it would not be possible to survive here without them. In particular, I thank Charles Farley for his assistance with my hydrothermal experiments and other equipment. It seems like the equipment was held together by chewing gum and duct tape at times, but he always kept it working. The office staff members kept me up to date on all of the paperwork, were willing to listen to problems and were always helpful and friendly. They are really the people behind the scenes that keep everything running smoothly, and I thank them for all of their hard work.

My fellow graduate students have made life in Blacksburg fun, including the weekly basketball games at War Memorial Hall, and out having beers at the local watering holes. In particular, I thank the current and former members of the fluids research group: Tristan Azbej, Andras Fall, Fang Lin, Megan Elwood-Madden, Rocky Severs, Claudia Cannatelli, Rosario Esposito, Daniel Moncada, and Max Rolandi.

I especially thank my wife, Kris, for her nearly infinite patience and willingness to continue to live the graduate student life for four more years. She has been wonderful wife, and an even better mother to our son Tim for the past two and a half years.

Finally, I thank my family back in Missouri for their encouragement and support. I greatly appreciate everything they have done for me and my family here in Blacksburg.

Table of Contents

List of Tables

Chapter 2:

List of Figures

Chapter 2:

Chapter 3:

Chapter 1: Introduction

Magmatic-hydrothermal ore deposits are important sources of metals that help supply the world with the resources required to sustain industrial and technological applications. As current reserves are extracted, new resources must be discovered. At the same time, the discovery of new prospects is limited by our understanding of the geological systems that concentrate metals in the crust of the earth. If we are able to improve our knowledge of these systems, exploration strategies may be modified to maximize our chances to discover new prospects.

The geology of magmatic-hydrothermal systems, including porphyry copper deposits, is well constrained in most cases. However, the characteristics of associated fluids are not always understood, often limited by a lack of experimental data that describe the pressure-volume-temperature-composition (PVTX) characteristics of the fluids. During ascent and crystallization of a hydrous magma, aqueous fluid phase separation results in a hydrothermal system responsible for ore mineralization (Burnham, 1997). The ability to determine the PTX characteristics of the fluids responsible for mineralization is necessary to improve our understanding of the processes that lead to economic mineralization, as well as understanding the significance of certain geological characteristics of the system. For example, knowing the pressure of a system is particularly useful in exploration, as this constrains the depth of formation. However, the depth of formation is one aspect of hydrothermal systems that involves much uncertainty (Skinner, 1997).

Fluid Inclusions, PVTX Properties of Fluids, and the Evolution of Magmatic-Hydrothermal Systems

Aqueous fluids that exsolve from a silicate melt phase are invariably trapped as inclusions in phenocrysts and fracture-filling cements (Bodnar, 1995; Roedder, 1984). These fluid inclusions allow researchers to study and understand magmatic-hydrothermal systems, providing direct evidence of the PTX characteristics of the system at the instant in time that the inclusions were trapped. Studying inclusions using basic petrographic techniques makes it possible to describe the PTX evolution of the system in time and space. However, the interpretation of inclusions relies on our current knowledge of the phase equilibria of

geologically relevant fluids. Aqueous fluids of magmatic origin are moderately to highly saline as a consequence of the partitioning behavior of chlorine between melt and magmatic fluid (Cline and Bodnar, 1991; Kilinc and Burnham, 1972; Shinohara et al., 1989). Thus, the composition of magmatic fluids can be adequately modeled by the behavior of simple water-salt solutions, such as H_2O-NaCl. Many previous experimental (Bischoff, 1991; Bischoff and Pitzer, 1989; Bodnar, 1985, 1994; Bodnar and Vityk, 1994; Haar et al., 1984; Haas, 1976; Keevil, 1942; National Research Council, 1928; Palliser and McKibbin, 1998a, b; Pitzer and Pabalan, 1986; Potter, 1977; Sourirajan and Kennedy, 1962; Sterner et al., 1988) and theoretical (Anderko and Pitzer, 1993; Duan et al., 2003; Kosinski and Anderko, 2001) descriptions of the H_2O-NaCl system provide a basis to interpret the PTX properties of most fluid inclusions, although there are some situations where further experimental data would improve our ability to interpret certain types of inclusions, such as those that homogenize along the halite liquidus (Bodnar, 1994; Klevtsov and Lemmlein, 1959; Lemmlein and Klevtsov, 1961; Lyakhov, 1973; Roedder and Bodnar, 1980).

In addition to the phase equilibrium studies described above, a number of previous hydrothermal fluid-flow modeling studies predict the temporal and spatial thermal evolution of magmatic-hydrothermal systems (Cathles, 1977, 1981; Hayba and Ingebritsen, 1997; Knapp and Norton, 1981; Norton and Knight, 1977; Norton, 1982; Norton, 1984). Also, data from geochemical modeling (Cline and Bodnar, 1991; Kilinc and Burnham, 1972; Shinohara et al., 1989) and natural fluid inclusions (e.g. Hedenquist et al., 1998) provide constraints on the compositions of magmatic-derived aqueous fluids. Thus, experimental and theoretical phase equilibrium data allow us to interpret natural fluid inclusions and make it possible to develop predictive models of the characteristics of fluids associated with a magmatic-hydrothermal system during its thermal evolution.

Research Summary

In the following chapters, characteristics of fluid inclusions in magmatic-hydrothermal ore deposits are explored using experimental geochemistry and computer modeling based on available PVTX data. These related studies improve our current understanding of the fluids associated with magmatic-hydrothermal ore deposits, and may be used to improve exploration strategies. In Chapter 2, the origin and interpretation of high

salinity fluid inclusions that homogenize by halite disappearance are discussed in detail. Owing to a lack of appropriate experimental data, except for a composition of 40 wt. % NaCl (Bodnar, 1994), it was previously not possible to accurately interpret the minimum trapping pressures of such inclusions. Using the synthetic fluid inclusion technique to determine a relationship between trapping pressure and homogenization temperature, it is now possible to interpret data from this inclusion type and to infer a depth of formation. However, it has also become apparent that many inclusions that homogenize by halite disappearance often do not obey "Roedder's Rules" (Bodnar, 2003a; Roedder, 1984), which in most cases precludes the use of such inclusions to interpret the PTX history of a system.

In Chapter 3, a model for the temporal and spatial distribution of fluid inclusions in a simple porphyry-copper system is presented. This model is based on a combination of available PVTX data for the H_2O-NaCl system and fluid-flow studies that describe the thermal history of epizonal intrusions. These data were used to develop "maps" of the phase stability regions on a cross-section of a basic porphyry model. This information was then used to predict the types and characteristics of fluid inclusions that would be trapped during the magmatic stage of the porphyry system that is primarily associated with ore-forming fluids. This model may be used to conduct exploration activities in areas where other indicators of position in the overall porphyry environment, such as alteration zones, are not useful. This study also has implications for the association of certain types of fluids with alteration zones at different stages of the evolution of the magmatic system, such as acid alteration in shallow plutons, and late phyllic alteration in some deposits.

Together these two studies advance our understanding of the evolution of saline fluids released from crystallizing magmas. Because these fluids are responsible for the formation of economically important ore deposits, this knowledge will improve our ability to locate and exploit these important sources of metals.

References

Anderko, A., and Pitzer, K. S., 1993, Equation-of-state representation of phase equilibria and volumetric properties of the system NaCl-H_2O above 573 K: Geochimica et Cosmochimica Acta, v. 57, p. 1657-1680.

Bischoff, J. L., 1991, Densities of Liquids and Vapors in Boiling NaCl-H_2O Solutions: a PVTX summary from 300° to 500°C: American Journal of Science, v. 291, p. 309-338.

Bischoff, J. L., and Pitzer, K. S., 1989, Liquid-Vapor Relations for the System NaCl-H_2O: Summary of the P-T-x Surface from 300° to 500°C: American Journal of Science, v. 289, p. 217-248.

Bodnar, R. J., 1985, Pressure-Volume-Temperature-Composition (PVTX) properties of the system H_2O-NaCl at elevated temperatures and pressures: Unpub. PhD Dissertation thesis, The Pennsylvania State University, 183 p.

Bodnar, R. J., 1994, Synthetic fluid inclusions. XII. Experimental determination of the liquidus and isochores for a 40 wt.% H_2O-NaCl solution: Geochimica et Cosmochimica Acta, v. 58, p. 1053-1063.

Bodnar, R. J., 1995, Fluid inclusion evidence for a magmatic source for metals in porphyry copper deposits, *in* Thompson, J. F. H., ed., Mineralogical Association of Canada Short Course Volume 23, 23, p. 139-152.

Bodnar, R. J., 2003, Introduction to fluid inclusions, *in* Samson, I., Anderson, A., and Marshall, D., eds., Fluid Inclusions: Analysis and Interpretation, Short Course 32, 32, Mineralogical Association of Canada, p. 1-8.

Bodnar, R. J., Burnham, C. W., and Sterner, S. M., 1985, Synthetic fluid inclusions in natural quartz. III. Determination of phase equilibrium properties in the system H_2O-NaCl to 1000°C and 1500 bars.: Geochimica et Cosmochimica Acta, v. 49, p. 1861-1873.

Bodnar, R. J., and Vityk, M. O., 1994, Interpretation of microthermometric data for H_2O-NaCl fluid inclusions, *in* de Vivo, B., and Frezzotti, M. L., eds., Fluid Inclusions in Minerals, Methods and Applications: Blacksburg, VA, Virginia Tech, p. 117-130.

Burnham, C. W., 1997, Magmas and hydrothermal fluids, *in* Barnes, H. L., ed., Geochemistry of Hydrothermal Ore Deposits: New York, Wiley and Sons, p. 63-123.

Cathles, L. M., 1977, An analysis of the cooling of intrusives by ground-water convection which includes boiling: Economic Geology, v. 72, p. 804-826.

Cathles, L. M., 1981, Fluid flow and genesis of hydrothermal ore deposits: Economic Geology, v. 75th Anniversary, p. 424-457.

Cline, J. S., and Bodnar, R. J., 1991, Can economic porphyry copper mineralization be generated by a typical calc-alkaline melt?: Journal of Geophysical Research, v. 96, p. 8113-8126.

Duan, Z., Moller, N., and Weare, J. H., 2003, Equations of state for the NaCl-H_2O-CH_4 system and the NaCl-H_2O-CO_2-CH_4 system; phase equilibria and volumetric properties above 573 K: Geochimica et Cosmochimica Acta, v. 67, p. 671-680.

Haar, L., Gallagher, J. S., and Kell, G. S., 1984, NBS/NRC Steam Tables: Thermodynamic and Transport Properties and Computer Programs for Vapor and Liquid States of Water in SI Units, Hemisphere Publishing Corporation.

Haas, J. L. J., 1976, Physical Properties of the Coexisting Phases and Thermochemical Properties of the H_2O Component in Boiling NaCl Solutions: Geological Survey Bulletin, v. 1421-A, p. 73pp.

Hayba, D. O., and Ingebritsen, S. E., 1997, Multiphase groundwater flow near cooling plutons: Journal of Geophysical Research, v. 102, p. 12235-12252.

Hedenquist, J. W., Arribas, A., Jr., and Reynolds, T. J., 1998, Evolution of an Intrusion-Centered Hydrothermal System: Far Southeast-Lepanto Porphyry and Epithermal Cu-Au Deposits, Philippines: Economic Geology, v. 93, p. 373-404.

Keevil, N. B., 1942, Vapor Pressures of Aqueous Solutions at High Temperatures: American Chemical Society Journal, v. 64, p. 841-850.

Kilinc, I. A., and Burnham, C. W., 1972, Partitioning of Chloride Between a Silicate Melt and Coexisting Aqueous Phase from 2 to 8 Kilobars: Economic Geology, v. 67, p. 231-235.

Klevtsov, P. V., and Lemmlein, G. G., 1959, Determination of the minimum pressure of quartz formation as exemplified by crystals from the Pamir: Zap. Vses. Mineral. Obshch., v. 85, p. 661-666.

Knapp, R. B., and Norton, D., 1981, Preliminary Numerical Analysis of Processes Related to Magma Crystallization and Stress Evolution in Cooling Pluton Environments: American Journal of Science, v. 281, p. 35-68.

Kosinski, J. J., and Anderko, A., 2001, Equation of state for high-temperature aqueous electrolyte and nonelectrolyte systems.: Fluid Phase Equilibria, v. 183-184, p. 75-86.

Lemmlein, G. G., and Klevtsov, P. V., 1961, Relations among the principle thermodynamic parameters in a part of the system H_2O-NaCl: Geochemistry, v. 2, p. 148-158.

Lyakhov, Y. V., 1973, Errors in determining pressure of mineralization from gas-liquid inclusions with halite, their causes and ways of eliminating them: Zap. Vses. Mineral. Obshch., v. 102, p. 385-393.

National Research Council, 1928, International critical tables of numerical data, physics, chemistry, and technology: New York, McGraw-Hill, 444 p.

Norton, D., and Knight, J., 1977, Transport Phenomena in Hydrothermal Systems: Cooling Plutons: American Journal of Science, v. 277, p. 937-981.

Norton, D. L., 1982, Fluid and heat transport phenomena typical of copper-bearing pluton environments, *in* Titley, S. R., ed., Advances in Geology of the Porphyry Copper Deposits: Tucson, AZ, University of Arizona Press.

Norton, D. L., 1984, Theory of Hydrothermal Systems: Annual Reviews of Earth and Planetary Science, v. 12, p. 155-177.

Palliser, C., and McKibbin, R., 1998a, A model for deep geothermal brines; I, T-p-X state-space description: Transport in Porous Media, v. 33, p. 65-80.

Palliser, C., and McKibbin, R., 1998b, A model for deep geothermal brines; II, Thermodynamic properties, density: Transport in Porous Media, v. 33, p. 129-154.

Pitzer, K. S., and Pabalan, R. T., 1986, Thermodynamics of NaCl in steam: Geochimica et Cosmochimica Acta, v. 50, p. 1445-1454.

Potter, R. W. I., 1977, Pressure Corrections for Fluid Inclusion Homogenization Temperatures Based on the Volumetric Properties of the System NaCl-H_2O: Journal Research U.S. Geological Survey, v. 5, p. 603-607.

Roedder, E., 1984, Fluid Inclusions, *in* Ribbe, P. H., ed., Reviews in Mineralogy, 12: Washington, D.C., Mineralogical Society of America, p. 644.

Roedder, E., and Bodnar, R. J., 1980, Geologic pressure determinations from fluid inclusion studies: Annual Review of Earth and Planetary Sciences, v. 8, p. 263-301.

Shinohara, H., Iiyama, J. T., and Matsuo, S., 1989, Partition of chlorine compounds between silicate melt and hydrothermal solutions; I, Partition of NaCl-KCl: Geochimica et Cosmochimica Acta, v. 53, p. 2617-2630.

Skinner, B. J., 1997, Hydrothermal mineral deposits: What we do and don't know, *in* Barnes, H. L., ed., Geochemistry of Hydrothermal Ore Deposits: New York, Wiley & Sons, p. 1-29.

Sourirajan, S., and Kennedy, G. C., 1962, The system H_2O-NaCl at elevated temperatures and pressures: American Journal of Science, v. 260, p. 115-141.

Sterner, S. M., Hall, D. L., and Bodnar, R. J., 1988, Synthetic fluid inclusions. V. Solubility relations in the system NaCl-KCl-H_2O under vapor-saturated conditions: Geochimica et Cosmochimica Acta, v. 52, p. 989-1006.

Chapter 2: Synthetic Fluid Inclusions. XIX. PVTX properties of high salinity H_2O-NaCl solutions (>30 wt. % NaCl), with application to inclusions that homogenize along the halite liquidus

Stephen P. Becker and Robert J. Bodnar
Fluids Research Laboratory, Department of Geosciences
Virginia Tech, Blacksburg, Virginia 24061, USA

Abstract

The relationship between liquid-vapor homogenization (Th_{L-V}), halite dissolution temperature (Tm_{halite}) and pressure has been determined using synthetic H_2O-NaCl fluid inclusions that homogenize by halite disappearance. The experimental data cover the range $Th_{L-V} \approx 150°$-$500°C$ and $Tm_{halite} \approx 275°$-$550°C$. An empirical equation describing the relationship between pressure, Th_{L-V}, and Tm_{halite} has been developed to estimate formation pressures from microthermometric data, and is valid from pressures along the liquid + vapor + halite curve to 300 MPa.

A detailed literature review reveals that the results of this study cannot be applied retroactively to estimate pressures of previously reported inclusions that homogenize by halite dissolution for several reasons. Most workers have not collected and reported the data following the Fluid Inclusion Assemblage methodology described by Goldstein and Reynolds. Thus, it is not possible to determine if the inclusions show consistent microthermometric behavior within a group of coeval inclusions. Additionally, many published studies provide only summaries of results from numerous samples or present the data graphically, precluding application of our results to individual inclusions. However, based on our review of the published results, it appears that much of the published data for inclusions that homogenize by halite dissolution represents inclusions that have either trapped a halite crystal along with the liquid, or have reequilibrated by necking and/or stretching.

Results from this study have been used to estimate minimum formation pressures for inclusions from the Ditrau Alkaline Massif, Transylvania, Romania; Musoshi stratiform copper deposit, Zaire (now DRC); Bismark skarn deposit, northern Mexico; Naica chimney-manto deposit, Mexico; and the Questa porphyry molybdenum deposit, New Mexico. In each case, pressures estimated using results from the present study are in good agreement with previous pressure estimates. However, in some cases estimated pressures (both our estimates as well as those of other authors) appear to be unreasonably high based on the geological setting at the time of formation. These results highlight the need for improved methods for estimating pressure in ore-forming systems.

Introduction

Halite-bearing fluid inclusions are common in many geologic environments, and are essentially ubiquitous in shallow silicic plutons such as those associated with porphyry copper deposits (Bodnar, 1995). Halite-bearing inclusions may display three different modes of homogenization during heating from room temperature: A) halite dissolution (Tm_{halite}) followed by liquid-vapor homogenization ($Th_{L\text{-}V}$), B) simultaneous $Th_{L\text{-}V}$ and Tm_{halite}, or C) $Th_{L\text{-}V}$ followed by Tm_{halite} (Fig. 1). Fluid inclusion researchers use microthermometric data from halite-bearing inclusions to estimate fluid compositions and temperatures of formation of the inclusions (Roedder, 1984). Compositions and trapping pressures can be estimated with reasonable precision (and accuracy) for inclusions that homogenize via modes "A" and "B" because experimental (Bischoff and Pitzer, 1989; Bodnar, 1992; Bodnar et al., 1985; Haas, 1976; Sterner et al., 1988) and theoretical (Anderko and Pitzer, 1993; Bischoff and Pitzer, 1989) PVTX data are available for the vapor-saturated halite solubility curve and the liquid-vapor surfaces for the system H_2O-NaCl. However, mode "C" inclusions homogenize along the halite liquidus and traverse the liquid + halite field after the vapor bubble disappears. PVTX data along the halite liquidus and in the liquid + halite field are only available for a composition of 40 wt. % NaCl (Bodnar, 1994). For other compositions, the pressure in the inclusion at homogenization and the inclusion composition cannot be estimated with a high degree of certainty from microthermometric data.

As noted above, inclusions that homogenize by halite disappearance are nearly ubiquitous in porphyry copper deposits. Owing to this, much effort has been devoted to understanding the P-T formation conditions of these inclusions (Klevtsov and Lemmlein, 1959; Lemmlein and Klevtsov, 1961; Lyakhov, 1973; Roedder and Bodnar, 1980). Klevtsov and Lemmlein (1959) and Lemmlein and Klevtsov (1961) assumed that the slope of the isochore in the two-phase (liquid+halite) field was the same as the slope in the one-phase (liquid) field. Based on this assumption, they estimated an internal pressure of 1100 bars for an inclusion with $Th_{L\text{-}V} = 310°C$ and $Tm_{halite} = 400°C$ (Fig. 2). Lyakhov (1973) assumed a much steeper P-T path in the two-phase field, compared to the one-phase field, resulting in an inferred trapping pressure of 5000 bars for an inclusion with this same homogenization behavior. Roedder and Bodnar (1980) noted pressure determinations summarized above

(particularly the Lyakhov value) appeared to be inconsistent with geological evidence for a shallow crustal origin for most porphyry copper mineralization. These workers introduced a third method to estimate the internal pressure using limited PVTX data that were available at the time. When applied to the same inclusion ($Th_{L\text{-}V}$ = 310°C and Tm_{halite} = 400°C), Roedder and Bodnar estimated an internal pressure at homogenization of 650 bars (Fig. 2).

The significance and interpretation of inclusions that homogenize by halite disappearance remains a topic of discussion within the fluid inclusion community, as evidenced by a discussion on the fluid inclusion listserv (see http://www.geology.wisc.edu/flincs/fi/disc/salinity.html). Type "C" inclusions are especially important for understanding the genesis of porphyry copper deposits, as trapping pressure is directly related to depth of formation. Thus, our ability to determine trapping conditions has implications for emplacement depths and genetic models for porphyry copper deposits. These uncertainties in turn affect exploration strategies in the search for new deposits. In this paper we present new experimental PVTX data for the system H_2O-NaCl. These data can be used to estimate trapping pressures for inclusions that homogenize by halite disappearance, and have been applied to estimate trapping pressure of type "C" inclusions from several ore-forming systems.

Trapping Conditions and Microthermometric Behavior of Halite-bearing Inclusions

Figure 2 is a schematic P-T projection of the H_2O-NaCl system for some salinity greater than about 26.4 wt. % NaCl, which represents the solubility of NaCl in H_2O at room temperature (Bodnar et al. 1985). That is, any H_2O-NaCl fluid inclusion with a salinity greater than the solubility of NaCl at room temperature is likely to contain a halite daughter mineral at room temperature. In practice, however, inclusions with salinities less than about 30 wt. % NaCl usually remain as metastable, supersaturated liquids and do not precipitate a halite crystal.

Isochore "B" (Fig. 2) for this composition intersects the three-phase (liquid+vapor+halite; L+V+H; Fig. 2) curve at the point at which the halite liquidus for this same composition intersects the three-phase curve. Inclusions trapped along this isochore will homogenize by the simultaneous disappearance of vapor and halite, as shown by inclusion "B" on Figure 1. During heating from room temperature (B1; Fig. 2) a type "B"

inclusion will follow the vapor-saturated halite solubility curve (L+V+H) to homogenization at point “B2”, where the halite crystal and vapor bubble disappear simultaneously (Fig 1; heating sequence “B”). If the inclusion is heated beyond the homogenization temperature, the P-T conditions within the inclusion will follow isochore “B” into the one-phase liquid field.

Inclusions trapped in field “A” (Fig. 2) will homogenize via mode “A”, whereby the halite crystal disappears first, followed by liquid-vapor homogenization at some higher temperature (Fig. 1; heating sequence “A”). Fluid inclusions trapped anywhere in field “A”, which is bounded by isochore “B” and the liquid-vapor curve corresponding to the bulk composition of the inclusion, will homogenize via mode “A”. During heating from room temperature (A1), a type “A” inclusion will follow the vapor-saturated halite solubility (three-phase curve; L+V+H) curve to point “A2”, at which point the halite crystal disappears. Point A2 is defined by the intersection of the halite liquidus with the L+V+H curve. With continued heating the inclusion will follow the liquid-vapor curve until the bubble disappears at point “A3”. If the inclusion is heated beyond the homogenization temperature, the P-T conditions within the inclusion will follow isochore “A” into the one-phase liquid field.

Inclusions trapped in field “C” will homogenize via mode “C”, whereby the vapor bubble disappears before the halite crystal dissolves (heating sequence “C”; Fig. 1). Field “C” is bounded by isochore “B” and the halite liquidus (Fig. 2). During heating from room temperature (C1; Fig. 2), a type “C” inclusion will follow the vapor-saturated halite solubility (L+V+H) curve to temperature “C2” (Fig. 2), at which point the vapor bubble disappears, leaving an inclusion containing liquid and halite. With continued heating the inclusion will follow an isochoric path through the two-phase (L+H) field to “C3”, where the halite crystal disappears. If the inclusion is heated beyond the homogenization temperature, the P-T conditions within the inclusion will follow isochore “C” into the one-phase liquid field.

PVTX data are available for high salinity H_2O-NaCl fluids in the one-phase liquid field up to 70 wt.% NaCl, 900°C and 500 MPa (Bodnar, 1985). Thus, the P-T paths followed by inclusions that homogenize by modes “A” and “B” may be determined, and the trapping conditions can be estimated from microthermometric data. However, PVTX data for the two phase liquid + halite field are not available, except for a composition of 40 wt.% NaCl (Bodnar, 1994). Thus, the path followed by type “C” inclusions from the point at which the

vapor bubble disappears (C2; Fig. 2) to that at which the halite disappears (C3; Fig. 2), cannot be estimated from microthermometric data. The isochore through the two-phase field is shown as a dashed straight line on Fig. 2, because the exact P-T path through this field is not known (only the two end points, on the three-phase L+V+H curve and on the liquidus L+H, are known).

Methods

Synthetic fluid inclusions

Synthetic fluid inclusions were prepared as described by Sterner and Bodnar (1984). Clean, inclusion free, fractured quartz prisms 1.25 to 2.0 cm long were sealed in 2.5 cm platinum capsules with 100μL of saturated H_2O-NaCl solution (~26 wt. %) and excess halite. Adding saturated solution and halite to the capsule ensured that the solution was halite-saturated at room temperature and decreased the amount of time required for the aqueous solution to equilibrate with halite at experimental conditions. This ensured that the inclusions were trapped along a halite liquidus and would thus homogenize along the liquidus. A consequence of this approach is that the composition of the solution trapped is not known. Fortunately, the salinity of the inclusions can be calculated, as discussed below.

Each capsule was placed into a cold-seal hydrothermal autoclave and run at pre-selected P-T conditions of 50, 100, 200, and 300 MPa, and temperatures ranging from 300° to 550°C. Experiments conducted at ≤ 400°C were run for 18-21 days, whereas those > 400°C were run for 10-14 days. One additional experiment was performed at 300°C and 50 MPa for 47 days. Longer runs were necessary at lower temperatures to allow the fractured quartz to heal and trap inclusions suitable for study. The accuracy of both pressure and temperature in the autoclaves is estimated to be ±1% relative (Sterner and Bodnar, 1991). At the completion of the experiment, quartz prisms were removed from the capsules, placed into glass tubes containing Crystalbond™, sliced into disks, and polished. Depending on abundance and quality, up to 10 inclusions from each sample were selected for microthermometry and heated in a USGS gas-flow stage mounted on a Leitz microscope equipped with a 40x objective (N.A. = 0.55) with 15x oculars. The heating stage was calibrated at 374.1°C using pure H_2O synthetic fluid inclusions that homogenize by critical

behavior (Sterner and Bodnar, 1984). Liquid-vapor homogenization (Th_{L-V}) and halite dissolution temperatures (Tm_{halite}) were determined to ±0.05°C by thermal cycling using temperature steps of 0.1°C, followed by cooling a few degrees to determine if halite had disappeared. The thermal cycling technique was necessary to accurately determine Tm_{halite} because, as the halite became smaller and smaller during heating, it was often not possible to recognize the final disappearance if the inclusion was heated continuously. With the thermal cycling technique, the inclusion is heated until the halite is no longer recognizable. Then, the inclusion is cooled a few degrees. If the halite crystal had not completely dissolved, the halite will become visible at the same location where it was last observed in the inclusion, and will grow in size as the inclusion cools. If the halite had completely dissolved, the inclusion will appear unchanged during cooling of several tens of degrees until eventually the halite will "pop" back, usually at a different position in the inclusion than that at which it was last observed during heating.

Natural inclusions

After the synthetic fluid inclusion study was completed and the relationship between Th_{L-V}, Tm_{halite}, and pressure was established, two natural samples containing inclusions that homogenize by halite disappearance were studied for comparison with the experimental results. Samples studied include breccia-matrix quartz from the Questa porphyry-Mo deposit in New Mexico (Cline and Bodnar, 1994), and fluorite from the Naica, Mexico, chimney-manto limestone replacement base-metal deposit (Erwood et al., 1979). Doubly-polished fragments of quartz (Questa) and fluorite (Naica) were prepared by mounting samples on 1" round glass disks and grinding the samples by hand until they were sufficiently thin that distinct fluid inclusion assemblages (FIAs) could be unambiguously identified. An FIA represents a group of petrographically-associated inclusions that were all trapped at the same time and, presumably, at the same temperature and pressure and from a fluid of the same composition (Goldstein and Reynolds, 1994). It is only possible to assess the validity of microthermometric data and to evaluate "Roedder's Rules" (Bodnar, 2003a, b) if the data are collected following the FIA methodology. Most natural samples contain many generations of FIAs that crosscut the crystals. Thus, when observing the sample under the microscope, any field of view may contain fluid inclusions from several different FIAs that were trapped

at different times, and at different temperatures and pressures and from different fluids in an evolving hydrothermal system. However if the sample is thinned sufficiently such that the number of fluid inclusions in the field of view is reduced, it often becomes easier to identify individual FIAs (fractures or growth zones) and to confidently assign each inclusion to an FIA. FIAs in samples from Questa and Naica identified in this manner were analyzed in the heating/cooling stage as previously described. $Th_{L\text{-}V}$ and Tm_{halite} were determined using the same thermal cycling technique described previously for the synthetic fluid inclusions, except that a 1°C step was used, rather than 0.1°C, resulting in a precision of ±0.5°C. A larger temperature step was used because variations in Tm_{halite} for FIAs in natural samples are typically on the order of several degrees or more. Thus, heating steps of 0.1 degree Celsius were unwarranted and a precision of ±0.5°C was sufficient.

Results

Relationship between pressure, Tm_{halite} and $Th_{L\text{-}V}$

Microthermometric data obtained from synthetic fluid inclusions are summarized in Table 1 and Figure 3. Vapor bubble disappearance temperatures ($Th_{L\text{-}V}$) and halite dissolution temperatures (Tm_{halite}) vary smoothly and systematically along the 50, 100, 200, and 300 MPa isobars (Fig. 3). An empirical least-squares regression model relating pressure P to $Th_{L\text{-}V}$ and Tm_{halite} has been developed to estimate pressure in the inclusion at homogenization, which also represents a minimum pressure of formation.

$$P = \sum_{i=0}^{2}\sum_{j=0}^{2} a_{i,j} Th^{i} Tm^{j} + b\ln(Tm) + c\ln(Th + Tm) \qquad (1)$$

where P is the pressure in MPa, Th is the liquid-vapor homogenization temperature in degrees Celsius, Tm is the halite dissolution temperature in degrees Celsius, and $a_{i,j}$, b and c are the regression coefficients. Regression coefficients for this equation are listed in Table 2. The residual standard error for equation (1) = 5.519 with an $R^2 = 0.998$. Equation (1) is valid from $Th_{L\text{-}V}$ ≈200 to 500°C, and Tm_{halite} ≈300 to 550°C. Isobars in $Th_{L\text{-}V}$ versus Tm_{halite} and (Tm_{halite} - $Th_{L\text{-}V}$) versus $Th_{L\text{-}V}$ space have been estimated over the range of experimental data using Equation (1) and are plotted in Figures 4 and 5. These plots are intended as a tool to

help inclusionists evaluate data from type "C" inclusions graphically if they choose to not use the empirical equation presented above.

Equation (1) was applied to the example fluid inclusion described above and shown graphically in Figure 2. The equation predicts a minimum trapping pressure of 151 MPa for an inclusion with $Th_{L\text{-}V}$ = 310°C and Tm_{halite} = 400°C. This pressure is similar to the 110 MPa estimated by the Lemmlein and Klevtsov method (Klevtsov and Lemmlein, 1959; Lemmlein and Klevtsov, 1961), somewhat higher then the 65 MPa estimated by Roedder and Bodnar (1980), and significantly lower than the 500 MPa predicted by Lyakhov (1973) (Fig. 2).

Synthetic inclusions in this study were trapped on a halite liquidus. This means that Tm_{halite} equals the trapping temperature, and consequently the pressure inside the inclusion at Tm_{halite} equals the trapping pressure. Thus, as the inclusions were heated from room temperature to Tm_{halite}, pressures in the inclusions increased to 50 – 300 MPa, depending upon the trapping pressure. The elevated pressures developed in the inclusions during heating to measure $Th_{L\text{-}V}$ and Tm_{halite} did not significantly affect inclusions trapped at pressures of 50 to 200 MPa. However, most inclusions trapped at 300 MPa decrepitated before Tm_{halite} was reached, owing to the high internal pressures (Bodnar, 2003b). Consequently, the experimental temperature was substituted for Tm_{halite} for inclusions trapped at 300 MPa. As a result the error in temperature along the 300 MPa isobar is greater than the error for the other isobars because the experimental temperature is considered to be accurate to about ±1 percent (Sterner and Bodnar, 1991), corresponding to an uncertainty of ±5.5°C at 550°C. However, this error is not likely to exceed more than a few tens of MPa because the maximum error in temperature should be no more than ±1% error in the temperature increase between the 200 and 300 MPa isobars, which is small compared to the total range of temperature between the 100 and 200 MPa isobars.

Fluid inclusion compositions

All of the synthetic inclusions in this study trapped a liquid that was saturated in halite, i.e., the inclusions were trapped on the halite liquidus. Thus, the relationship between trapping pressure, $Th_{L\text{-}V}$, and Tm_{halite} could be determined directly from experimental and

microthermometric data, but the composition of the liquid that was trapped in the inclusions was not known.

Historically, fluid inclusionists have used NaCl solubility along the L+V+H curve (Fig. 2) to estimate salinities of halite-bearing inclusions that homogenize by any of the three modes "A", "B" and "C". This method provides correct salinities for inclusions that homogenize by modes "A" and "B". However, type "C" inclusions homogenize along a liquidus, and data for NaCl solubility on the vapor-saturated solubility curve may not be valid for type "C" inclusions. If the solubility of NaCl were pressure independent, then the halite liquidi would be represented by vertical lines ($dT/dP = 0$) on a P-T diagram, and solubilities along the vapor-saturated solubility curve would be valid along the liquidi. The ice (I) liquidus in the pure H_2O system has a slope of approximately -10.5°C/100 MPa, whereas the slope of the liquidus for pure NaCl has a slope of ≈22.6°C/100 MPa (Bodnar, 1994). As NaCl is added to the system H_2O, the slopes of the liquidi become increasingly less negative up to about 50 wt.% NaCl where the slope is 0°C/100 MPa. The slopes of the liquidi continue to become more positive with increasing salinity above 50 wt. % and finally achieve a slope of 22.6°C/100 MPa for pure NaCl. Thus, the halite liquidi are not vertical lines, but rather have slopes that change from negative to positive as the salinity increases (Fig. 6). Unless Tm_{halite} and the pressure along the liquidus are known, the salinity cannot be determined. The results of this study may be used to determine this pressure, and the composition of inclusions that homogenize by halite disappearance may be estimated as described below.

The minimum trapping pressure of type "C" inclusions may be estimated from measured $Th_{L\text{-}V}$ and Tm_{halite} using Equation (1). This calculated pressure and measured Tm_{halite} define a point in P-T space on a halite liquidus (e.g. point "C3", Fig. 2). The slopes of the halite liquidi as a function of salinity have previously been estimated over the range 26-100 wt.% NaCl (Bodnar, 1994). Additionally, NaCl solubility is known as a function of temperature and pressure along the three-phase curve (Sterner et al., 1988). Only one liquidus may pass through any P-Tm_{halite} point. Thus, by incrementally varying salinity along the three phase curve, calculating the slope of the liquidus for that salinity, and extrapolating that liquidus to the measured Tm_{halite}, the pressure at Tm_{halite} for that salinity may be estimated using the point-slope form of a linear equation. This pressure is compared

with the pressure at Tm_{halite} predicted by Equation (1). If they differ, then the salinity chosen is not the salinity of the inclusion, and the salinity is then decreased (or increased) incrementally until the pressures at Tm_{halite} estimated by these two independent methods agree. The input salinity (along the three phase curve) then represents the salinity of the inclusion. Using this method, the compositions of the synthetic fluid inclusions trapped along the liquidus in this study have been determined. A set of R and FORTRAN functions that perform this iterative calculation is available in Appendices B and C.

Discussion

In porphyry copper deposits, halite-bearing fluid inclusions displaying types "A", "B," and "C" homogenization behavior are common. All three inclusion types often occur in a single deposit, reflecting evolving P-T conditions during crystallization and cooling of the magmatic-hydrothermal system. For example, a high salinity fluid might follow an essentially isobaric path that starts in field "A" and crosses isochore "B" into field "C" during cooling (path 1→2→3, Fig. 2). Inclusions trapped at points "1", "2" and "3" would homogenize via modes "A", "B" and "C", respectively. Similarly, a decreasing pressure path at relatively constant temperature could also produce all three types of inclusions (path 4→2→5, Fig. 2). An important difference in the two processes that generate these three different types of inclusions is that along the isobaric path the earliest inclusions would be type "A", followed by types "B" and "C", whereas along the isothermal path the earliest inclusions would be type "C", followed by types "B" and "A". Thus, careful petrographic examination of samples to determine the relative ages of the different modes of homogenization of halite-bearing fluid inclusions might provide valuable information concerning the P-T history of the deposit.

Expected trends in $Th_{L\text{-}V}$ versus Tm_{halite} for natural inclusions

Most studies report the occurrence of types "A", "B", and "C" inclusions in the same deposit or in the same sample. As noted above, this is to be expected as the P-T path followed during cooling and uplift in a plutonic environment is likely to traverse all three fields shown on Figure 2. Most workers present microthermometric data from halite-bearing

inclusions as plots of Th_{L-V} versus Tm_{halite}, or Th_{L-V} versus salinity. A simple inspection of these data does not permit one to apply "Roedder's Rules" (Bodnar, 2003a) to validate the data because results for individual FIAs are usually not presented. As such, it is not possible to determine from visual inspection of the plots if individual FIAs exhibit consistent Tm_{halite}, and Th_{L-V}. However, it is possible to predict Th_{L-V} - Tm_{halite} trends that should be expected for different inclusion trapping scenarios.

In many hydrothermal systems, the fluid may become saturated in halite during its evolution and precipitate halite crystals on a growing crystal surface (Fig. 7a). The halite crystals thus "poison" the growing surface, causing the crystal to grow around the foreign halite crystal and in the process some of the NaCl-saturated fluid may be trapped along with the halite to produce type "C" fluid inclusions. Some inclusions will trap only the liquid phase (inclusions 2, 4, 5, 7 and 9; Fig. 7a), while others will trap various proportions of liquid and halite (Fig. 7a). As a result, there will be a wide range in Tm_{halite} for these inclusions, ranging from the lowest values corresponding to inclusions that trapped only liquid and extending to higher values for those inclusions that trapped a halite crystal along with the liquid (inclusions 1, 3 6 and 8; Fig. 7a). However, the P-T paths followed by these inclusions through the halite + liquid field will all be essentially the same because the salinity (and density) of the *liquid phase* will be the same in all inclusions and the halite crystal can be considered to be incompressible (constant density) over temperature and pressure ranges of a few hundred degrees Celsius or a few hundred megapascals (Bodnar, 1994). The net result is that Th_{L-V} will be identical (or nearly so) for all of these inclusions, even though they have very different salinities and halite to liquid ratios at room temperature. Plots of Th_{L-V} versus Tm_{halite} for these inclusions will show a range in Tm_{halite} at constant Th_{L-V} (Fig. 7b). The inclusion with the largest halite/liquid ratio at trapping (inclusion 8; Fig. 7a) will have the highest Tm_{halite} and those inclusions that trapped only the halite-saturated liquid along the liquidus will have the lowest Tm_{halite} (inclusions 2, 4, 5, 7 and 9 represented by filled circle; Fig. 7b). Pressures estimated from inclusions that trapped only the liquid phase represent the correct trapping pressure, whereas pressures estimated from Th_{L-V} and Tm_{halite} for inclusions that trapped halite along with the liquid will be higher than the actual trapping pressure.

Inclusions that homogenize by halite dissolution may also be produced by necking. If necking occurs at a constant temperature and pressure and the original inclusion contains

only a single fluid phase (inclusion 1; Fig. 8a), the densities of the resulting inclusions (inclusions 2 and 3; Fig. 8a) will be the same as the original inclusion. The inclusions produced by necking (inclusions 2 and 3; Fig. 8a) will have the same homogenization temperature and composition as the original inclusion and follow the same isochore that the original inclusion would have followed had necking not occurred (Fig. 8a). However, necking may also occur after a halite crystal has nucleated in the inclusion. In this case, one of the pair of necked inclusions might contain only liquid (inclusion 5; Fig. 8a) while the other inclusion might contain liquid plus a halite crystal (inclusion 4; Fig. 8a). Because the density and composition of the liquid in each of the two inclusions would be the same, these inclusions would follow the same P-T path during cooling to room temperature and would have the same $Th_{L\text{-}V}$. The necked inclusion that contained only liquid after necking (inclusion 5; Fig. 8a) would have Tm_{halite} equivalent to the temperature at which necking occurred (Fig. 8b), while the inclusion that included the halite crystal (inclusion 4; Fig. 8a) would have a higher salinity and Tm_{halite} (Fig. 8b).

The necking process could occur continuously during cooling, even after the P-T path has passed into the halite + liquid field (i.e., at a temperature lower than that on the liquidus corresponding to the original salinity). Thus, both of the necked inclusions formed on liquidus A (inclusions 4 and 5; Fig. 8a) will contain halite and liquid at temperatures below the liquidus temperature. If one of these inclusions necks at some temperature significantly below the original liquidus temperature (bold liquidus; Fig. 8a), one inclusion will contain liquid plus a relatively large halite crystal (inclusion 6; Fig. 8a) and one will contain only liquid (inclusion 7; Fig. 8a). Both of these inclusions will have same (correct) $Th_{L\text{-}V}$, but different Tm_{halite}. Note that the inclusion that includes only the liquid phase (inclusion 7; Fig. 8a) will have Tm_{halite} that is *lower* than that for the original inclusion (inclusion 1; Fig. 8a), and those that necked in the one-phase field at temperatures greater than that of the original liquidus (inclusions 2 and 3; Fig. 8a), and those that necked close to the original liquidus and included only the liquid phase (inclusion 5; Fig. 8a).

The trend in Tm_{halite} and $Th_{L\text{-}V}$ for the inclusions that necked (Fig. 8b) is identical to that produced by trapping of halite crystals along with the liquid (Fig. 7b). For those inclusions that trapped halite, the Tm_{halite} and $Th_{L\text{-}V}$ that represents the trapping of only the liquid phase on the halite liquidus, and thus represents the real trapping conditions, is that

with the lowest Tm_{halite}. Conversely, the Tm_{halite} and $Th_{L\text{-}V}$ that represents the actual trapping conditions in the case of necking depends on whether or not necking continued at temperatures less than that along the liquidus corresponding to the original salinity. If necking did not continue below the original liquidus, then the data that correspond to the original trapping conditions is that with the lowest Tm_{halite}, similar to the case in which some inclusions trap halite. However, if necking continues below the original liquidus, then the lowest Tm_{halite} (i.e., inclusions 5 and 7; Fig. 8b) does not correspond to the original trapping conditions. There is no mechanism that we are aware of that would allow us to know which of the many inclusions along this trend is the one that trapped only liquid at the original formation conditions. If halite solid inclusions are observed in the host mineral, one might conclude that the fluid was saturated in halite and that trapping of halite along with the liquid is responsible for the observed Tm_{halite} and $Th_{L\text{-}V}$ trend. In the absence of such petrographic information, it is not possible to arrive at any meaningful interpretation of the microthermometric data.

Another type of reequilibration that commonly occurs is stretching, whereby the volume of an inclusion increases (decreasing density) without changing the bulk composition (Bodnar, 2003b). Stretching of inclusions can occur in any mineral, but is particularly common in soft (low Mohs hardness, high ductility) minerals (Bodnar, 2003b; Bodnar and Bethke, 1984; Ulrich and Bodnar, 1988). The decrease in density associated with stretching results in the inclusions following a different isochore than that of the original unstretched inclusion, resulting in a higher liquid-vapor homogenization temperature. Thus, a fluid inclusion trapped in the one-phase field (inclusion 1; Fig. 9a) that remains unstretched (isochoric) will follow the original isochore (Fig. 9a) to the liquid+vapor+halite (L+V+H) curve. During heating from room temperature the inclusion will homogenize at this same point of intersection. As a result of stretching, the inclusions move to progressively lower density isochores and these isochores intersect the L+V+H curve at increasingly higher temperatures with greater amounts of stretching (inclusions 2-5; Fig. 9a). Thus, stretching results in a range of $Th_{L\text{-}V}$. The effect of stretching on Tm_{halite} depends on the slope of the halite liquidus for the inclusion salinity. Because halite liquidi slopes are generally very steep (Fig. 6), Tm_{halite} will not change significantly except as a result of unrealistically large increases in inclusion volume. Stretching thus produces a $Th_{L\text{-}V}$ - Tm_{halite} trend with

relatively uniform Tm_{halite} but a range in $Th_{L\text{-}V}$ (Fig. 9b). If inclusions in an FIA show a trend similar to that illustrated in Figure 9b (or any trend of varying liquid-vapor homogenization temperature but constant composition), one can reasonably assume that stretching has occurred. Stretched inclusions have higher $Th_{L\text{-}V}$ compared to unstretched inclusions. Thus, the inclusion with the lowest $Th_{L\text{-}V}$ (inclusion 1; Fig. 9b) most closely represents the original trapping conditions and provides the closest approximation of minimum trapping pressure.

Under unusual circumstances, inclusions that homogenize by halite disappearance may be generated by reequilibration associated with mobilization and loss of H_2O (Audétat and Günther, 1999). In some boiling assemblages, there is unambiguous petrographic evidence for vapor-rich inclusions coexisting with inclusions that homogenize by halite disappearance. Phase equilibria do not permit these two types of inclusions to be in equilibrium, as vapor-rich inclusions must be trapped on a vapor-saturation boundary and inclusions that homogenize by halite disappearance cannot be in equilibrium with a vapor phase (Bodnar and Sterner, 1985; Roedder and Bodnar, 1980) (Fig. 2). An inclusion assemblage consisting of halite-bearing inclusions that homogenize by halite disappearance and vapor-rich inclusions could be produced by 1) post entrapment volume reduction (density increase), 2) selective H_2O loss (salinity increase), or 3) accidental trapping of halite crystals (Audétat and Günther, 1999). Scenarios "1" and "2" are possible during migration of inclusions within the quartz host after initial entrapment. Scenario "3" has already been discussed, however it should be noted that trapping halite in a boiling system is only possible on the three-phase (L+V+H) curve, and inclusions that homogenize via mode "B" ($Th_{L\text{-}V} = Tm_{halite}$; Fig. 2) should be present in such an assemblage.

Application of Results to Synthetic and Natural Fluid Inclusions

Reequilibration processes described above likely explain much of the scatter observed in published $Th_{L\text{-}V}$ - Tm_{halite} data. However, it appears that in many cases the scatter in published $Th_{L\text{-}V}$ - Tm_{halite} data results because workers have not collected or reported their results within the context of FIAs. This consequences in mixing data from fluid inclusions trapped at different times and, presumably, at different P-T conditions and from fluids of different salinities. Below we present several examples from synthetic and natural fluid

inclusions that document that it is possible to obtain consistent $Th_{L\text{-}V}$ - Tm_{halite} data that show relatively little scatter if one collects and compares only data from well-defined FIAs.

Synthetic fluid inclusions containing 40 wt. % NaCl

Bodnar (1994) determined the location of the 40 wt. % halite liquidus experimentally using synthetic fluid inclusions, and reported $Th_{L\text{-}V}$, Tm_{halite} and pressure along the liquidus. These data provide a basis for comparison with results of this study. $Th_{L\text{-}V}$ versus Tm_{halite} for a range of densities along the 40 wt. % liquidus show good agreement with results of this study over most of the pressure range (Figs. 10a, 11). However, at the highest pressures the difference between the experimental data of Bodnar (1994) and pressures calculated from Equation (1) in this study increases (Fig. 11). This increasing difference with increasing pressure above about 250 MPa has two possible explanations. Firstly, Equation (1) is only valid to 300 MPa and the high-pressure data for the 40 wt% liquidus are outside of this range. This explanation is considered to be less likely because $Th_{L\text{-}V}$ versus Tm_{halite} for 40 wt. % inclusions from the study of Bodnar (1994) that have a liquidus pressure near 300 MPa appear to be consistent with extrapolation of the 300 MPa isobar from this study to lower values of Tm_{halite}.

A second possibility is that during laboratory heating stretching becomes significant above 250 MPa. Bodnar and coworkers (Bodnar et al., 1989) have shown that all inclusions larger than about 5 μm in quartz will stretch or decrepitate at pressures ≥250 MPa. In this case the density in the inclusions continuously decreases as the inclusion stretches during heating, placing the heating path on progressively lower density isochores. As a result the inclusion P-T path intersects the liquidus at a lower pressure than it would have if the inclusion followed an isochoric path (i.e., did not stretch during heating). Bodnar (1994) assumed an isochoric path during heating to homogenization. Because the slope of the 40 wt. % liquidus is very steep (-5.5°C/100 MPa; Bodnar, 1994), stretching will not significantly affect Tm_{halite} – that is the temperature of intersection of the heating path with the liquidus does not change much as pressure changes. Assuming that stretching did occur, pressures reported by Bodnar (1994) represent a maximum pressure at halite dissolution because he assumed an isochoric path. We believe that this second explanation for the

increasing difference between the highest-pressure results of Bodnar (1994) and those from this study is the most likely.

Ditrau Alkaline Massif, Transylvania, Romania

The Ditrau Alkaline Massif, Transylvania, Romania contains several different types of fluid inclusions, including three-phase (liquid + vapor + halite) inclusions that homogenize by halite disappearance (Fall et al., 2007). The halite-bearing inclusions are oriented parallel to the cleavage direction of nepheline and define FIAs that are interpreted to have been trapped after formation of the host nepheline. The observed decreasing salinity trend with time in the Ditrau Alkaline Massif indicates crystallization pressures ≥ 200MPa (Cline and Bodnar, 1991). This is consistent with extrapolation of isochores for moderate salinity inclusions in the Ditrau Alkaline Massif to the H_2O-saturated solvus in the nepheline-H_2O system, which indicates pressures in excess of 250 MPa, with a maximum pressure of about 500 MPa (Fall et al., 2007).

The homogenization behavior of halite-bearing inclusions in the Ditrau Alkaline Massif is consistent within an individual FIA and vapor-rich inclusions are absent, suggesting entrapment in field "C" (Fig. 2). Microthermometric data ($Th_{L\text{-}V}$ versus Tm_{halite}) for the FIAs cluster tightly near the low-temperature end of the 50MPa isobar (Fig. 10b). Combining these microthermometric data with pressures reported above based on the nepheline-H_2O system suggests that the inclusions were trapped in the one-phase field (e.g. along isochore "C" in field "C", Fig. 2) at about 400-600°C. This temperature range is consistent with temperature estimates based on the position of the H_2O-saturated solvus, and with extrapolation of isochores for later, lower salinity inclusions in nepheline and cancrinite that were interpreted to have been formed at the same pressure as the halite-bearing inclusions, but at slightly lower temperature.

Musoshi stratiform copper deposit, Zaire

Fluid inclusions in footwall quartz-hematite veins at the Musoshi stratiform copper deposit in Zaire (now DRC) contain halite daughter minerals and most homogenize by halite disappearance (Richards et al., 1988). Richards and coworkers also reported the occurrence

of isolated halite cubes in the quartz and interpreted this to indicate that the halite-bearing inclusions were trapped on the halite liquidus – thus Tm_{halite} equals the trapping temperature. Interpretation of microthermometric data for these inclusions using the H_2O-NaCl system must be viewed with caution because sylvite daughter minerals occur in about 5% of the inclusions, and energy dispersive microprobe analysis of inclusion decrepitate residues showed the presence of Fe, K, Ca, and Mn chlorides. Moreover, some inclusions contain small amounts of CO_2, as evidenced by melting at -56.6°C and the rare occurrence of a separate CO_2 phase at room temperature.

Within individual samples, homogenization temperatures are very consistent, varying by no more than about ±1° to ±13°C, and define three distinct regions in $Th_{L\text{-}V}$ versus Tm_{halite} space (Fig. 10c). Five samples (which Richards and coworkers classified as "high temperature" samples) form a tight cluster between 50 and 100 MPa, and were collected from 7 to 30m below the ore shale. Two samples (which Richard and coworkers classified as "low temperature" samples) plot outside of the $Th_{L\text{-}V}$ - Tm_{halite} range of our experimental data. However, extrapolation of the 100 and 200 MPa isobars to lower $Th_{L\text{-}V}$ and Tm_{halite} indicates minimum trapping pressures of approximately 150 MPa. As noted above, halite crystals in quartz are associated with both the low and high temperature groups, suggesting that the fluid was halite saturated when the halite-bearing inclusions were trapped. In this case Tm_{halite} represents the trapping temperature (assuming the fluid inclusions did *not* trap a halite crystal along with the liquid), and pressures shown on Figure 10c represent the trapping pressures (i.e., no pressure corrections are needed). This interpretation is consistent with maximum pressures of 120 MPa estimated by Richards and coworkers based on the observation that fluid inclusions did not decrepitate during heating to Tm_{halite}. Richards and coworkers based this pressure on decrepitation data for fluid inclusions in quartz that were available at the time (Leroy, 1979). More recent data indicate that the decrepitation pressure depends on the inclusion size, and ranges from about 50 MPa for a 100 μm inclusion, to about 350 MPa for a 1 μm inclusion (Bodnar, 2003b; Bodnar et al., 1989).

Inclusions in sample [13]-300W-0, that comes from the "deep footwall vein" 300 m below the ore shale, plot considerably outside the range of our experimental data. Extrapolation of the 300 MPa isobar to lower temperatures suggests a minimum trapping pressure in excess of 300 MPa for these inclusions. This pressure appears to be unreasonably

high for sediment-hosted ore deposits. However, Richards and coworkers suggest that fluids associated with the deep footwall vein may have been sourced from deeply buried sediments during compressional deformation and metamorphism. Microthermometric data for this sample are remarkably consistent with 40 inclusions having $Th_{L\text{-}V}$ between 110 and 125°C, and Tm_{halite} between 285 and 300°C. While the inferred pressures appear to be too high for the geologic environment, the consistency of microthermometric data rules out reequilibration or mixed trapping, as both of these processes tend to smear out the data (Bodnar, 2003b; Vityk and Bodnar, 1995, 1998).

Bismark skarn deposit, Mexico

The Bismark skarn deposit in northern Mexico hosts massive sulfide ore in direct contact with a quartz monzonite stock (Baker and Lang, 2003). Quartz, calcite and fluorite contain halite-bearing inclusions, and Baker and Lang distinguished between type 3A inclusions containing liquid, vapor and halite, and Type 3B inclusions containing liquid, vapor, halite and sylvite. Both inclusion types often also contain various opaque and other unidentified phases, and both types show all three modes of homogenization ($Th_{L\text{-}V} > Tm_{halite}$, $Th_{L\text{-}V} = Tm_{halite}$, and $Th_{L\text{-}V} < Tm_{halite}$). Microthermometric data ($Th_{L\text{-}V}$ versus Tm_{halite}) for individual inclusions define three distinct groups, and show the best consistency when sorted according to host mineral (Fig. 10d). Baker and Lang (2003) estimated minimum trapping pressures of ≈60 MPa for type 3A inclusions in early fluorite that homogenize by halite disappearance, and pressures of 80 and 95 MPa for secondary inclusions. We note that Baker and Lang estimated the minimum trapping pressure for inclusions that homogenize by halite disappearance using isochores for the one-phase field and assuming that the slope of the isochore in the halite + liquid field is the same. The average slopes of isochores in the halite + liquid field is actually steeper than in the one-phase liquid field (Bodnar, 1994), thus pressures estimated by Baker and Lang are less than the actual pressures.

Minimum trapping pressures estimated from our experimental data generally do not exceed 100 MPa, which agrees with Baker and Lang's interpretation using isochores for Type 3a inclusions to constrain pressures. Fluid inclusions hosted in calcite plot outside of the range of our experimental data, but extrapolation of our isobars to lower temperatures

indicates entrapment pressures of ~100 MPa for a cluster of points including calcite type 3b immediately to the lower left of the 100 MPa isobar (Fig. 10d). Other calcites are consistent with trapping between 100 and 200 MPa.

Naica chimney-manto deposit, Mexico

The Naica deposit near Chihuahua, Mexico is a chimney-manto, limestone replacement base metal deposit. Polyphase fluid inclusions ≤100μm in fluorite contain liquid, vapor and halite (Type B), or liquid, vapor, halite and sylvite (Type C), and homogenize by halite disappearance (Erwood et al., 1979). Both types may also contain a small, unidentified non-opaque phase (possibly a carbonate). Microthermometric analysis is facilitated by the large size of the inclusions (up to 100 μm) and excellent optical qualities of the fluorite. All observed inclusions were secondary, occurring as well defined trails along healed fractures.

Microthermometric data were obtained from three FIAs represented by trails of secondary inclusions and are reported in Table 3. Microthermometric data (Th_{L-V} versus Tm_{halite}) for individual FIAs define a trend of constant Tm_{halite} but variable Th_{L-V} (Fig. 10e). This trend suggests that the inclusions have reequilibrated by post-entrapment stretching (compare to Fig. 9b). Stretching is the likely cause of the variable Th_{L-V} because it is well known that inclusions in relatively soft minerals such as fluorite stretch at relatively low internal pressures (Bodnar, 2003b; Bodnar and Bethke, 1984). This may be attributed to the high ductility of such minerals. Based on measured Tm_{halite} and Th_{L-V} we estimate that the internal pressure in the inclusions could have been as high as 200 MPa. Thus, it is not surprising that significant stretching of the host fluorite occurred. It is not possible to determine if the stretching occurred in nature or during heating in the lab.

As noted previously, stretching decreases the density of the fluid inclusions and results in the P-T path followed during heating to intersect the halite liquidus at a lower pressure than it would had stretching not occurred (Fig. 9b). However, the estimated minimum trapping pressures of reequilibrated inclusions are difficult to reconcile based on the geology of the Naica deposits. Stretching of inclusions increases Th_{L-V} without significantly affecting Tm_{halite}; thus, the lowest Th_{L-V} measured should most closely approximate Th_{L-V} that would have been observed had stretching not occurred (e.g., inclusion

1; Fig. 9b). Erwood and coworkers approximated isochores in the liquid + halite field to determine pressures of inclusions that homogenize by halite disappearance, and obtained pressures ranging from 30-160 MPa (Type B inclusions) to 50-270 MPa (Type C inclusions). In addition to inclusions that homogenize by halite disappearance, coexisting liquid-rich and vapor-rich inclusions that are indicative of boiling in the Naica deposit suggest trapping pressures of 4 to 14 MPa. Depths of formation estimated from the boiling assemblages range from 400 to 1700 m, and these depths are consistent with depths based on the local geology. But, one should not expect pressures up to 270 MPa at such shallow depths. To explain these high pressures, Erwood and coworkers suggested that the system could have periodically become overpressured. While overpressured hydrothermal systems do occur, they usually form at greater depth and overpressures of more than a few 10 MPa are unlikely (Burnham, 1997).

Populations of inclusions with consistent homogenization behavior that predict geologically unreasonable high pressures are a conundrum, yet they are relatively common (e.g., the "deep footwall vein" samples from the Musoshi stratiform copper deposit described above). Erwood and coworkers attributed inclusions that homogenize by halite disappearance to phase separation involving liquid and halite along the liquidus prior to entrapment, resulting in the "halite trend" (Cloke and Kesler, 1979). This interpretation should result in accidental entrapment of halite crystals to produce a trend similar to that shown in Figure 7a. However, this condition might be expected to result in halite crystals being trapped in the host phase, as was observed at Musoshi (Richards et al., 1988). Erwood and coworkers report small halite xenocrysts in some fluorites. In the present study, we did not observe halite crystals in the fluorites, but only a single sample was examined.

Questa porphyry molybdenum deposit, New Mexico

Inclusions that homogenize by halite disappearance have been reported from the Questa, New Mexico, porphyry molybdenum deposit (Cline and Bodnar, 1994). These inclusions appear to have trapped a high salinity fluid that exsolved directly from the magma, unlike most high salinity fluids in porphyry type deposits that originate by fluid phase immiscibility (Bodnar, 1995; Bodnar et al., 1985). Although the data show some scatter, Cline and Bodnar reported a grouping of $Th_{L\text{-}V} \approx 320°C$ and $Tm_{halite} \approx 380°C$ that is

characteristic of a majority of the inclusions. The lack of coexisting vapor-rich inclusions indicates that the high salinities were not the result of immiscibility, but rather represent the direct exsolution of brine from a crystallizing magma. Isochores bounding the region near $Th_{L\text{-}V} \approx 320°C$ and $Tm_{halite} \approx 380°C$ define a range of possible trapping pressures from approximately 75 to 150 MPa. Equation (1) predicts a minimum trapping pressure of approximately 97 MPa for an inclusion with $Th_{L\text{-}V} \approx 320°C$ and $Tm_{halite} \approx 380°C$.

In this study we examined a single FIA (QFIA-1) hosted in a 2 cm euhedral quartz crystal growing into a vug. The fluid inclusions were primary, with equant shapes and oriented parallel to the c-axis. These polyphase inclusions were approximately 10 to 20 μm in maximum dimension, and contained liquid, vapor, halite, chalcopyrite, and a small non-opaque phase. All homogenized by halite disappearance. Microthermometric data reported in Table 4 show relatively consistent $Th_{L\text{-}V}$ of approximately 330°C, with the exception of one inclusion with $Th_{L\text{-}V} = 351°C$. It is possible that this one inclusion reequilibrated (by stretching) to some extent, although a 20°C variation is not unreasonable in an FIA from a natural sample and could reflect slight pressure and/or temperature fluctuations during growth of the quartz. Three inclusions had $Tm_{halite} = 390°C$ and two others had halite dissolution temperatures of 406° and 450°C, respectively. Because $Th_{L\text{-}V}$ for these two inclusions are consistent with others from this same FIA, the inclusions likely trapped small halite crystals that were precipitating on the surface of the quartz crystal as the inclusions were being trapped. The $Th_{L\text{-}V}$ versus Tm_{halite} trend (Fig. 10f) is consistent with accidental trapping (Fig. 7b). The trend could also be explained by necking (Fig. 8b). However, necking during cooling is likely to result in significantly different Tm_{halite} for every inclusion in the FIA—here, three of the inclusions have very similar Tm_{halite}, and so this explanation is less likely. If this interpretation is correct, the presence of halite crystals in equilibrium with fluid at the time of entrapment indicates that the FIA was trapped at halite saturation. The trapping temperature of this FIA is equivalent to Tm_{halite} for inclusions that trapped only liquid. These inclusions were trapped at ~390°C, and Equation (1) indicates a trapping pressure of approximately 96MPa. Pressures reported by Cline and Bodnar (1994) and those estimated from measurements in the present study are in good agreement and indicate that the pressure during Mo mineralization at Questa was approximately 100 MPa.

Summary

Halite-bearing fluid inclusions that homogenize by halite disappearance are common in many geological environments, and are especially common in porphyry copper deposits. Owing to a lack of PVTX data, previous workers have estimated trapping pressures for this type of inclusion using a variety of methods, often resulting in widely varying pressure estimates for inclusions showing similar microthermometric behavior (see Appendix A). In this experimental study, the synthetic fluid inclusion technique was used to obtain PVTX data that may be used to interpret microthermometric data from inclusions that homogenize by halite disappearance over the range $Th_{L\text{-}V} \approx 150°\text{-}500°C$ and $Tm_{halite} \approx 275°\text{-}550°C$. An empirical equation describing the relationship between pressure, $Th_{L\text{-}V}$, and Tm_{halite} has been developed to estimate formation pressures from microthermometric data.

Most published data for fluid inclusions that homogenize by halite disappearance cannot be evaluated and compared with results of the present study for various reasons. Only a very few studies have been performed following the protocol described by Goldstein and Reynolds (1994) that requires the study of fluid inclusion assemblages (FIAs) and tests the data for conformity with "Roedder's Rules" (Bodnar, 2003a). Thus, most studies group data from many different generations of inclusions, and sometimes from different samples, making it impossible to identify data from individual inclusions. Similarly, a common means of presenting the data is on plots of $Th_{L\text{-}V}$ versus Tm_{halite} (or salinity) rather than in tables, again making it difficult to associate a particular data point with a specific trapping event. Because both $Th_{L\text{-}V}$ and Tm_{halite} are easily modified by trapping of halite along with the liquid, and by stretching or necking, we propose that the experimental data reported in this study should not be used to interpret fluid inclusions that homogenize by halite disappearance unless inclusions can be unambiguously shown to belong to an FIA and produce consistent microthermometric data. The only exceptions to this would be if *all* inclusions within a sample have consistent microthermometric values (even though they cannot be proven to represent an FIA) or if halite crystals are observed in the host phase (indicating trapping of halite along with liquid) or if inclusions in an FIA show consistent Tm_{halite} but widely varying $Th_{L\text{-}V}$ (suggesting that stretching has occurred).

Some workers have studied fluid inclusions that homogenize by halite disappearance following the methodology of Goldstein and Reynolds (1994) and have presented results for

individual FIAs in tables, making it possible to evaluate the results using data obtained in this study. Formation pressures have been estimated for several occurrences using these published microthermometric data and there is general agreement between our results and pressures estimated previously based on some assumptions concerning P-T paths of isochores in the liquid + halite field, as well as on geological information. In some cases, the estimated pressures appear to be unreasonably high based on the inferred geology and depth of burial at the time the inclusions were trapped. These studies emphasize the fact that pressure, or depth of formation, remains one of the major unknowns in ore genesis research (Skinner, 1997).

Acknowledgments

The authors thank Jim Reynolds for suggesting Questa and Naica as examples of deposits in which fluid inclusions that homogenize by halite disappearance are common, and thank Jean Cline for providing a Questa sample for study. The authors also thank Eduardo Campos for providing samples for study. The authors thank Tim Baker, Jeremy Richards, Sarah Gleeson, John Mavrogenes, Jean Cline, Andrew Campbell, Bob Darling, Luiz Henrique Ronchi, and Steve Kissin for participating in a discussion on the fluid inclusion listserve and suggesting published studies reporting these inclusions. The authors also thank Brian Rusk for interesting discussions concerning inclusions that homogenize by halite dissolution in porphyry systems, and for providing microthermometric data to analyze. The authors also thank Mr. Charles Farley for assistance with hydrothermal experiments. This material is based upon work supported by the National Science Foundation under Grants No. EAR-0125918 and EAR-0337094.

References

Anderko, A., and Pitzer, K. S., 1993, Equation-of-state representation of phase equilibria and volumetric properties of the system NaCl-H_2O above 573 K: Geochimica et Cosmochimica Acta, v. 57, p. 1657-1680.

Audétat, A., and Günther, D., 1999, Mobility and H_2O loss from fluid inclusions in natural quartz crystals: Contributions to Mineralogy and Petrology, v. 137, p. 1-14.

Baker, T., and Lang, J. R., 2003, Reconciling fluid inclusion types, fluid processes, and fluid sources in skarns: an example from the Bismark Deposit, Mexico: Mineralium Deposita, v. 38, p. 474-495.

Bischoff, J. L., and Pitzer, K. S., 1989, Liquid-Vapor Relations for the System NaCl-H_2O: Summary of the P-T-x Surface from 300° to 500°C: American Journal of Science, v. 289, p. 217-248.

Bodnar, R. J., 1985, Pressure-Volume-Temperature-Composition (PVTX) properties of the system H_2O-NaCl at elevated temperatures and pressures: Unpub. PhD Dissertation thesis, The Pennsylvania State University, 183 p.

Bodnar, R. J., 1992, Can we recognize magmatic fluid inclusions in fossil hydrothermal systems based on room temperature phase relations and microthermometric behavior?: Geological Survey of Japan, v. 279, p. 26-30.

Bodnar, R. J., 1994, Synthetic fluid inclusions. XII. Experimental determination of the liquidus and isochores for a 40 wt.% H_2O-NaCl solution: Geochimica et Cosmochimica Acta, v. 58, p. 141-148.

Bodnar, R. J., 1995, Fluid inclusion evidence for a magmatic source for metals in porphyry copper deposits, *in* Thompson, J. F. H., ed., Mineralogical Association of Canada Short Course Volume 23, 23, p. 139-152.

Bodnar, R. J., 2003a, Introduction to fluid inclusions, *in* Samson, I., Anderson, A., and Marshall, D., eds., Fluid Inclusions: Analysis and Interpretation, Short Course 32, 32, Mineralogical Association of Canada, p. 1-8.

Bodnar, R. J., 2003b, Reequilibration of fluid inclusions, *in* Samson, I., Anderson, A., and Marshall, D., eds., Fluid Inclusions: Analysis and Interpretation, 32, Mineralogical Association of Canada, p. 213-230.

Bodnar, R. J., and Bethke, P. M., 1984, Systematics of stretching of fluid inclusions. I. Fluorite and sphalerite at 1 atmosphere confining pressure: Economic Geology, v. 79, p. 141-161.

Bodnar, R. J., Binns, P. R., and Hall, D. L., 1989, Synthetic fluid inclusions. VI. Quantitative evaluation of the decrepitation behavior of fluid inclusions in quartz at one atmosphere confining pressure.: Journal of Metamorphic Geology, v. 7, p. 229-242.

Bodnar, R. J., Burnham, C. W., and Sterner, S. M., 1985, Synthetic fluid inclusions in natural quartz. III. Determination of phase equilibrium properties in the system H_2O-NaCl to 1000°C and 1500 bars.: Geochimica et Cosmochimica Acta, v. 49, p. 1861-1873.

Bodnar, R. J., and Sterner, S. M., 1985, Synthetic fluid inclusions in natural quartz. II. Application to PVT studies: Geochimica et Cosmochimica Acta, v. 49, p. 1855-1859.

Burnham, C. W., 1997, Magmas and hydrothermal fluids, *in* Barnes, H. L., ed., Geochemistry of Hydrothermal Ore Deposits: New York, Wiley and Sons, p. 63-123.

Cline, J. S., and Bodnar, R. J., 1991, Can economic porphyry copper mineralization be generated by a typical calc-alkaline melt?: Journal of Geophysical Research, v. 96, p. 8113-8126.

Cline, J. S., and Bodnar, R. J., 1994, Direct evolution of a brine from crystallizing silicic melt at the Questa, New Mexico, molybdenum deposit: Economic Geology, v. 89, p. 1780-1802.

Cloke, P. L., and Kesler, S. E., 1979, The halite trend in hydrothermal solutions: Economic Geology, v. 74, p. 1823-1831.

Erwood, R. J., Kesler, S. E., and Cloke, P. L., 1979, Compositionally distinct, saline hydrothermal solutions, Naica Mine, Chihuahua, Mexico: Economic Geology, v. 74, p. 95-108.

Fall, A., Bodnar, R. J., Szabó, C., and Pál-Molnár, E., 2007, Fluid evolution in the nepheline syenites of the Ditrau Alkaline Massif, Transylvania, Romania: Lithos, v. 95, p. 331-345.

Goldstein, R. H., and Reynolds, T. J., 1994, Systematics of fluid inclusions in diagenetic minerals: Society for Sedimentary Geology Short Course 31, p. 199.

Haas, J. L. J., 1976, Physical Properties of the Coexisting Phases and Thermochemical Properties of the H_2O Component in Boiling NaCl Solutions: Geological Survey Bulletin, v. 1421-A, p. 73pp.

Klevtsov, P. V., and Lemmlein, G. G., 1959, Determination of the minimum pressure of quartz formation as exemplified by crystals from the Pamir: Zap. Vses. Mineral. Obshch., v. 85, p. 661-666.

Lemmlein, G. G., and Klevtsov, P. V., 1961, Relations among the principle thermodynamic parameters in a part of the system H_2O-NaCl: Geochemistry, v. 2, p. 148-158.

Leroy, J., 1979, Contribution a l'etalonnage de la pression interne des inclusions fluides lors de leur decrepitation: Bulletin de Société français de Minéralogie et de Cristallographie, v. 102, p. 584-593.

Lyakhov, Y. V., 1973, Errors in determining pressure of mineralization from gas-liquid inclusions with halite, their causes and ways of eliminating them: Zap. Vses. Mineral. Obshch., v. 102, p. 385-393.

Richards, J. P., Krogh, T. E., and Spooner, E. T. C., 1988, Fluid inclusion characteristics and U-Pb rutile age of late hydrothermal alteration and veining at the Musoshi stratiform copper deposit, Central Africa Copper Belt, Zaire: Economic Geology, v. 83, p. 118-139.

Roedder, E., 1984, Fluid Inclusions, *in* Ribbe, P. H., ed., Reviews in Mineralogy, 12: Washington, D.C., Mineralogical Society of America, p. 644.

Roedder, E., and Bodnar, R. J., 1980, Geologic pressure determinations from fluid inclusion studies: Annual Review of Earth and Planetary Sciences, v. 8, p. 263-301.

Skinner, B. J., 1997, Hydrothermal mineral deposits: What we do and don't know, *in* Barnes, H. L., ed., Geochemistry of Hydrothermal Ore Deposits: New York, Wiley & Sons, p. 1-29.

Sterner, S. M., and Bodnar, R. J., 1984, Synthetic fluid inclusions in natural quartz. I. Compositional types synthesized and applications to experimental geochemistry: Geochimica et Cosmochimica Acta, v. 48, p. 2659-2668.

Sterner, S. M., and Bodnar, R. J., 1991, Synthetic fluid inclusions. X. Experimental determination of P-V-T-X properties in the CO2-H2O system to 6 kb and 700 °C: American Journal of Science, v. 291, p. 1-54.

Sterner, S. M., Hall, D. L., and Bodnar, R. J., 1988, Synthetic fluid inclusions. V. Solubility relations in the system NaCl-KCl-H_2O under vapor-saturated conditions: Geochimica et Cosmochimica Acta, v. 52, p. 989-1006.

Ulrich, M. R., and Bodnar, R. J., 1988, Systematics of stretching of fluid inclusions. II. Barite at one atmosphere confining pressure: Economic Geology, v. 83, p. 1037-1046.

Vityk, M. O., and Bodnar, R. J., 1995, Do fluid inclusions in high-grade metamorphic terranes preserve peak metamorphic density during retrograde decompression?: American Mineralogist, v. 80, p. 641-644.

Vityk, M. O., and Bodnar, R. J., 1998, Statistical microthermometry of synthetic fluid inclusions in quartz during decompression reequilibration: Contributions to Mineralogy and Petrology, v. 132, p. 149-162.

Tables

Table 1: Experimental conditions and microthermometric data for synthetic H_2O-NaCl fluid inclusions.

Run	P (MPa)	Th (°C)	Tm (°C)	n
102006-I	50	278.9	299.7	1
032305-II	50	312.5	336.9	1
032305-III	50	356.0	387.7	4
032305-V	50	470.9	480.1	7
071106-II	100	252.1	292.2	2
012405-II	100	281.7	337.3	3
012405-VI	100	327.8	390.8	4
012405-VII	100	378.9	442.9	2
061606-II	100	405.2	462.4	3
061606-I	100	406.7	468.2	5
012405-VIII	100	423.3	486.3	3
012405-IX	100	493.2	531.2	2
031705-I	200	202.5	291.1	1
031705-III	200	268.9	379.0	8
031705-IV	200	315.7	432.6	8
031705-V	200	352.8	473.9	6
031705-VI	200	415.9	528.5	6
051505-II	300	203.1	367.6	2
051505-III	300	241.1	419.3	5
051505-IV	300	287.5	471.0	6
051505-V	300	336.3	522.8	3
051505-VI	300	390.7	574.5	2

Table 2: Regression coefficients for Equation (1).

Coefficient	Value
$a_{0,0}$	-1.81686045E+5
$a_{0,1}$	-1.70660033E+2
$a_{0,2}$	9.21003065E-2
$a_{1,0}$	-2.99745046E+2
$a_{1,1}$	6.59084234E-1
$a_{1,2}$	-4.76501015E-4
$a_{2,0}$	2.69412137E-1
$a_{2,1}$	-7.93265819E-4
$a_{2,2}$	6.48940949E-7
b	-1.46975329E+4
c	5.37493440E+4

Table 3: Microthermometric data for FIAs hosted in fluorite from the Naica chimney-manto deposit.

FIA	Th (°C)	Tm (°C)
NFIA-1	237	339
NFIA-1	238	339
NFIA-1	244	338
NFIA-1	259	336
NFIA-1	265	338
NFIA-1	270	338
NFIA-1	257	340
NFIA-1	276	339
NFIA-2	240	309
NFIA-2	236	309
NFIA-2	249	309
NFIA-3	264	285
NFIA-3	271	285
NFIA-3	238	304
NFIA-3	249	304
NFIA-3	226	309
NFIA-3	218	285
NFIA-3	245	285
NFIA-3	248	304
NFIA-3	263	302
NFIA-3	210	296
NFIA-3	246	295
NFIA-3	250	297
NFIA-3	203	296
NFIA-3	275	292
NFIA-3	241	294
NFIA-3	253	294
NFIA-3	229	294
NFIA-3	248	294
NFIA-3	218	293

Table 4: Microthermometric data for inclusions from the QFIA-1 assemblage hosted in quartz from the Questa porphyry molybdenum deposit.

Inclusion	Th (°C)	Tm (°C)
1	337	407
2	334	450
3	324	392
4	333	387
5	351	391

Figures

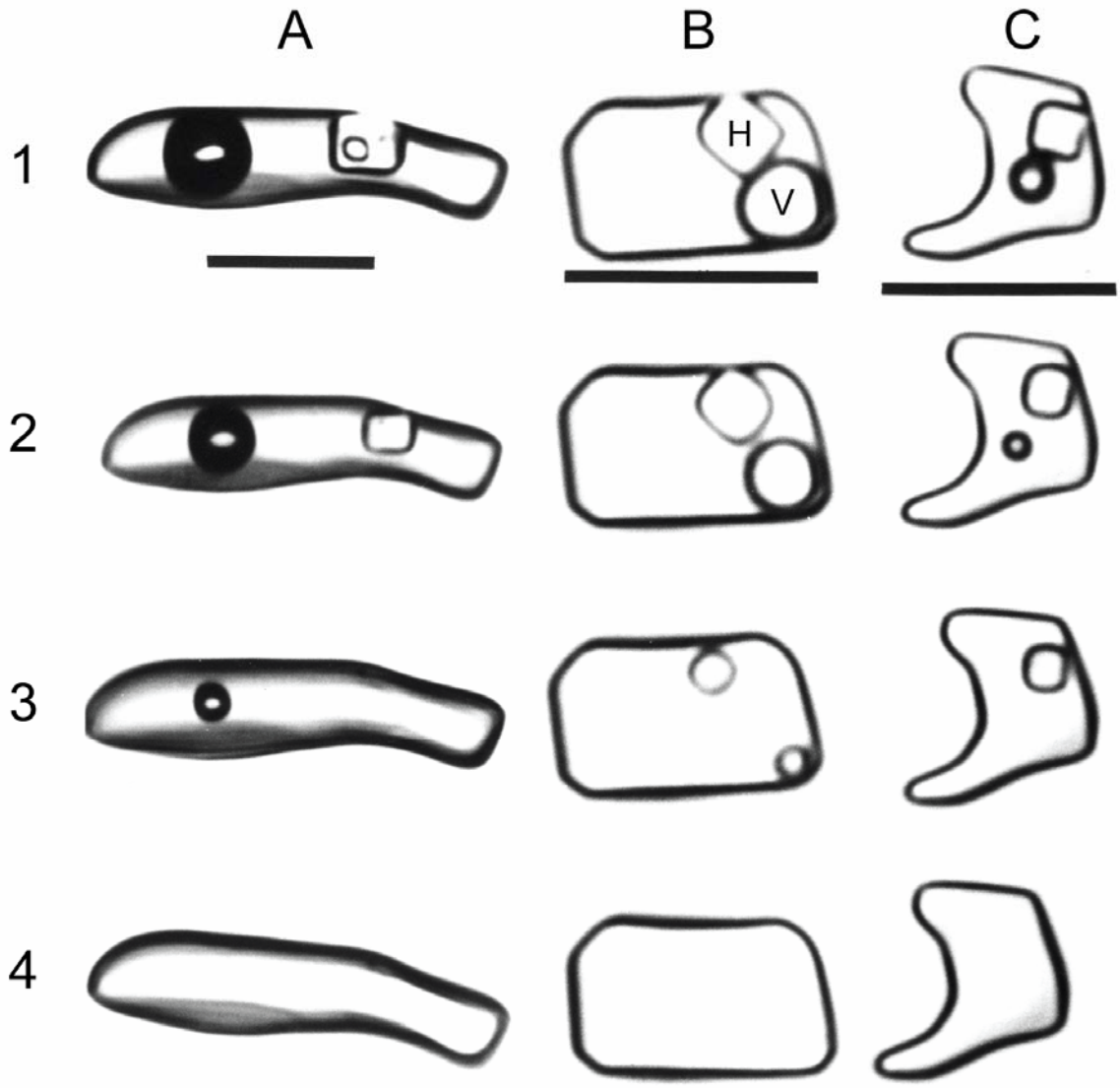

Figure 1. Series of photomicrographs showing the behavior during heating of synthetic, halite-bearing fluid inclusions that homogenize by three different modes. Column "A" shows an inclusion in which the halite daughter mineral dissolves first, followed by liquid-vapor homogenization. This mode of homogenization is referred to as mode "A". Column "B" shows an inclusion in which the halite daughter mineral and the vapor bubble disappear at the same temperature. This mode of homogenization is referred to as mode "B". Column "C" shows an inclusion in which liquid-vapor homogenization occurs first, followed by dissolution of the halite daughter mineral at some higher temperature. This mode of homogenization is referred to as mode "C". Image modified from Bodnar (1994).

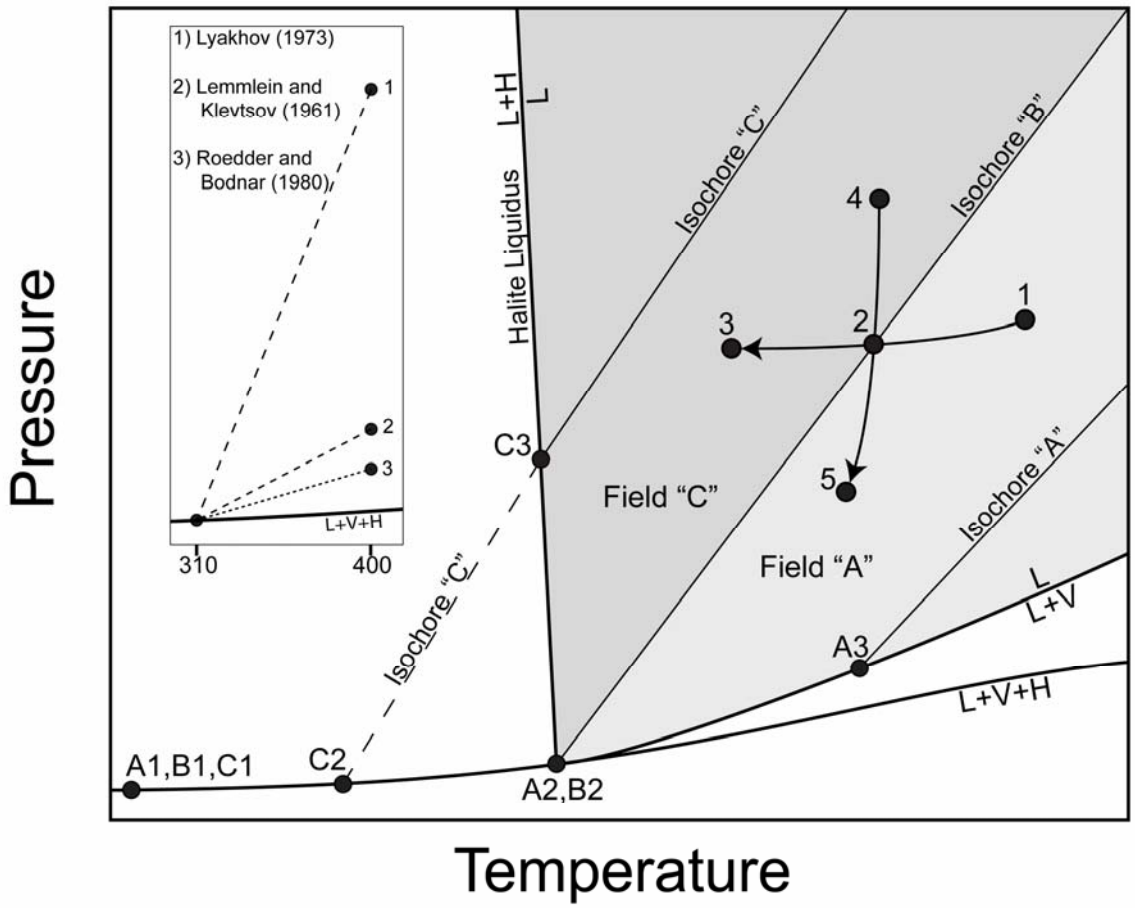

Figure 2. Schematic P-T phase diagram of the H_2O-NaCl system for some composition >~26.4 wt% NaCl (saturation at room temperature). Phase boundaries include the three-phase liquid+vapor+halite (L+V+H) curve, the two-phase liquid+vapor (L→L+V) curve, and the halite liquidus (L→L+H) where halite is in equilibrium with an NaCl-saturated liquid. Inclusions that homogenize by mode "B" could have been trapped at any point along isochore "B", which begins (points A2, B2) where the liquidus (L→L+H) and two-phase (L→L+V) curves intersect along the three-phase (L+V+H) curve. At room temperature (B1) an inclusion trapped along isochore "B" would contain liquid + vapor + halite. During heating the inclusion follows the L+V+H curve until the halite and vapor bubble both disappear simultaneously at B2. With continued heating the inclusion follows isochore "B" into the one-phase liquid field. Inclusions that homogenize by mode "A" could have been trapped anywhere within field "A", which is bounded at higher pressures by isochore "B" and at lower pressures by the two-phase (L→L+V) curve. At room temperature (A1) an inclusion trapped in field "A" would contain liquid + vapor + halite. During heating the inclusion follows the L+V+H curve until the halite disappears at A2 (defined by the intersection of the liquidus with the L+V+H curve). With continued heating the inclusion, which now contains liquid + vapor, follows the L→L+V curve until the vapor phase disappears (A3). With additional heating the inclusion follows isochore "A" into the one-phase liquid field. Inclusions that homogenize by mode "C" could have been trapped

anywhere within field “C”, which is bounded at higher temperatures by isochore “B” and at lower temperatures by the liquidus (L→L+H). At room temperature (C1) an inclusion trapped in field “C” would contain liquid + vapor + halite. During heating the inclusion follows the L+V+H curve until the vapor phase disappears at C2. With continued heating the inclusion, which now contains liquid + halite, travels through the liquid + halite field until the path intersects the halite liquidus (C3). With additional heating the inclusion follows isochore “C” into the one-phase liquid field. All three modes of homogenization are often observed in an individual deposit or sample. This may result from isobaric cooling of a fluid originally in field “A” (path 1→2→3) or isothermal decompression of a fluid originally in field “C” (path 4→2→5). The inset in the upper left shows pressures estimated by three different studies for a halite-bearing inclusion with $Th_{L\text{-}V}$ = 310°C and Tm_{halite} = 400°C.

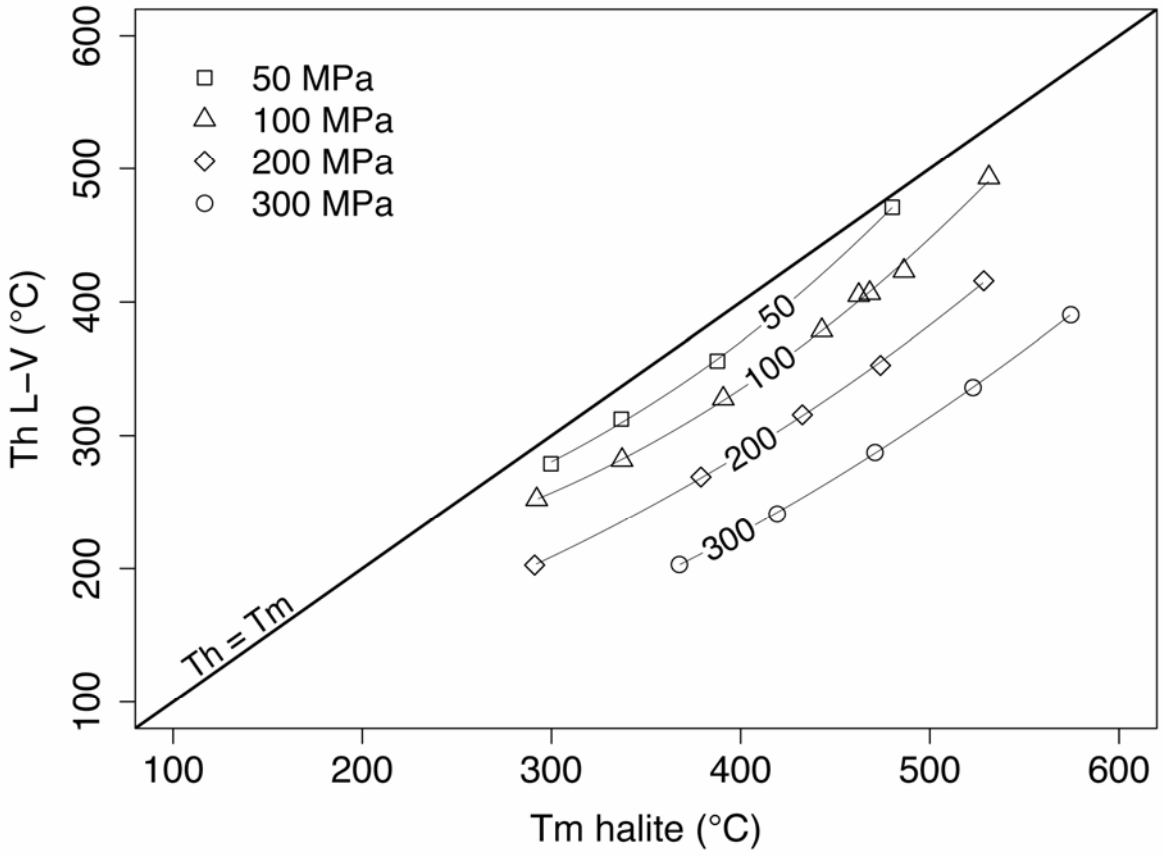

Figure 3. $Th_{L\text{-}V}$ versus Tm_{halite} for synthetic fluid inclusions in this study. $Th_{L\text{-}V}$ and Tm_{halite} vary smoothly and systematically between Tm_{halite} from ~300 to ~500°C for inclusions trapped at 50, 100, 200, and 300 MPa. The heavy diagonal line is the projection of the three-phase (L+V+H) curve in $Th_{L\text{-}V}$ versus Tm_{halite} space ($Th_{L\text{-}V} = Tm_{halite}$). Smooth lines through the data are spline functions showing trends in $Th_{L\text{-}V}$ and Tm_{halite} along each isobar.

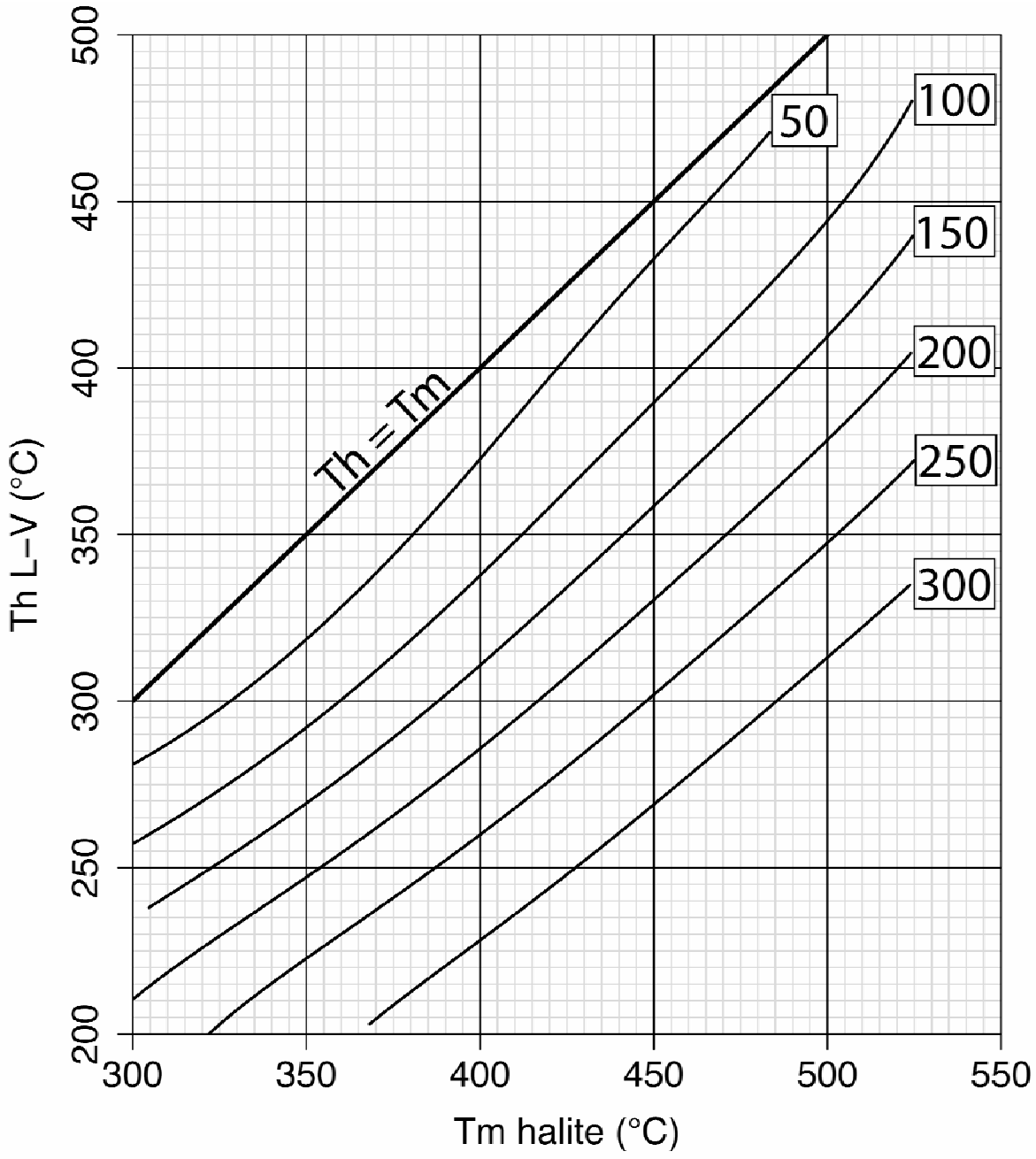

Figure 4. Smoothed isobars (MPa) in $Th_{L\text{-}V}$ versus Tm_{halite} space, generated using Equation (1).

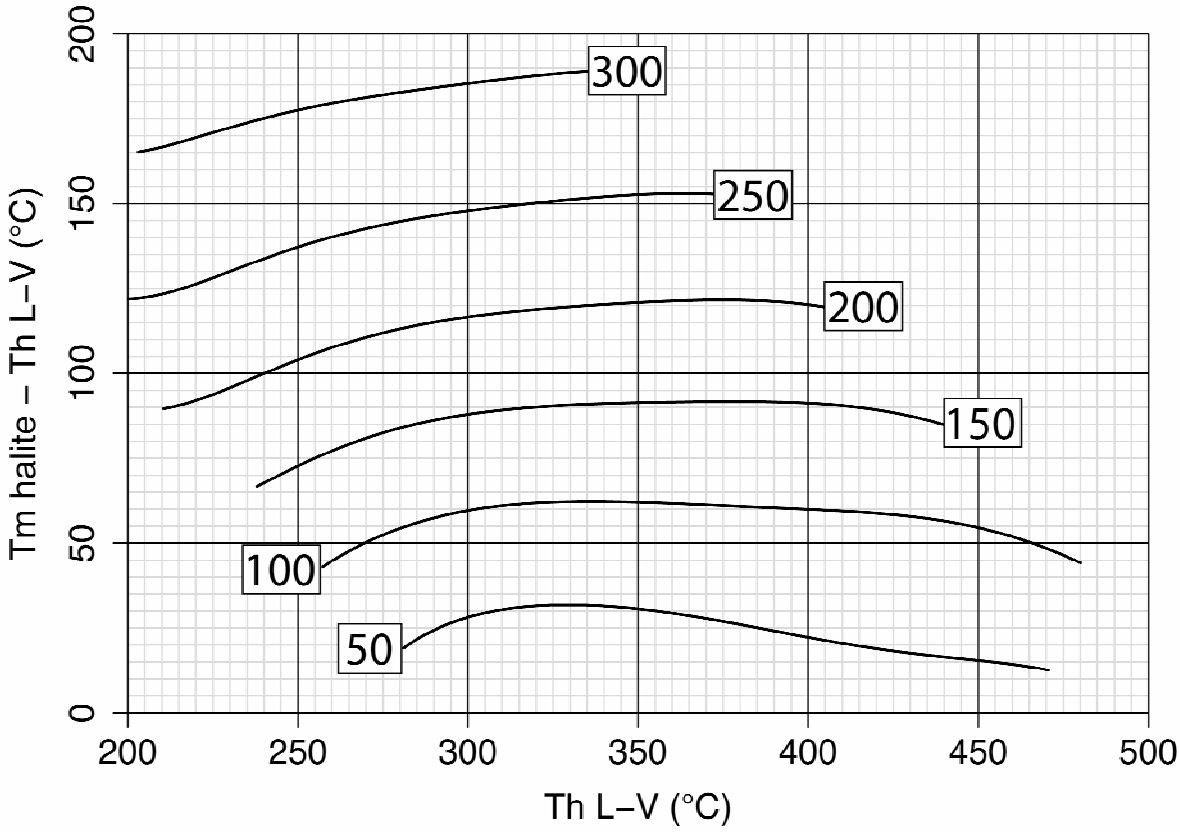

Figure 5. Smoothed isobars (MPa) in Tm_{halite}-$Th_{L\text{-}V}$ versus $Th_{L\text{-}V}$ space, generated using Equation (1).

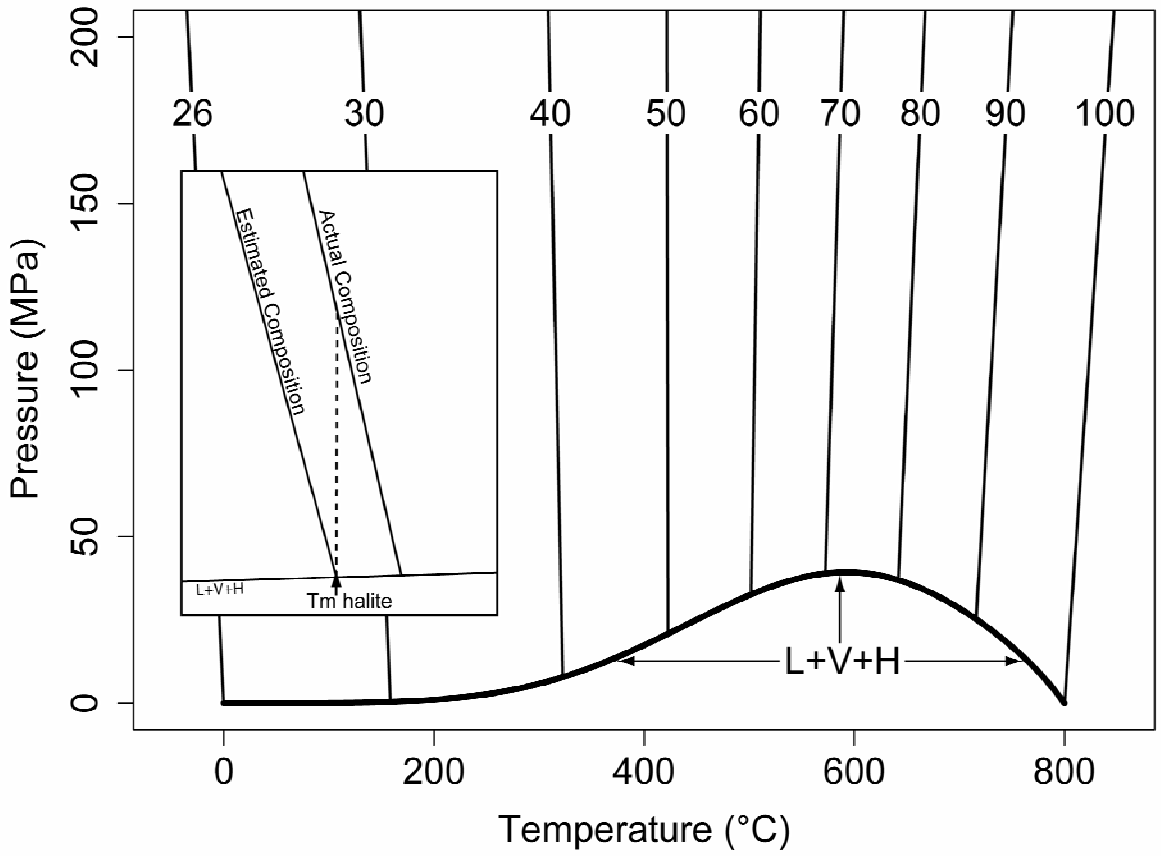

Figure 6. P-T phase diagram for the H_2O-NaCl system showing liquidi (labeled in wt% NaCl) for compositions between 26 and 100 wt. %, and from the vapor-saturated halite solubility (L+V+H) curve to 200 MPa. The inset on the left is a schematic representation of two liquidi, one that represents the liquidus that intersects the L+V+H curve at the temperature of halite disappearance for a type "C" inclusion, and the other corresponding to the actual liquidus for the inclusion. See text for details.

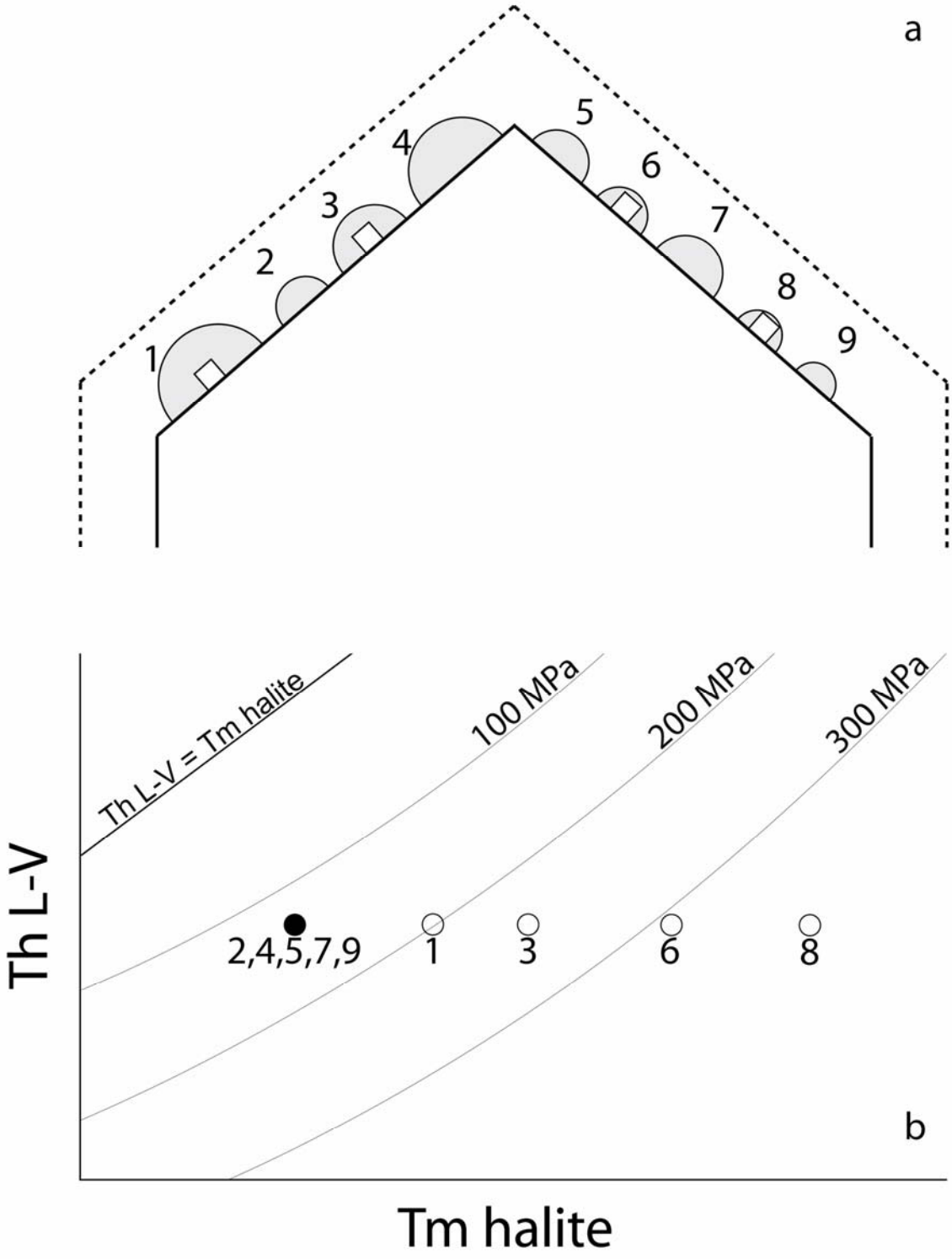

Figure 7. Schematic representation showing the relationship between Th_{L-V} versus Tm_{halite} for nine inclusions that were trapped on the liquidus. (a) Some inclusions will trap only the liquid phase (inclusions 2, 4, 5, 7 and 9) and others will trap various proportions of liquid

plus a halite crystal (inclusions 1, 3, 6 and 8). (b) All of the inclusions trapped on the liquidus have the same Th_{L-V} but show a range in Tm_{halite}. Inclusions that trap only the liquid phase (inclusions 2, 4, 5, 7 and 9) show the correct combination of Th_{L-V} and Tm_{halite} and will predict the correct pressure of trapping using Equation (1). Inclusions that trapped halite along with liquid (inclusions 1, 3, 6 and 8) have Tm_{halite} that are too high and will predict a pressure of trapping that is higher than the actual pressure.

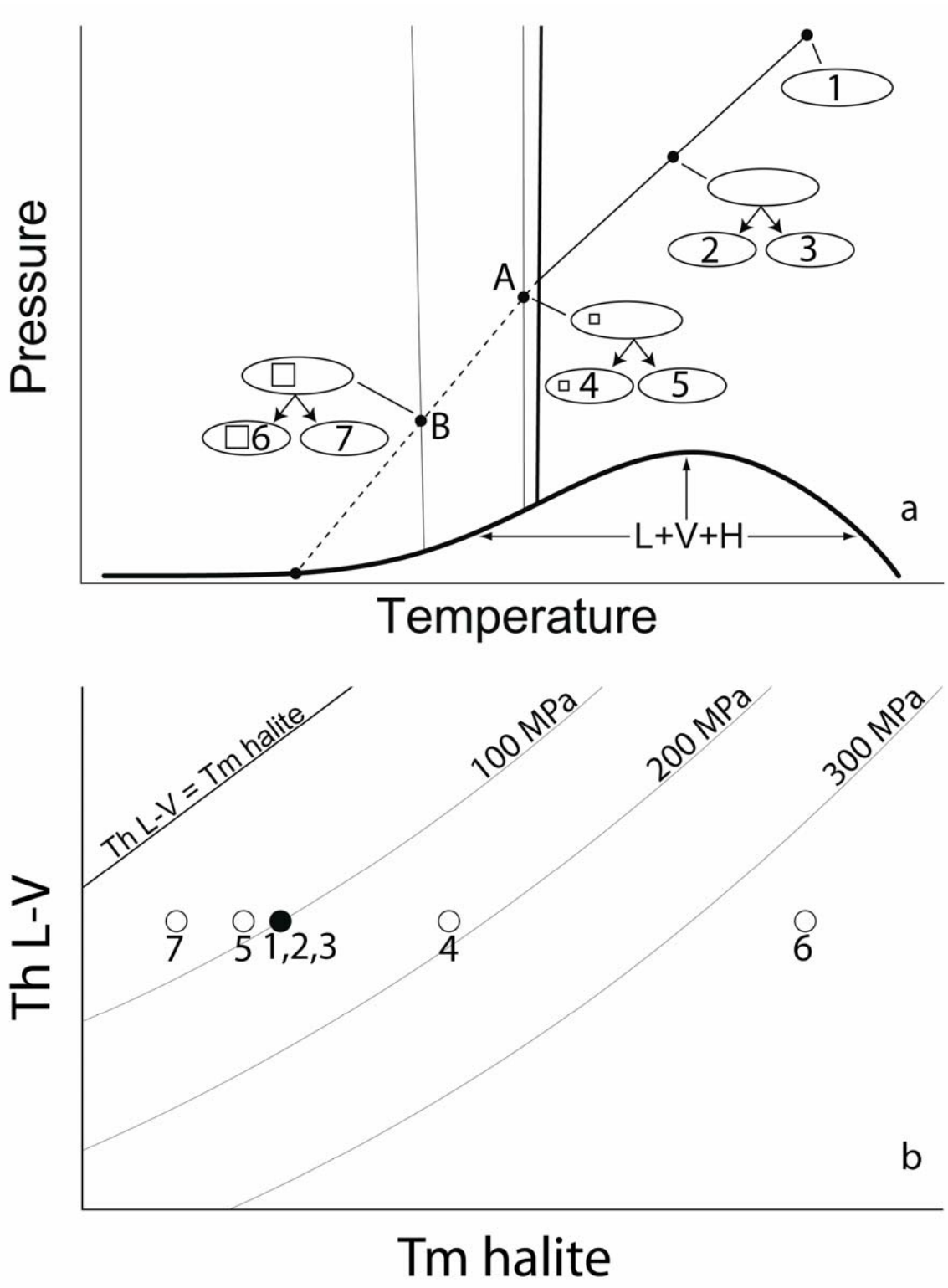

Figure 8. Schematic representation showing the relationship between Th_{L-V} versus Tm_{halite} for inclusions that neck during cooling. Inclusion 1 represents the original inclusion before necking, and the solid and dashed line extending to the L+V+H curve is the isochore

corresponding to the original trapping conditions. If necking occurs in the one-phase liquid field, inclusions (2 and 3) with the same density and composition as the original inclusion will be produced. If necking occurs after the P-T path has reached the halite liquidus (A), some inclusions (inclusion 4) may include a halite crystal in addition to liquid. The inclusion that necks with only liquid (inclusion 5) will have the same composition and density as the original inclusion, whereas the inclusion that necks with halite (inclusion 4) will have a higher salinity than the original inclusion. If necking continues at temperatures below the original liquidus temperature (B), some necked inclusions will contain only liquid (inclusion 7) whereas others will include halite + liquid (inclusion 6). Necking in a closed system produces inclusions with the same $Th_{L\text{-}V}$ but with widely varying Tm_{halite} (bottom). Moreover, it is not possible to know which of the $Th_{L\text{-}V}$ - Tm_{halite} combinations represents the original trapping conditions as Tm_{halite} may be lower than, higher than, or equal to the Tm_{halite} corresponding to the original trapping conditions, depending on whether necking occurred in the one-phase or two-phase field, and whether necking continued to temperatures below the original liquidus temperature.

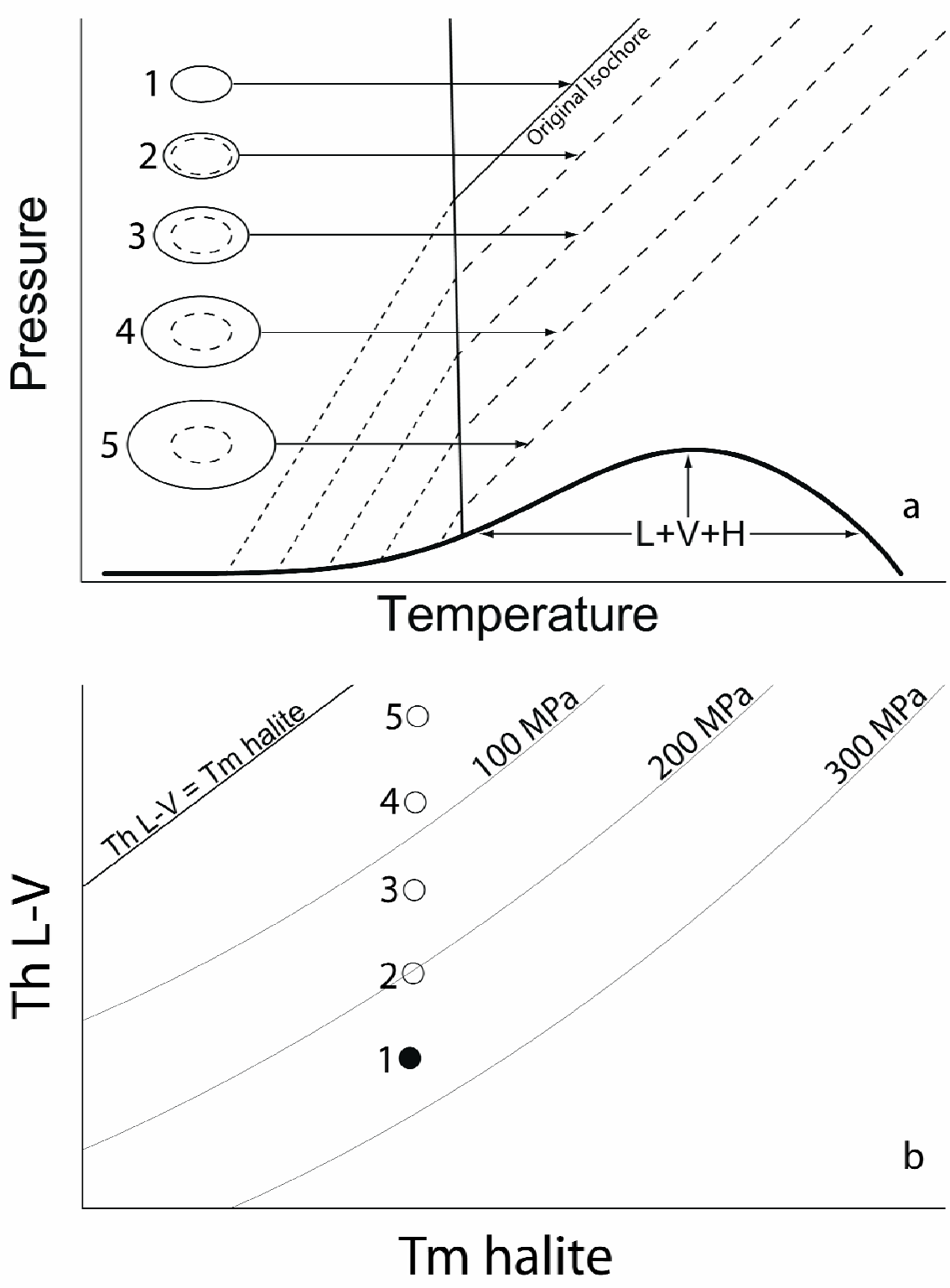

Figure 9. Schematic representation showing the relationship between Th_{L-V} versus Tm_{halite} for inclusions that stretch after trapping. Inclusion 1 represents the original inclusion before stretching, and inclusions 2-5 represent inclusions showing increasing amounts of stretching.

All of these inclusions will show essentially the same Tm_{halite}, but will display a wide range in $Th_{L\text{-}V}$. The inclusion with the lowest $Th_{L\text{-}V}$ (inclusion 1) represents the original trapping conditions.

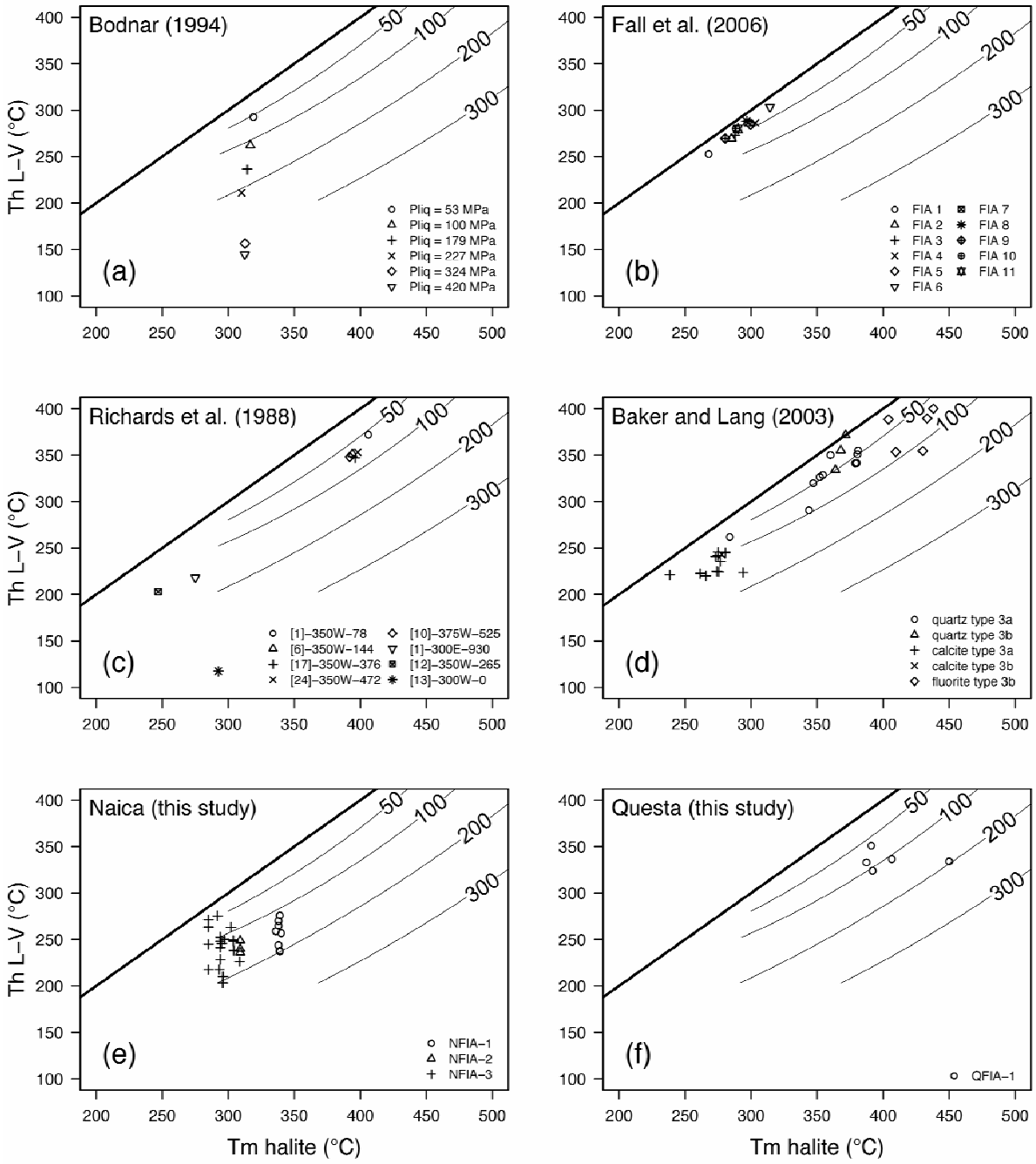

Figure 10. Series of $Th_{L\text{-}V}$ versus Tm_{halite} plots for synthetic and natural inclusions described in this study. Each plot displays the 50, 100, 200, and 300 MPa isobars as determined using synthetic fluid inclusions in this study. The heavy diagonal line is the projection of the vapor-saturated halite solubility curve in $Th_{L\text{-}V}$ versus Tm_{halite} space ($Th_{L\text{-}V} = Tm_{halite}$). (a) Selected data points for synthetic 40 wt% NaCl inclusions (Bodnar, 1994). Labels for data points indicate the liquidus pressure calculated by Bodnar (1994). (b) Average $Th_{L\text{-}V}$ versus Tm_{halite} for FIAs from the Ditrau alkaline massif (Fall et al., 2006). (c) Average $Th_{L\text{-}V}$ versus Tm_{halite} for inclusions hosted in quartz from the Musoshi, Zaire stratiform copper deposit (Richards et al., 1988). (d) Average $Th_{L\text{-}V}$ versus Tm_{halite} for inclusions hosted in quartz,

calcite, and fluorite from the Bismarck skarn deposit, Mexico (Baker and Lang, 2003). (e) $Th_{L\text{-}V}$ versus Tm_{halite} for individual inclusions in three fluorite-hosted FIAs from the Naica chimney-manto deposit, Mexico. (f) $Th_{L\text{-}V}$ versus Tm_{halite} for individual inclusions from a single quartz-hosted FIA from the Questa porphyry molybdenum deposit, New Mexico, USA.

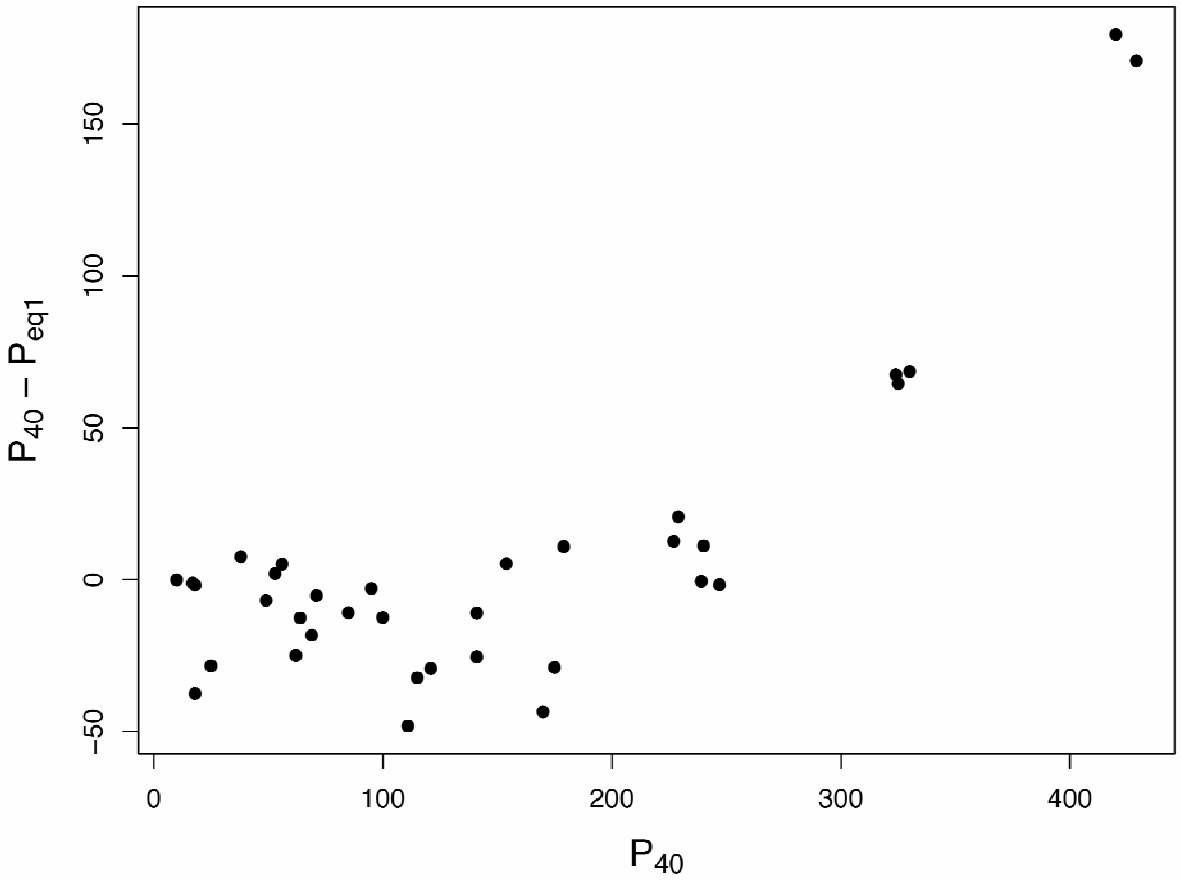

Figure 11. Comparison of calculated pressure along the 40 wt% liquidus (P_{40}) from Bodnar (1994) to the pressure calculated for the same inclusions using equation 1 (P_{eq1}). The agreement between these values is within approximately 50 MPa for inclusions with liquidus pressure up to ~250 MPa but become larger at higher pressures. See text for details.

Chapter 3: Temporal and Spatial Variations in Fluid Inclusion Characteristics in Porphyry Copper Deposits: Implications for Alteration and Exploration

Stephen P. Becker, Robert J. Bodnar, and T. James Reynolds
Fluids Research Laboratory, Department of Geosciences
Virginia Tech, Blacksburg, Virginia 24061, USA

Abstract

Porphyry copper deposits are associated with the emplacement and crystallization of silicic epizonal intrusions related to subduction zone magmatism. During crystallization, the magma becomes water-saturated. The large, positive volume change associated with exsolution of water from the magma results in an increase in pressure and concomitant fracturing of the overlying rocks. A network of veins is formed as fluids enter the fracture system and precipitate quartz and other minerals in response to cooling and decreasing pressure. Some of these fluids are trapped as fluid inclusions during the formation of veins, including high salinity liquid-rich inclusions, moderate-salinity liquid-rich inclusions, and low-salinity vapor-rich inclusions. The composition of the inclusions can be modeled based on the H_2O-NaCl system. A computer model was developed to predict the PVTX properties of fluids in the porphyry copper environment. Using this, the spatial and temporal distribution of fluid inclusion types, their compositions, and their homogenization behavior have been predicted. These results have implications for the association of magmatic fluids with alteration zones, and in the exploration for new prospects by predicting ones location within the overall porphyry environment based solely on fluid inclusion petrography.

Introduction

Porphyry copper deposits are formed in association with the emplacement and crystallization of silicic epizonal intrusions derived from hydrous arc magmas generated during partial melting of subducted oceanic crust (Sillitoe, 1972). Following a Burnham-style orthomagmatic model for the origin of porphyry systems (Burnham, 1997), these plutons may reach water saturation due to decompression (first boiling) or crystallization (second boiling). Second boiling is particularly important in generating the magmatic-hydrothermal system responsible for porphyry mineralization. The magma begins crystallizing from the margins inward, eventually becoming H_2O saturated, at which point any further crystallization will cause exsolution of an aqueous fluid phase (Burnham, 1997). Incompatible elements dissolved in the magma, including chlorine and copper, tend to partition into the aqueous phase, resulting in a metal-rich saline aqueous fluid (Candela, 1989; Candela and Holland, 1984; Cline and Bodnar, 1991; Holland, 1972; Kilinc and Burnham, 1972; Shinohara et al., 1989). The partial molar volume of H_2O dissolved in a silicic melt is less than the molar volume of the exsolved aqueous fluid, resulting in a concomitant pressure increase that hydrofractures the surrounding wall rocks (Burnham, 1997). The saline aqueous fluids flow along these fractures, altering the wall rocks and also precipitating minerals in the veins. Fluid inclusions are invariably trapped during the growth and subsequent refracturing of minerals in these veins throughout the life of the hydrothermal system (Bodnar, 1995; Roedder, 1984). Generally, these fluid inclusions fall into one of three categories: 1) high salinity inclusions containing liquid+vapor+salt±opaques at room temperature, 2) moderate salinity liquid-rich inclusions containing liquid+vapor±opaques at room temperature, or 3) low salinity vapor-rich inclusions containing liquid+vapor±opaques at room temperature. The bulk composition of these inclusions may be reasonably approximated by the binary H_2O-NaCl system.

Extensive experimental (Bischoff, 1991; Bischoff and Pitzer, 1989; Bodnar, 1985, 1994; Bodnar and Vityk, 1994; Haar et al., 1984; Haas, 1976; Keevil, 1942; National Research Council, 1928; Palliser and McKibbin, 1998a, b; Pitzer and Pabalan, 1986; Potter, 1977; Sourirajan and Kennedy, 1962; Sterner et al., 1988) and theoretical (Anderko and Pitzer, 1993; Duan et al., 2003; Kosinski and Anderko, 2001) descriptions of pressure-volume-temperature-composition (PVTX) relationships are reported for the H_2O-NaCl

system. Also, numerical models have been developed that describe the evolution of P-T conditions in time and space around cooling plutons based on fluid-flow (Cathles, 1977, 1981; Hayba and Ingebritsen, 1997; Knapp and Norton, 1981; Norton and Knight, 1977; Norton, 1982; Norton, 1984) and thermochronology (McInnes et al., 2005). Combined, it is possible to use these phase equilibria and fluid flow modeling studies to predict the PVTX characteristics of aqueous fluids at any point in time and space in a porphyry system, and then by extension to predict the types (high salinity, liquid-rich, and vapor-rich) and characteristics (homogenization temperature, phase ratios) of fluid inclusions that were trapped in time and space. In this study, we present a model for the temporal and spatial distribution of aqueous fluids present during the crystallization of a pluton associated with porphyry copper mineralization, and the types and characteristics of fluid inclusions trapped as magmatic aqueous fluids form veins throughout the surrounding rocks. This model provides a vectoring mechanism for porphyry systems based solely on fluid inclusion petrography, and has implications for exploration in environments where alteration and mineralization zoning may not be obvious.

Modeling

Geologic Model

A cross-section of a "typical" porphyry intrusion is shown in Figure 1 (Burnham, 1979). The pluton intrudes its overlying volcanic pile at shallow depths, and reaches water saturation due to crystallization (S_1) at a minimum depth of approximately 2 km (Fig. 1a). At this point, it is assumed that a saline fluid with a composition of 10 wt. % NaCl begins exsolving from the saturated melt, which will represent the bulk composition of the system at any point in time during the crystallization of the pluton. The salinity of an exsolved magmatic fluid is a function of both the chlorine content of the melt, and the pressure of the system (Cline and Bodnar, 1991). A composition of 10 wt. % NaCl is consistent with geochemical modeling of Cline and Bodnar (1991), and is also consistent with salinities of natural fluid inclusions (Bodnar, 1995). The position of the water saturated solidus (S_1-S_3) movies to greater depth as the pluton crystallizes inwards and downwards (Figs. 1a-1c).

The temperature at any location and time in the system was estimated based on models for the cooling of an epizonal pluton (Knapp and Norton, 1981). Knapp and Norton modeled the thermal history of points located within and above epizonal intrusions during hydrothermal fluid flow (Fig. 2). These data were used to estimate the positions of isotherms on Figures 1a-1d throughout the magmatic phase of the porphyry system. However, we recognize an inconsistency between the thermal models and the geologic model. The hydrothermal fluid-flow model assumes an intrusion instantaneously emplaced within a sequence of rocks with no pre-existing thermal anomaly (Knapp and Norton, 1981). The Burnham-style porphyry model portrayed in Figure 1 begins with an intrusion that was emplaced at a shallower depth and crystallized for some period of time prior to becoming water saturated. Therefore, the isotherms should probably be positioned closer to the surface in model A (Fig. 1a), which somewhat affects the size and position of phase stability fields discussed below, but not their relative positions.

The pressure at any location and time in the system was estimated by assuming that a hydrostatic (10 MPa/km) gradient applies from the surface to a depth corresponding to the 400°C isotherm, and that a lithostatic (30 MPa/km) gradient applies to depths below the 400°C isotherm, which may be calculated according to Equation 1:

$$P = (10MPa/km)(D1) + (30MPa/km)(D2 - D1) \qquad (1)$$

where P is pressure in MPa, $D1$ is either depth beneath the surface or to the 400°C isotherm (whichever is less), and $D2$ is depth beneath the surface.

Modeling Phase Boundaries

Four important phase stability fields are present in the H_2O-NaCl system over the range of temperatures and pressures of interest in a porphyry environment: one-phase liquid (L), one-phase vapor (V), two-phase liquid+vapor (L+V), and two-phase vapor+halite (V+H) (Fig. 3). In order to describe the PVTX properties of fluids in time and space, it is necessary to have an adequate mathematical description of the boundaries between these fields. One approach is to use a thermodynamically based theoretical equation of state (EOS) to describe the PVTX properties of H_2O-NaCl solutions. However, published EOS that describe H_2O-NaCl properties (Anderko and Pitzer, 1993; Duan et al., 2003; Kosinski and Anderko, 2001) require intensive calculations to solve, and are therefore non-trivial to apply. A second

approach to this problem is to use numerical methods (i.e. regression models, interpolation) to describe published PVTX data over the range of temperature relevant to porphyry mineralization, or when available, to use published equations describing PVTX properties of H_2O-NaCl fluids. This second approach was deemed more practical for the purposes of this study. Subsequently, data from experimental and theoretical studies were compiled from available literature, and regressed to produce algorithms suitable to describe properties of interest. All regression models were developed using the R project for statistical computing (R Development Core Team, 2007). Previously published equations describing H_2O-NaCl equilibrium were used when deemed appropriate (Palliser and McKibbin, 1998a, b; Sterner et al., 1988).

The one-phase field is separated from the two-phase L+V field by the liquid-vapor equilibrium surface. Liquid-vapor PVTX equilibrium is described over a range from 80-900°C by experimental and theoretical studies (Anderko and Pitzer, 1993; Bischoff, 1991; Bischoff and Pitzer, 1989; Haas, 1976). A stepwise regression model of pressure as a function of temperature and composition was developed using data from these sources to calculate liquid-vapor equilibrium in this study. Developing a precise regression model relating density to pressure, temperature, and composition along the liquid-vapor surface could not be accomplished owing to the complexity of PVTX 4-dimensional space. Instead, a compilation of all the PVTX data in the range of 80-300°C was used with the "loess" function of R (R Development Core Team, 2007) to interpolate density as a function of temperature and composition along the liquid-vapor surface.

The two-phase liquid+vapor field is bounded at low pressures by the vapor-saturated halite solubility (L+V+H) curve. The equation of Sterner et al. (1988) was used to describe the T-X projection of the L+V+H curve for H_2O-NaCl solutions. Palliser and McKibbin (1998b) provide an equation describing density as a function of temperature along the L+V+H curve. Data for the P-T projection of the L+V+H curve (Bischoff, 1991; Bischoff and Pitzer, 1989; Keevil, 1942; National Research Council, 1928; Pitzer and Pabalan, 1986; Sourirajan and Kennedy, 1962) were compiled and regressed to produce an equation describing pressure as a function of temperature.

The density of halite-undersaturated liquid between 0 and 26.4 wt. % NaCl at room temperature (25ºC) is reported by Potter (1977). A regression model was developed using

these data combined with endpoint densities of 0 and 26.4 wt. % fluids (Haar et al., 1984; Palliser and McKibbin, 1998b) so that halite undersaturated fluid densities could be precisely determined for compositions outside the range reported by Potter.

The one-phase liquid field is separated from the one-phase vapor field by the critical isochore for the bulk salinity of the liquid. Fluids in the one-phase field with densities greater than the critical density are in the one-phase liquid field; fluids in the one-phase field with densities less than the critical density are in the one-phase vapor field. An equation that describes the slopes of isochores extending into the one phase field as a function of temperature and pressure along the liquid-vapor surface for compositions up to 40 wt. % NaCl (Bodnar and Vityk, 1994) was used in combination with previously described functions to determine the phase state of the H_2O-NaCl fluid at any PTX condition.

Computer Modeling

The relationships described above were used to develop a computer model that predicts the density and phase state of fluids in the H_2O-NaCl system as a function of temperature, pressure, and composition. This model was coded in a combination of FORTRAN subroutines and R functions (see Appendices B and C). The model is valid from 80 to 900°C. For liquid-vapor equilibrium below 380°C, the composition of coexisting vapor is assumed to be 0 wt. % NaCl. Above 500°C, the model is only valid at pressures of 40 MPa and above. However, pressures <40 MPa at temperatures >500°C are rarely predicted by the cooling models. Input is total depth, depth to the 400°C isotherm, temperature, and bulk composition. The pressure is calculated from the input depths according to Equation 1, and the input PTX conditions are evaluated using equations described above to determine the phase stability field and densities. Using an iterative approach, the composition of coexisting phases and homogenization temperatures are calculated when appropriate. The phase ratios that would be present in fluid inclusions at room temperature were then calculated using the bulk density of the inclusion and the densities of phases present at room temperature (Bodnar, 1983).

To map out the phase fields on the geologic model presented in Figures 1a-1d, the depth to 100 to 900°C isotherms was determined. As stated above, phase fields were calculated assuming a bulk composition of 10 wt. % NaCl for the fluid exsolving from the

crystallizing magma. This composition represents a reasonable estimate for the composition of primary magmatic aqueous phases exsolving from a pluton at a pressure of approximately 100 MPa (Cline and Bodnar, 1991). However, it is possible that high salinity brine may exsolve directly from a melt (Bodnar, 1994; Cline and Bodnar, 1994). This is not considered problematic because for salinities up to ~40 wt. % over the range of temperature and pressure consistent with porphyry copper mineralization, the position of H_2O-NaCl isopleths in P-T space are relatively insensitive to small changes in salinity and would not significantly change except at high temperature and pressure (Fig. 4).

Results

Geologic Model and Phase Stability Fields

The H_2O-NaCl phase fields at different times during the crystallization of the pluton display the evolution of phase stability fields, including one-phase liquid (blue), one-phase vapor (green), two-phase liquid+vapor (L+V) (yellow), and two-phase vapor+halite (V+H) (purple) (Figs. 3, 5-8). The red shaded region represents a water-undersaturated hydrous melt at or above 1000°C (Figs. 5-8). The region between the solidus ($S_1/S_2/S_3$) and the 1000°C isotherm represents the water-saturated carapace where crystals+melt+aqueous phases coexist. Early in the evolution of a porphyry system, magmatic fluids tend to be laterally restricted to a region corresponding to the width of the intrusion. Meteoric fluids dominate from the margins of the system out into the surrounding wall rocks. Thus, it is not likely that the one-phase field adjacent to the flanks of the system has salinity as high as that of the magmatic fluid. However, the one-phase liquid field for a very low salinity meteoric fluid should not significantly differ from that of the magmatic fluid except at high P-T conditions that are not encountered in the one-phase stability field on these models (Fig. 4), so modeling based on a 10 wt. % bulk composition is sufficient for the purposes of this study. During later stages of the crystallization of the pluton, the boundary between one-phase meteoric water and one-phase magmatic fluid will descend according to the downward migration of the brittle-ductile transition. The implications of this will be discussed in more detail below.

Model A (Fig. 5) represents the earliest stage during the evolution of the porphyry system where an aqueous phase begins exsolving from the pluton at a minimum depth of approximately 2 km. At this time, the water-saturated carapace at the top of the pluton is relatively close to the surface, where pressure is low and the temperature is high. Here, P-T conditions in the water saturated carapace are such that the magmatic aqueous phase enters the two-phase L+V field at the instant it separates from the magma, which dominates much of the system. Any fluids that are able to ascend eventually cross into the two-phase V+H field as they cross a P-T condition along the three-phase L+V+H curve between 1 and 2 km depth. This stability field has important implications for shallow alteration of the system, and will be discussed in more detail below. At deeper levels of the system along the flanks, the L+V field pinches out between two "fingers" where a single-phase vapor is stable. Where the vapor field is in direct contact with the magma, the composition represents the bulk composition of the primary magmatic aqueous fluid. If this vapor were to ascend, it would intersect the two-phase field and condense into high salinity brine coexisting with low salinity vapor. Model A (Fig. 5) also has five vertical lines superimposed from the center to the flanks of the system. P-T paths for the intersection of isotherms with these lines have been plotted on a phase diagram of the H_2O-NaCl system for a bulk composition of 10 wt. % to provide a visual representation of the change of stability field with depth (Fig. 9).

Model B represents a time when the crystallization of the pluton has proceeded to a minimum depth of approximately 4 km, and is very similar to model A in terms of the relative positions of the phase stability fields (Fig. 6). However, the extent of the two-phase V+H field has become smaller, and a single-phase magmatic vapor dominates the deeper flanks of the system. As with model A, ascent of this single-phase vapor towards the center of the system will intersect the two-phase field and condense into high salinity brine coexisting with a low salinity vapor. It is likely that meteoric water has begun to circulate through the upper parts of the system above the brittle-ductile transition at the point. As with Model A, P-T paths are plotted for the five lines superimposed on Model B (Fig. 10).

Model C represents a time when the crystallization of the pluton has proceeded to a minimum depth of approximately 7 km (Fig. 7). Alternatively, this model could be used to represent the early crystallization of a deep pluton, analogous to a system such as Butte (Bodnar, 1995; Rusk et al., 2004; Sillitoe, 1973). At this point, the primary magmatic

aqueous phase is stable as single-phase vapor extending out from the water-saturated carapace along the flanks and at the center of the system. As this fluid ascends, its density will continuously increase as it contracts with decreasing temperatures, eventually becoming greater than the critical density to exist as a single phase fluid with a liquid-like density. P-T paths for the five lines superimposed on model C illustrate this (Fig. 11). The consequence of this is that from the water-saturated carapace up to the brittle-ductile transition, a single-phase liquid having a primary magmatic composition will be stable. This has implications for late alteration products and copper mineralization, and will be discussed in detail below.

Model D represents a time at the end of the life of the magmatic system when the pluton has completely crystallized, but the thermal anomaly associated with the system still exists (Fig. 8). Here, meteoric water begins to dominate the entire system, although there may still be components of magmatic aqueous fluid present at deep levels. The entire system is in the one-phase field with respect to a bulk salinity of 10 wt. % NaCl and lower salinities (Fig. 4). A P-T path diagram is not presented for this model.

Spatial and Temporal Distribution of Fluid Inclusions

Along each of lines 1-5, four evenly spaced points were chosen beginning at 1.5 km depth and then every 2 km beyond that to a total depth of 7.5 km (Figs. 5-8). The fluid inclusion characteristics at each of these points were calculated using the modeling software developed for this study. These data were then used to produce a set of tables displaying the evolution of fluid inclusion types and characteristics in time and space (Figs. 12-16). Fluid inclusions in these tables are pictured as they would appear at room temperature, where the grey-shaded circles or ellipses represent a vapor phase, the squares represent halite, and the remaining area is liquid. Any one table displays the fluid inclusion characteristics for a single line at depths from 1.5-7.5 km over four columns corresponding to the same line on model A through model D, including salinity (or salinities), homogenization temperature, and the phase stability field in which the inclusion or inclusions was/were trapped.

At the outermost margin of porphyry model (lines 1-2, Figs. 5-8), the system remains in the single-phase field throughout the entire crystallization history, and thus all fluid inclusions trapped along this line appear as simple two-phase L+V inclusions at room temperature (Figs. 12-13). Owing to the increase in temperature with depth, the

homogenization temperatures of these inclusions increase as the bulk density decreases towards the bottom of the system (Figs. 12-13). Lines 1-2 remain in the single-phase liquid stable field for the entire life of the system down to a depth of 7.5 km except for the bottom of line 2, which lies within the single-phase vapor stable field for the first two time-slices (Figs. 5-6), which results in the formation of vapor-rich inclusions at the base of line 2 (Fig. 13).

From the middle-flank to the center of the porphyry model (lines 3-5, Figs. 5-8), the fluid inclusion characteristics become more variable (Figs. 14-16). Early during the crystallization of the pluton, these lines pass through a significant "thickness" of the system in the two-phase L+V field where high salinity brine coexists with low salinity vapor. This results in the entrapment of coexisting high salinity brine inclusions having bulk salinities greater than the solubility of NaCl at room temperature and low salinity vapor-rich inclusions. The brine inclusions contain NaCl saturated liquid, halite, and a vapor bubble at room temperature, whereas the vapor rich inclusions will contain a vapor bubble that occupies most of the volume of the inclusion at room temperature. Because these coexisting inclusions were trapped at the same P-T conditions along a phase boundary, they will have homogenization temperatures equivalent to the temperature at which they were trapped. However, in reality the surface of fractures and minerals is "wetted" by the high salinity liquid phase, resulting in heterogeneous trapping of liquid and vapor in the vapor-rich inclusions, lowering the measured homogenization temperature and increasing the bulk salinity of the vapor-rich inclusions (Roedder, 1984).

Towards the center of the intrusion of models A and B at shallow levels (lines 4-5, Fig. 5-6), the lines intersect the two-phase V+H field. Here, halite would begin precipitating in open spaces, possibly becoming trapped as mineral inclusions. A very low salinity vapor is trapped as vapor-rich inclusions with almost no visible liquid at room temperature. The homogenization temperatures of these inclusions are not calculated, as the computer model does not include the PVTX properties of fluids in the V+H field. With progressive crystallization to model C (Fig. 7), the shallow levels of the center of the intrusion lie within the single-phase liquid field, while the deeper levels lie with the single-phase vapor field. As noted previously, this vapor would be a primary magmatic fluid. Furthermore, the density of this vapor would be very close to the critical density, resulting in the entrapment of vapor-

rich inclusions having liquid and vapor at room temperature that display "near-critical" homogenization behavior (Figs. 13-16) (Roedder, 1984).

With progression to model D where the entire system is in the one-phase liquid stable field (Fig. 8), all inclusions from the flank to the center of the system would appear as simple two-phase L+V inclusions at room temperature, having increasing homogenization temperatures with increasing depth of entrapment (Figs. 12-16).

Discussion

Exploration Applications

The utility of Figures 12-16 are that they predict a sequence of fluid inclusions that one would expect to see at any point from the center to the periphery and from the top to the bottom of the overall porphyry environment. Consider exploration activities in a humid, tropical environment where exposed rocks containing silicates such as feldspars and micas indicative of alteration zones have succumbed to chemical weathering. In such an environment, all that may be left of the original rocks are clays, and pieces of quartz phenocrysts and veins that contain fluid inclusions. Using only petrographic techniques, it is then possible to use undisturbed fluid inclusions that were trapped in the chemically stable quartz to indicate one's position in the overall porphyry environment by providing vectors towards the center of the magmatic-hydrothermal system.

For example, a sequence beginning with inclusion-free phenocrysts (possibly containing melt inclusions) that were subsequently cross-cut by trails of inclusions containing coexisting brine and vapor-rich inclusions, which in turn were cross-cut by trails of vapor-rich inclusions of the critical or near-critical type having lower homogenization temperatures, which were then cross-cut by trails of liquid-rich inclusions having even lower homogenization temperatures would be indicative of a relatively deep position within a pluton that intruded to shallow depths (row 4 – 5.5 km, Fig. 15).

In another example, a sequence of four vein fragments collected along a traverse may indicate increasing depth within the system (e.g. column B, Fig. 14). The first sample hosts abundant two-phase liquid-rich inclusions, the second sample hosts boiling assemblages where the brine inclusions had relatively small halite crystals, the third sample hosts boiling

assemblages having a higher temperature with larger halite crystals, and the fourth sample hosts abundant vapor-rich inclusions of the critical or near-critical type.

Of course, we recognize that this is a rather crude oversimplification of reality. Phenocrysts and veins in typical porphyry environments may host hundreds if not thousands of generations of fluid inclusions. It is often difficult to unambiguously identify fluid inclusion assemblages (or FIAs—a population of fluid inclusions trapped at the same time from the same fluids at the same P-T conditions) and/or determine the relative ages of FIAs. Therefore, this technique requires strategic sampling/selection and careful petrography to be useful.

Significance of the Vapor+Halite Stability Field

Shallow (<3-4 km) intrusions are likely to generate hydrothermal systems that extend into the L+V and V+H stability fields (Fournier, 1987), which is consistent with the presence of the L+V and V+H fields on models A and B (Figs. 5-6). Fournier (1987) acknowledges the V+H field as an environment where the hydrolysis of salt generates acid gases (HCl and H_2SO_4) and hydroxides (NaOH and $Ca(OH)_2$). Alteration products are then formed from reactions between the hydroxides and silicate wall rocks, including epidote, albite, and chlorite. The zone of acid alteration is important at lower pressures, and is therefore only likely to be observed associated with shallow intrusions (Fournier, 1987). This has important implications for exploration, as the presence of acid alteration is indicative of the proximity of the intrusion to the paleosurface, the amount of erosion that has occurred, and one's position in the overall porphyry environment.

A Magmatic Source for Phyllic Alteration

Phyllic (or sericitic) alteration, consisting of quartz, sericite, and pyrite, is a characteristic feature of porphyry copper systems, occurring as a halo surrounding and overprinting early potassic alteration (Guilbert and Lowell, 1974; Lowell and Guilbert, 1970). Many early isotopic studies of porphyry copper deposits of the southwestern United States seemed to indicate a significant meteoric contribution to a low-salinity fluid (compared to the earlier high salinity brines associated with boiling and potassic alteration)

responsible for phyllic alteration and the precipitation of ore minerals (Sheppard et al., 1971; Taylor, 1974, 1997). This appeared to be supported by fluid inclusion studies linking later, low salinity fluid inclusions to copper mineralization (Bodnar, 1995). However, more recent studies imply a magmatic source for these late, moderate to low salinity fluids associated with phyllic overprinting and the precipitation of copper ore (Harris and Golding, 2002; Hedenquist et al., 1998; Hedenquist and Richards, 1998; Rusk et al., 2004; Shinohara and Hedenquist, 1997). Hedenquist et al. (1998) recognized this link while definitively ruling out a meteoric component at the Far Southeast-Lepanto system, where the late phyllic overprint associated with euhedral quartz veins having halos of sericite alteration was attributed to a low salinity (~5 wt. %) fluid that had a dominantly magmatic isotopic composition.

Modeling of the Far Southeast-Lepanto system suggests that rapid exsolution and ascent of magmatic fluid during the early stages of the system form a plume of magmatic fluid that intersects the two-phase field (e.g. Figs. 9-10), resulting in high salinity brine responsible for potassic alteration in the core of the system, and low salinity vapor responsible for argillic alteration near the edges of the system (Shinohara and Hedenquist, 1997). After this initial stage, the magmatic aqueous flux decreases, and the fluids ascend along a P-T path that does not intersect the two-phase field (e.g. Fig. 11), resulting in the system being flooded with a moderate to low salinity magmatic fluid component that is responsible for phyllic alteration and precipitation of Au-Cu ore. This interpretation is in near perfect agreement with porphyry models A-C (Figs. 5-7, 9-11). In particular, model C implies the presence of a magmatic vapor phase exsolving from the remaining melt at depths exceeding 6 km. As this vapor ascends, it will contract to a fluid having a liquid-like density at depth of 5-6 km. The entire region underneath the brittle-ductile transition (i.e. the 400°C isotherm) will be dominated by this primary magmatic fluid. This fluid may then ascend to shallower depths during periodic fracturing events that allow deeper fluids under lithostatic pressure to escape to the brittle regime. This interpretation is consistent with a magmatic source for late phyllic alteration and mineralization described by Hedenquist et al. (1998) and others.

Summary

A computer model based on PVTX properties of the H_2O-NaCl system was used to predict the characteristics of fluids in time and space in a porphyry copper environment. Modeling the compositions of fluids derived from exsolved aqueous fluids in a porphyry copper environment based temporal and spatial evolution of pressure and temperature has made it possible to predict the PVTX characteristics of fluids in the overall porphyry environment, and by extension to predict the fluid inclusion characteristics in time and space. This modeling shows that early in the crystallization of shallow plutons, the system is dominated by liquid+vapor stability, with a smaller but significant field of vapor+halite stability at the top of the system. As the crystallization of the pluton progresses inwards and downwards, the isotherms collapse downward, and the V+H and L+V field shrink as single-phase vapor stability becomes more important. Late in the system, the isotherms have collapsed far enough that primary magmatic aqueous fluid does not intersect the two-phase L+V field, allowing this primary magmatic fluid to escape to shallower depths where it may be involved in late alteration and mineralization.

As a consequence of the fracturing and vein formation associated with the evolution of aqueous phases, many generations of fluid inclusions are trapped throughout the life of the hydrothermal system. The characteristics of these inclusions have been predicted based upon the computer model. In general, early times during the evolution of the system will be characterized by sequences of coexisting high salinity liquid-rich and low salinity vapor-rich inclusions at the center of the system to two-phase liquid-rich or vapor-rich inclusions at the edge of the system (Figs. 5, 12-16). As crystallization of the porphyry pluton proceeds, vapor-rich inclusions will begin to dominate the flanks of the system as the L+V and V+H fields shrink (Figs. 6, 12-16). Late in the system (or early in the crystallization of a deep system), primary magmatic aqueous fluid dominates the lithostatic regime from the center to the flanks, resulting in the formation of critical or near-critical types of inclusions (Figs. 7, 12-16). Post-magmatic fluid flux of meteoric water in the one-phase liquid stable field results in the entrapment of low salinity, two-phase liquid-rich inclusions.

Using the distribution of fluid inclusions modeled after the evolution of fluid inclusions in time and space, it is then possible to predict one's position in the overall porphyry environment based solely on fluid inclusion petrography. This has implications for

exploration by providing vectors towards the center of the magmatic-hydrothermal system in regions where other indicators of position with the porphyry environment, such as alteration zones, are not useful.

Acknowledgements

The authors thank David Dolejš for providing a computer program that implements the Anderko and Pitzer EOS for H_2O-NaCl solutions.

References

Anderko, A., and Pitzer, K. S., 1993, Equation-of-state representation of phase equilibria and volumetric properties of the system NaCl-H_2O above 573 K: Geochimica et Cosmochimica Acta, v. 57, p. 1657-1680.

Bischoff, J. L., 1991, Densities of Liquids and Vapors in Boiling NaCl-H_2O Solutions: a PVTX summary from 300° to 500°C: American Journal of Science, v. 291, p. 309-338.

Bischoff, J. L., and Pitzer, K. S., 1989, Liquid-Vapor Relations for the System NaCl-H_2O: Summary of the P-T-x Surface from 300° to 500°C: American Journal of Science, v. 289, p. 217-248.

Bodnar, R. J., 1983, A Method of Calculating Fluid Inclusion Volumes Based on Vapor Bubble Diameters and P-V-T-X Properties of Inclusion Fluids: Economic Geology, v. 78, p. 535-542.

Bodnar, R. J., 1985, Pressure-Volume-Temperature-Composition (PVTX) properties of the system H_2O-NaCl at elevated temperatures and pressures: Unpub. PhD Dissertation thesis, The Pennsylvania State University, 183 p.

Bodnar, R. J., 1994, Synthetic fluid inclusions. XII. Experimental determination of the liquidus and isochores for a 40 wt.% H_2O-NaCl solution: Geochimica et Cosmochimica Acta, v. 58, p. 1053-1063.

Bodnar, R. J., 1995, Fluid inclusion evidence for a magmatic source for metals in porphyry copper deposits, *in* Thompson, J. F. H., ed., Mineralogical Association of Canada Short Course Volume 23, 23, p. 139-152.

Bodnar, R. J., Burnham, C. W., and Sterner, S. M., 1985, Synthetic fluid inclusions in natural quartz. III. Determination of phase equilibrium properties in the system H_2O-NaCl to 1000°C and 1500 bars.: Geochimica et Cosmochimica Acta, v. 49, p. 1861-1873.

Bodnar, R. J., and Vityk, M. O., 1994, Interpretation of microthermometric data for H_2O-NaCl fluid inclusions, *in* de Vivo, B., and Frezzotti, M. L., eds., Fluid Inclusions in Minerals, Methods and Applications: Blacksburg, VA, Virginia Tech, p. 117-130.

Burnham, C. W., 1979, Magmas and hydrothermal fluids., *in* Barnes, H. L., ed., Geochemistry of Hydrothermal Ore Deposits: New York, John Wiley & Sons, p. 71-136.

Burnham, C. W., 1997, Magmas and hydrothermal fluids, *in* Barnes, H. L., ed., Geochemistry of Hydrothermal Ore Deposits: New York, Wiley and Sons, p. 63-123.

Candela, P. A., 1989, Magmatic ore-forming fluids: thermodynamic and mass-transfer calculations of metal concentrations., *in* Whitney, J. A., and Naldrett, A. J., eds., Ore Deposition Associated with Magmas, 4. Reviews in Economic Geology: El Paso, TX, Economic Geology Publishing Company, p. 203-221.

Candela, P. A., and Holland, H. D., 1984, The partitioning of copper and molybdenum between silicate melts and aqueous fluids: Geochimica et Cosmochimica Acta, v. 48, p. 373-380.

Cathles, L. M., 1977, An analysis of the cooling of intrusives by ground-water convection which includes boiling: Economic Geology, v. 72, p. 804-826.

Cathles, L. M., 1981, Fluid flow and genesis of hydrothermal ore deposits: Economic Geology, v. 75th Anniversary, p. 424-457.

Cline, J. S., and Bodnar, R. J., 1991, Can economic porphyry copper mineralization be generated by a typical calc-alkaline melt?: Journal of Geophysical Research, v. 96, p. 8113-8126.

Cline, J. S., and Bodnar, R. J., 1994, Direct evolution of a brine from crystallizing silicic melt at the Questa, New Mexico, molybdenum deposit: Economic Geology, v. 89, p. 1780-1802.

Duan, Z., Moller, N., and Weare, J. H., 2003, Equations of state for the NaCl-H_2O-CH_4 system and the NaCl-H_2O-CO_2-CH_4 system; phase equilibria and volumetric properties above 573 K: Geochimica et Cosmochimica Acta, v. 67, p. 671-680.

Fournier, R. O., 1987, Conceptual Models of Brine Evolution in Magmatic-Hydrothermal Systems, *in* Decker, R. W., Wright, T. L., and Stauffer, P. H., eds., Volcanism in Hawaii, 2: Washington, United States Government Printing Office, p. 1487-1506.

Guilbert, J. M., and Lowell, J. D., 1974, Variations in zoning patterns in porphyry ore deposits: Canadian Mining and Metallurgical Bulletin, v. 67, p. 99-109.

Haar, L., Gallagher, J. S., and Kell, G. S., 1984, NBS/NRC Steam Tables: Thermodynamic and Transport Properties and Computer Programs for Vapor and Liquid States of Water in SI Units, Hemisphere Publishing Corporation.

Haas, J. L. J., 1976, Physical Properties of the Coexisting Phases and Thermochemical Properties of the H_2O Component in Boiling NaCl Solutions: Geological Survey Bulletin, v. 1421-A, p. 73pp.

Harris, A. C., and Golding, S. D., 2002, New evidence of magmatic-fluid-related phyllic alteration: Implications for the genesis of porphyry Cu deposits: Geology, v. 30, p. 335-338.

Hayba, D. O., and Ingebritsen, S. E., 1997, Multiphase groundwater flow near cooling plutons: Journal of Geophysical Research, v. 102, p. 12235-12252.

Hedenquist, J. W., Arribas, A., Jr., and Reynolds, T. J., 1998, Evolution of an Intrusion-Centered Hydrothermal System: Far Southeast-Lepanto Porphyry and Epithermal Cu-Au Deposits, Philippines: Economic Geology, v. 93, p. 373-404.

Hedenquist, J. W., and Richards, J. P., 1998, The influence of geochemical techniques on the development of genetic models for porphyry copper deposits, *in* Richards, J. P., and Larson, P. B., eds., Techniques in Hydrothermal Ore Deposits Geology, 10. Reviews in Economic Geology, p. 235-256.

Holland, H. D., 1972, Granites, Solutions, and Base Metal Deposits: Economic Geology, v. 67, p. 281-301.

Keevil, N. B., 1942, Vapor Pressures of Aqueous Solutions at High Temperatures: American Chemical Society Journal, v. 64, p. 841-850.

Kilinc, I. A., and Burnham, C. W., 1972, Partitioning of Chloride Between a Silicate Melt and Coexisting Aqueous Phase from 2 to 8 Kilobars: Economic Geology, v. 67, p. 231-235.

Knapp, R. B., and Norton, D., 1981, Preliminary Numerical Analysis of Processes Related to Magma Crystallization and Stress Evolution in Cooling Pluton Environments: American Journal of Science, v. 281, p. 35-68.

Kosinski, J. J., and Anderko, A., 2001, Equation of state for high-temperature aqueous electrolyte and nonelectrolyte systems.: Fluid Phase Equilibria, v. 183-184, p. 75-86.

Lowell, J. D., and Guilbert, J. M., 1970, Lateral and Vertical Alteration-Mineralization Zoning in Porphyry Ore Deposits: Economic Geology, v. 65, p. 373-408.

McInnes, B. I. A., Evans, N. J., Fu, F. Q., and Garwin, S., 2005, Application of thermochronology to hydrothermal ore deposits: Reviews in Mineralogy and Geochemistry, v. 58, p. 467-498.

National Research Council, 1928, International critical tables of numerical data, physics, chemistry, and technology: New York, McGraw-Hill, 444 p.

Norton, D., and Knight, J., 1977, Transport Phenomena in Hydrothermal Systems: Cooling Plutons: American Journal of Science, v. 277, p. 937-981.

Norton, D. L., 1982, Fluid and heat transport phenomena typical of copper-bearing pluton environments, *in* Titley, S. R., ed., Advances in Geology of the Porphyry Copper Deposits: Tucson, AZ, University of Arizona Press.

Norton, D. L., 1984, Theory of Hydrothermal Systems: Annual Reviews of Earth and Planetary Science, v. 12, p. 155-177.

Palliser, C., and McKibbin, R., 1998a, A model for deep geothermal brines; I, T-p-X state-space description: Transport in Porous Media, v. 33, p. 65-80.

Palliser, C., and McKibbin, R., 1998b, A model for deep geothermal brines; II, Thermodynamic properties, density: Transport in Porous Media, v. 33, p. 129-154.

Pitzer, K. S., and Pabalan, R. T., 1986, Thermodynamics of NaCl in steam: Geochimica et Cosmochimica Acta, v. 50, p. 1445-1454.

Potter, R. W. I., 1977, Pressure Corrections for Fluid Inclusion Homogenization Temperatures Based on the Volumetric Properties of the System NaCl-H_2O: Journal Research U.S. Geological Survey, v. 5, p. 603-607.

R Development Core Team, 2007, R: A language and environment for statistical computing: Vienna, Austria, R Foundation for Statistical Computing.

Roedder, E., 1984, Fluid Inclusions, *in* Ribbe, P. H., ed., Reviews in Mineralogy, 12: Washington, D.C., Mineralogical Society of America, p. 644.

Rusk, B. G., Reed, M. H., Dilles, J. H., Klemm, L. M., and Heinrich, C. A., 2004, Compositions of magmatic hydrothermal fluids determined by LA-ICP-MS of fluid inclusions from the porphyry copper-molybdenum deposit at Butte, MT: Chemical Geology, v. 210, p. 173-199.

Sheppard, S. M. F., Nielsen, R. L., and Taylor, H. P., Jr., 1971, Hydrogen and Oxygen Isotope Ratios in Minerals from Porphyry Copper Deposits: Economic Geology, v. 66, p. 515-542.

Shinohara, H., and Hedenquist, J. W., 1997, Constraints on Magma Degassing beneath the Far Southeast Porphyry Cu-Au Deposit, Philippines: Journal of Petrology, v. 38, p. 1741-1752.

Shinohara, H., Iiyama, J. T., and Matsuo, S., 1989, Partition of chlorine compounds between silicate melt and hydrothermal solutions; I, Partition of NaCl-KCl: Geochimica et Cosmochimica Acta, v. 53, p. 2617-2630.

Sillitoe, R. H., 1972, A Plate Tectonic Model for the Origin of Porphyry Copper Deposits: Economic Geology, v. 67, p. 184-197.

Sillitoe, R. H., 1973, The tops and bottoms of porphyry copper deposits: Economic Geology, v. 80, p. 1467-1514.

Sourirajan, S., and Kennedy, G. C., 1962, The system H_2O-NaCl at elevated temperatures and pressures: American Journal of Science, v. 260, p. 115-141.

Sterner, S. M., Hall, D. L., and Bodnar, R. J., 1988, Synthetic fluid inclusions. V. Solubility relations in the system NaCl-KCl-H_2O under vapor-saturated conditions: Geochimica et Cosmochimica Acta, v. 52, p. 989-1006.

Taylor, H. P., Jr., 1974, The application of oxygen and hydrogen isotope studies to problems of hydrothermal alteration and ore deposition: Economic Geology, v. 69, p. 843-883.

Taylor, H. P., Jr., 1997, Oxygen and hydrogen isotope relationships in hydrothermal mineral deposits, *in* Barnes, H. L., ed., Geochemistry of hydrothermal ore deposits: New York, John Wiley, p. 229-302.

Figures

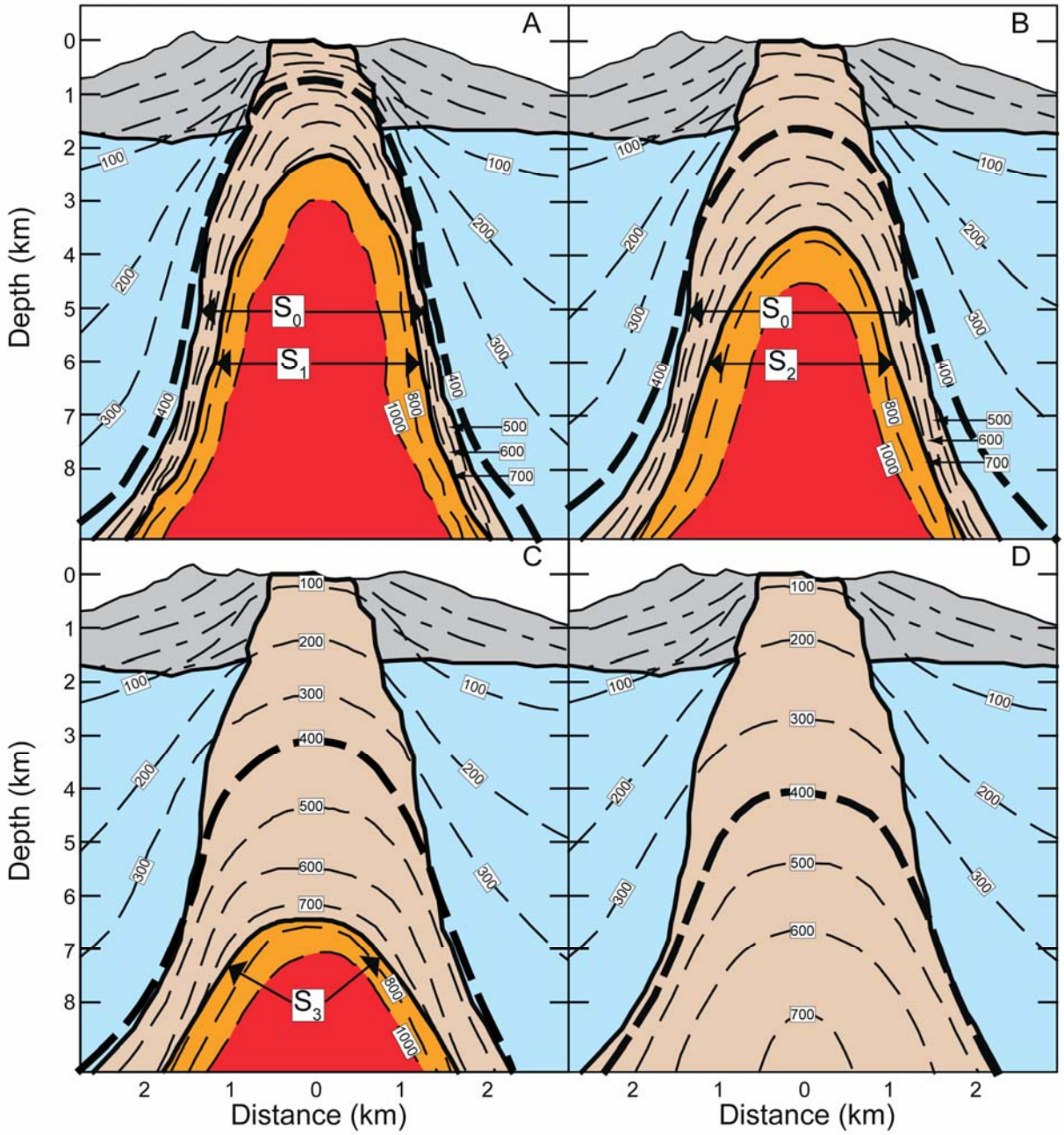

Figure 1: Geologic model of four consecutive times during the evolution of a porphyry intrusion, modified after Burnham (1979). The red shaded areas represent melt, the orange represent the water-saturated carapace in which crystals, melt, and aqueous fluid coexist, the tan represent the crystallized margin of the intrusion, the blue represent the country rocks, and the grey represent the volcanic pile associated with the intrusive system. Isotherms are estimated from Knapp and Norton (1981) (see Fig. 2). The original extent of the intrusion is

designated by the S_0 boundary. The water-saturated solidus is identified on subsequent diagrams by the designations of S_1-S_3.

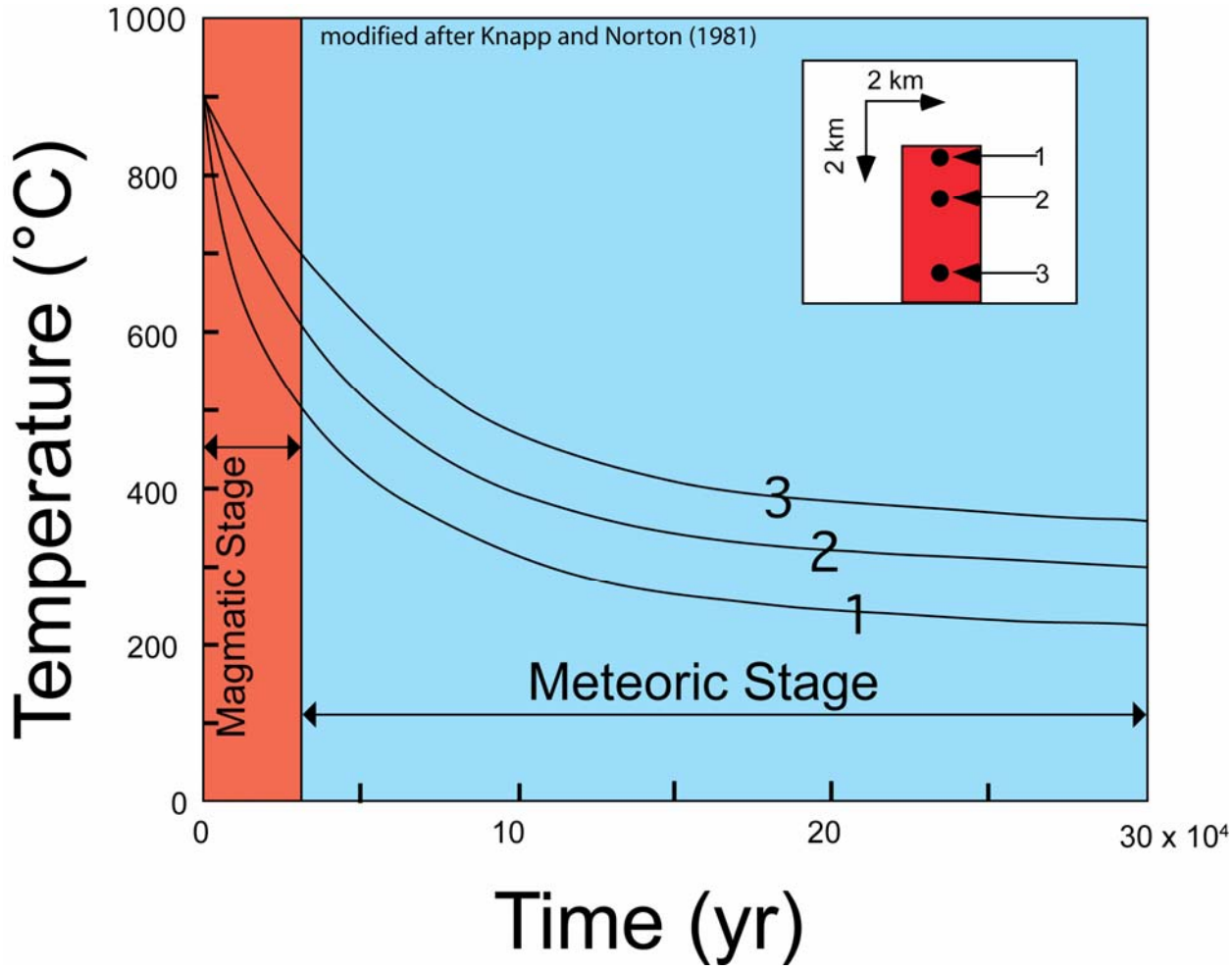

Figure 2: Thermal evolution of three points within an epizonal intrusion, modified after Knapp and Norton (1981). The light-red shaded region labeled magmatic stage represents the length of time between the initial intrusion up through complete crystallization. The light-blue shaded region represents the post-magmatic stage of the system dominated by an influx of meteoric water. Porphyry copper mineralization is closely associated with the magmatic stage of the system, and therefore the model presented below only spans the length of time defined by the red-shaded region.

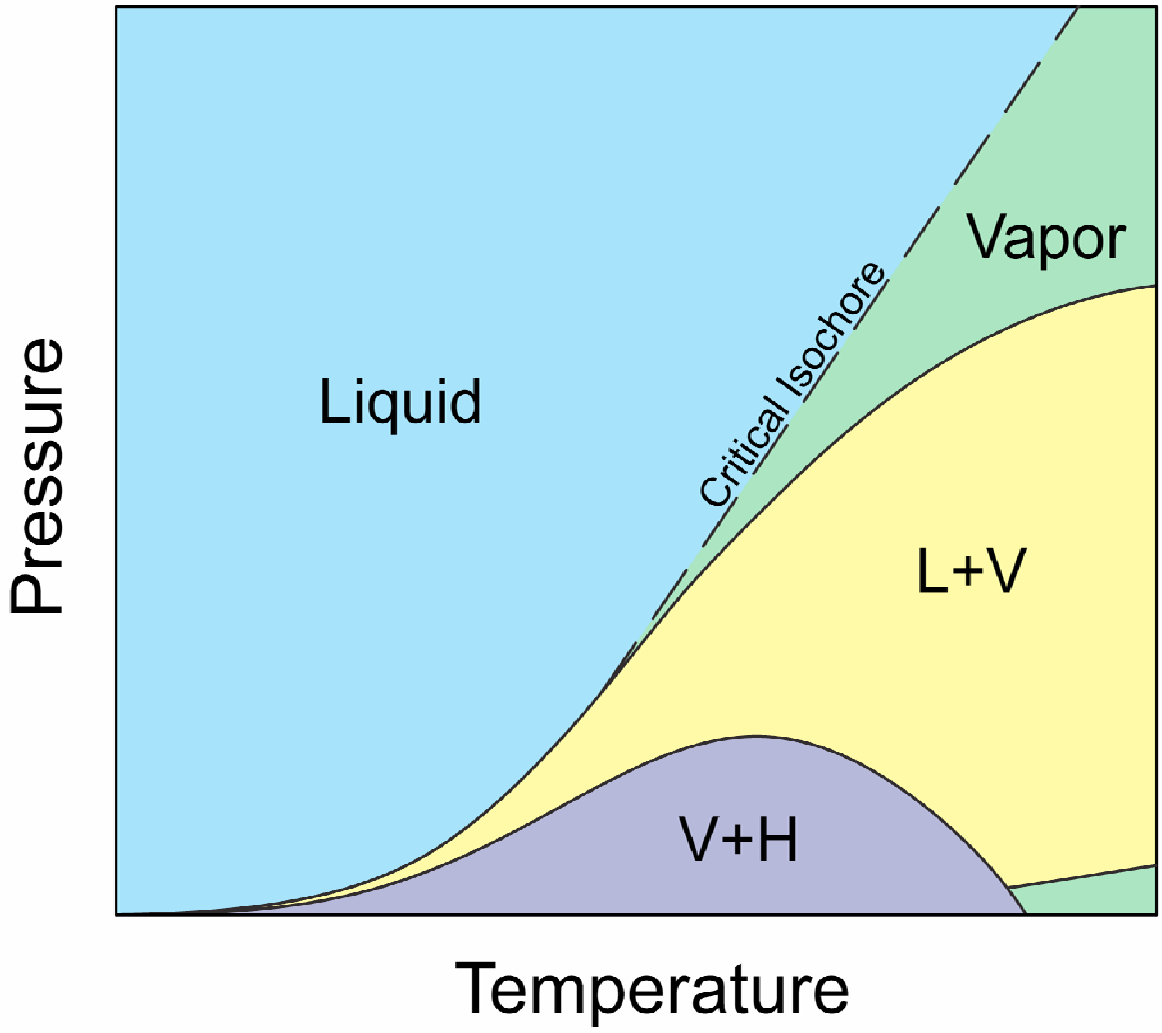

Figure 3: Schematic pressure-temperature phase diagram of the H_2O-NaCl system. The single-phase region includes both the blue and green shaded fields, and is separated into the liquid and vapor stable regions by the critical isochore. The two-phase liquid+vapor (L+V) stable field includes the yellow shaded area, and the two-phase vapor+halite (V+H) stable field includes the purple shaded area. A single phase fluid that enters the L+V field will either condense (if vapor) or boil (if liquid) to produce a high salinity liquid phase and a low salinity vapor phase. Any fluid that enters the V+H stable field will separate into a very low salinity vapor and halite crystals.

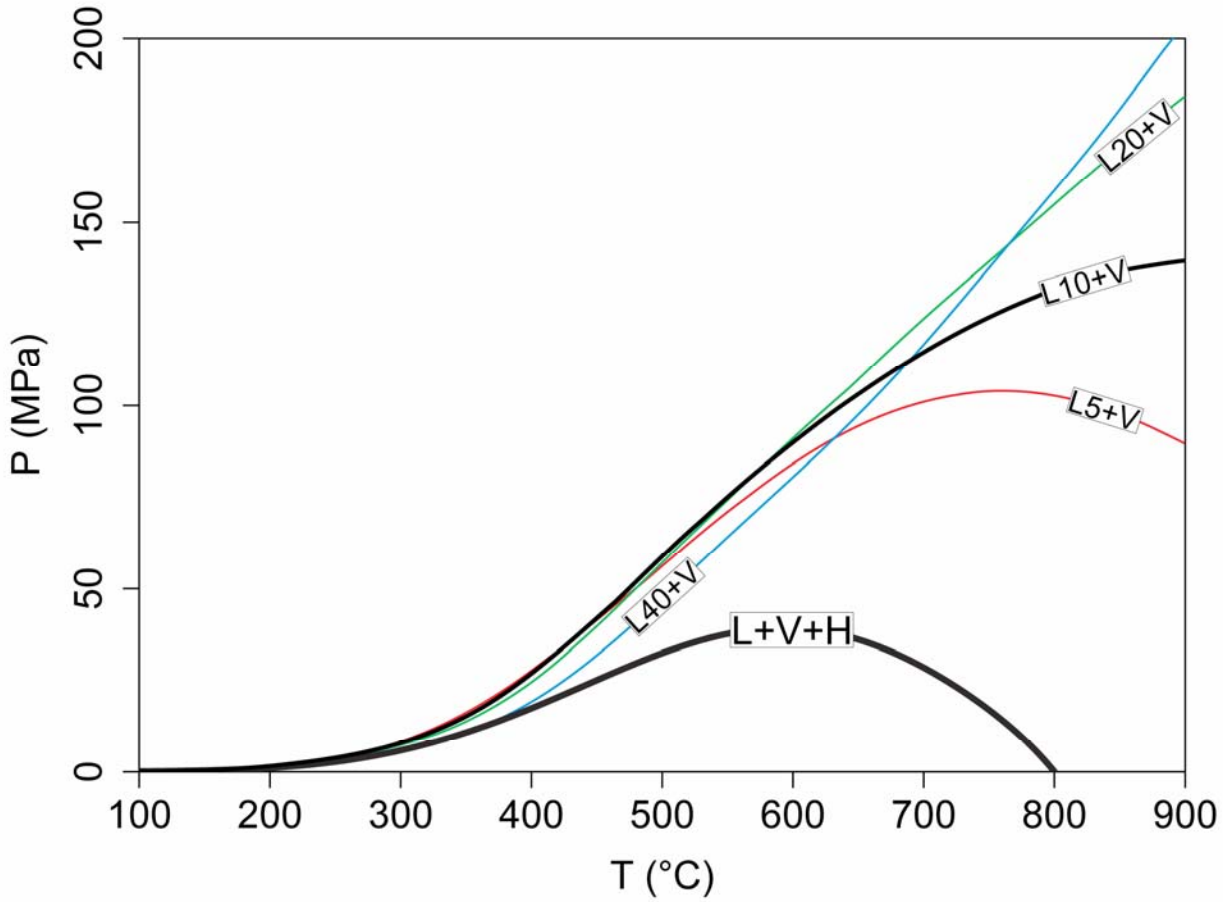

Figure 4: Pressure-temperature phase diagram of the H_2O-NaCl system for compositions of 5, 10, 20, and 40 wt. % NaCl. The three-phase (L+V+H) curve is drawn for reference. For temperatures below 600°C, the liquid-vapor curves for these compositions occupy similar paths through P-T space. This means that once a system enters the two-phase field at higher temperature and pressure, the system will remain in the two-phase field independent of changing liquid to vapor ratios. This allows for the usage of a reasonable intermediate composition of 10 wt. % NaCl to model the salinity of an average magmatic aqueous phase that is relevant to a wide range of porphyry environments.

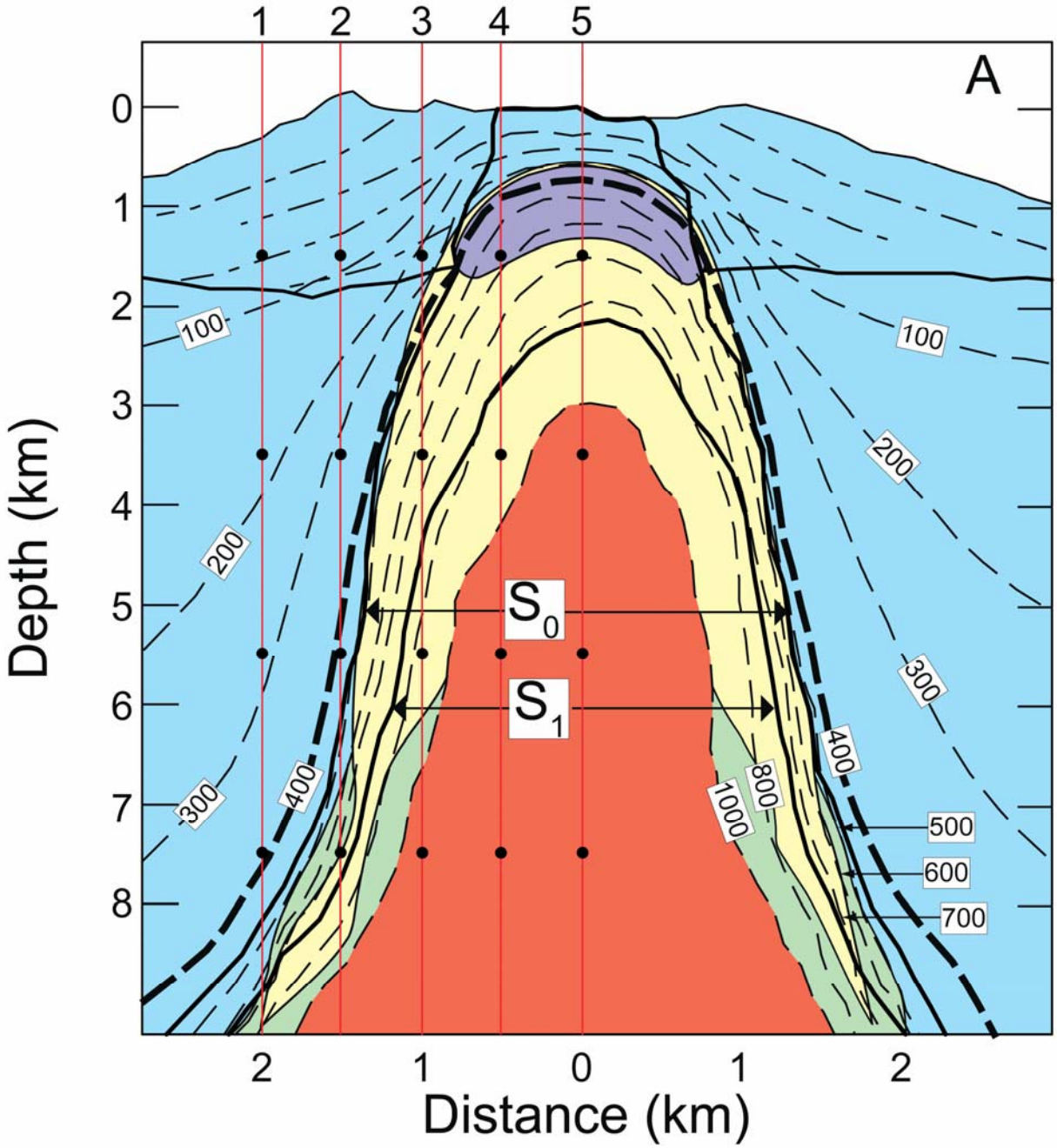

Figure 5: Porphyry model "A" represents the earliest point in time during the crystallization of a hydrous porphyry intrusion when the melt reaches water saturation and exsolves an aqueous phase (see Fig. 1a). The phase stability fields are color-coded to match those of the schematic phase diagram (Fig. 4). Five red lines (numbered 1 through 5) are superimposed on the diagram, and are the basis for constructing P-T paths and fluid inclusion charts below. The system is capped by a somewhat large area of V+H stability, which is important in generating a zone of acid alteration (see discussion) (Fournier, 1987). Most of the area above the crystallizing pluton is dominated by L+V stability, where high salinity brines coexist with low salinity vapors. A single phase magmatic vapor is stable deep along the flanks of the system.

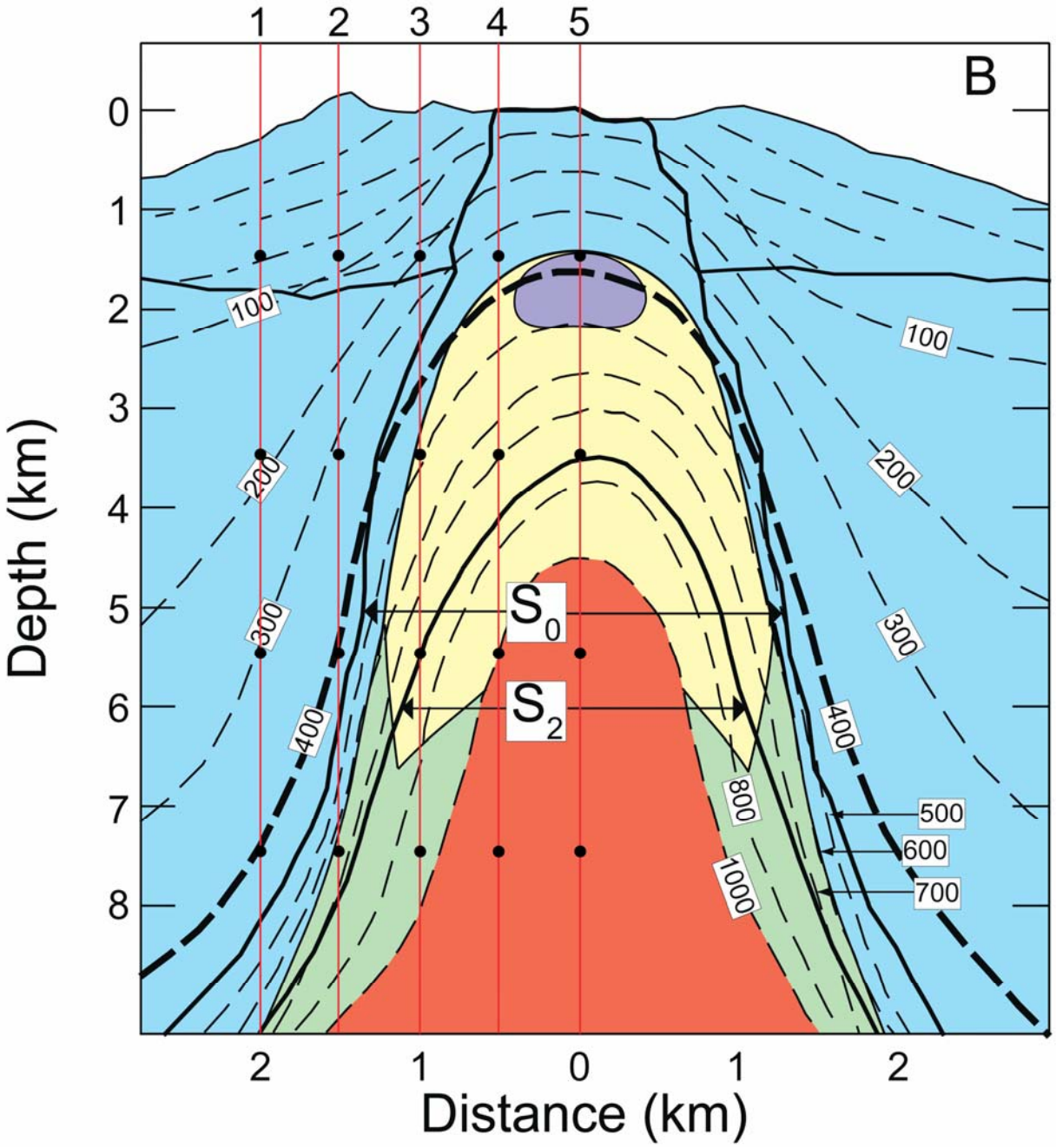

Figure 6: Porphyry model "B" represents a point in time during the crystallization of a hydrous porphyry intrusion when crystallization has proceeded to a minimum depth of approximately 4 km. Colors and lines are superimposed according to the same criteria as Figure 5. Here, the V+H stability field has shrunk considerably, and the single-phase magmatic vapor on the flanks of the system is more prevalent.

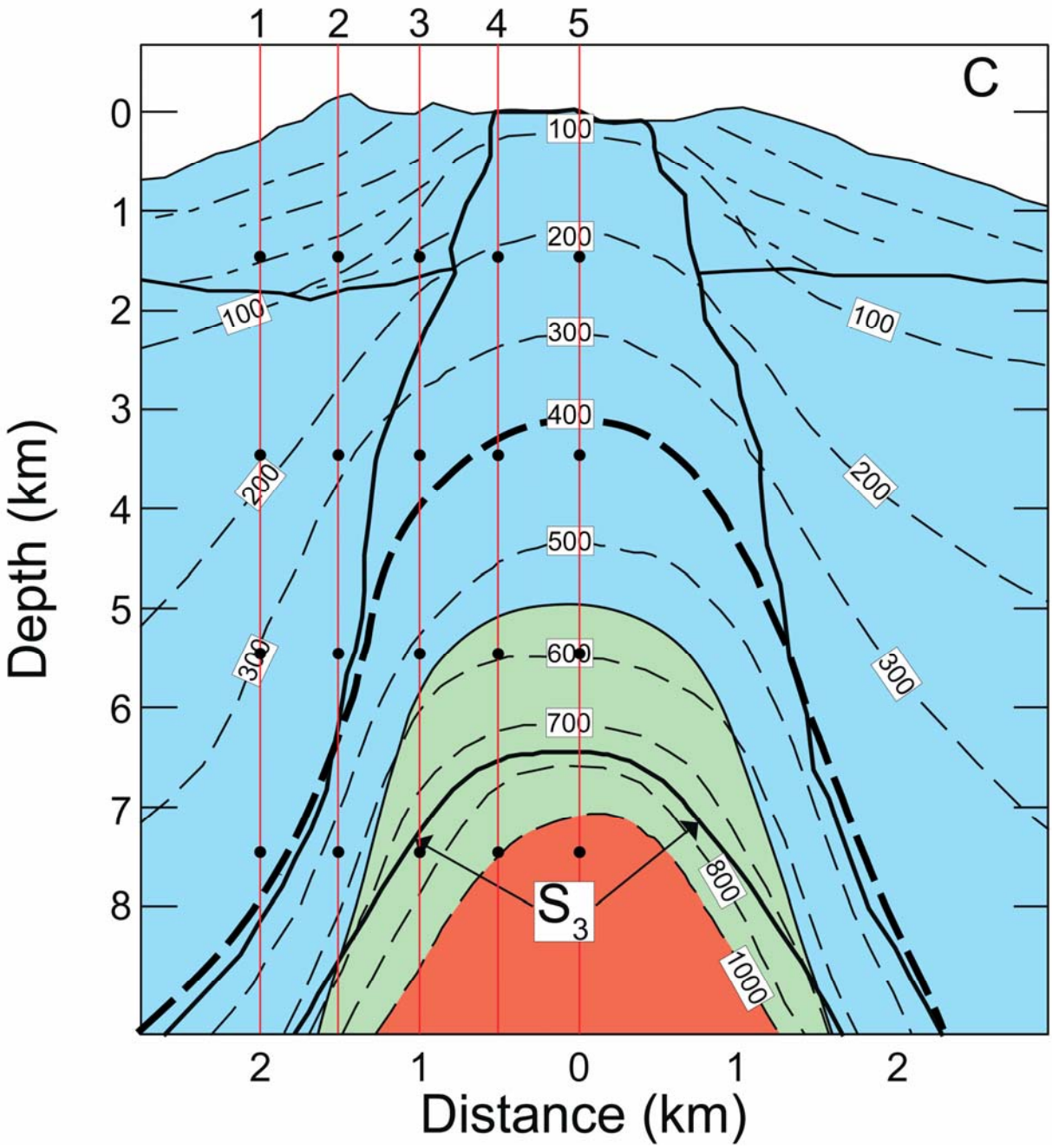

Figure 7: Porphyry model "C" represents a point in time during the crystallization of a hydrous porphyry intrusion when crystallization has proceeded to a minimum depth of approximately 7 km. Colors and lines are superimposed according to the same criteria as Figure 5. Here, the V+H and L+V fields have entirely disappeared as magmatic fluid ascends along a P-T path that does not intersect the two-phase L+V field. Above the brittle-ductile transition (i.e. above the 400°C isotherm), meteoric water has likely entered the system, but stays separate from the deeper magmatic fluid in the ductile regime.

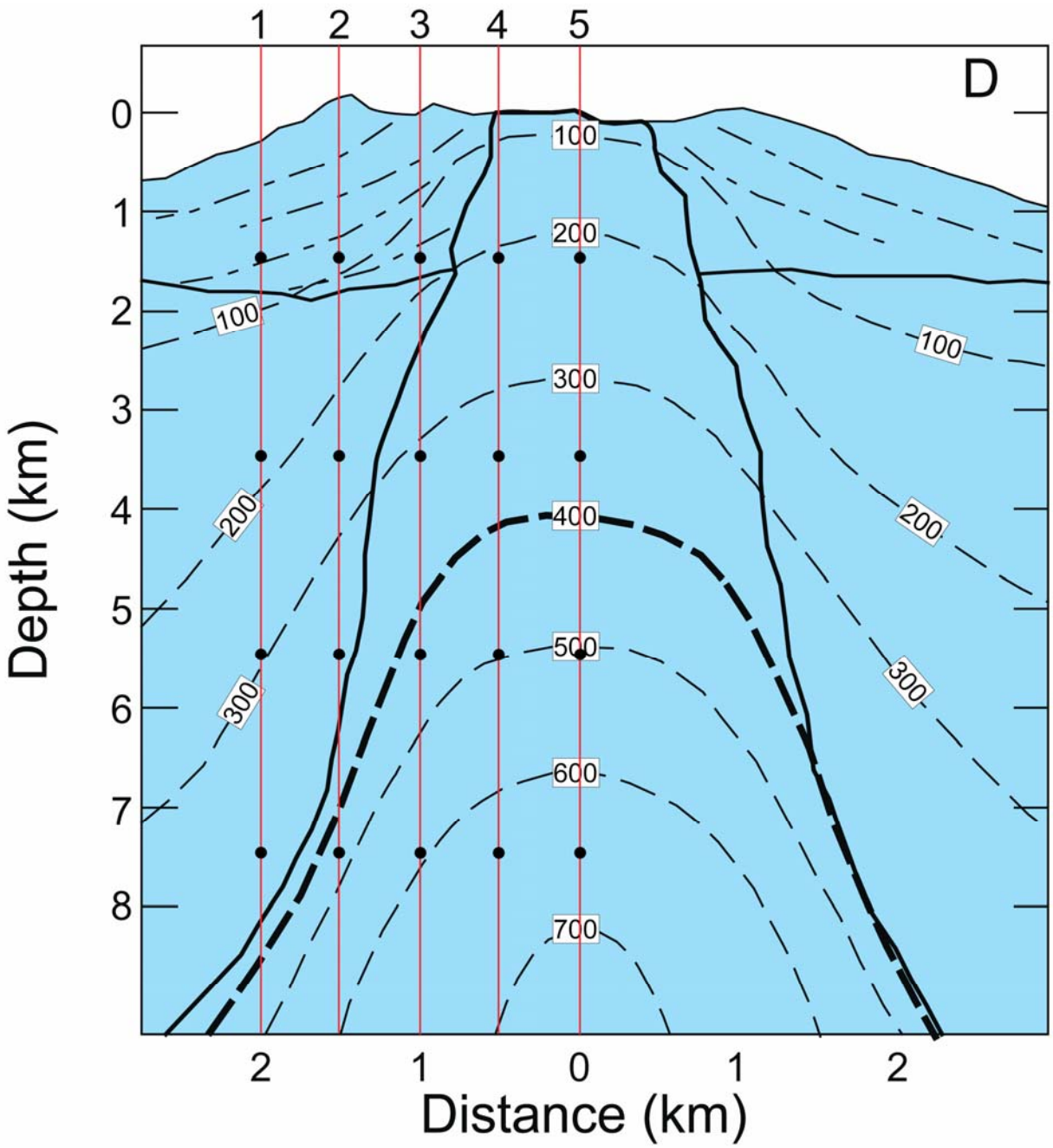

Figure 8: Porphyry model "D" represents a point in time during the crystallization of a hydrous porphyry intrusion when the entire pluton has crystallized, but the remnant thermal anomaly is still significant. At this point, the entire system is in the one-phase liquid stable field, and the source of fluids from here on will be dominantly meteoric.

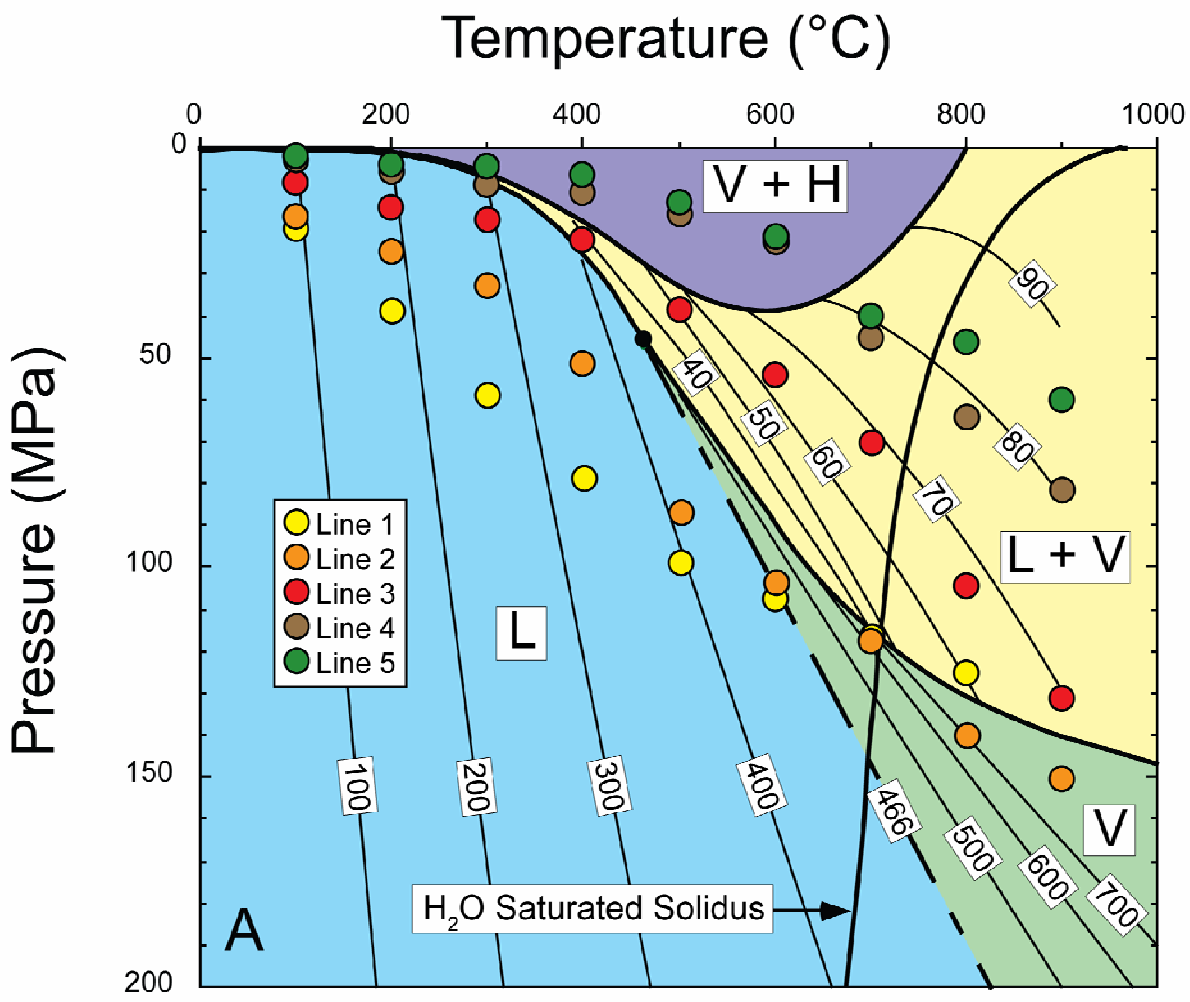

Figure 9: P-T phase diagram of the H_2O-NaCl system for a composition of 10 wt. % NaCl. P-T paths for the intersection of isotherms with lines 1-5 of "model A" (Fig. 5) have been plotted. These show that towards the center of the intrusion, magmatic fluids traverse directly from the two-phase L+V field to the two-phase V+H field. Towards the flanks of the system, magmatic fluids may enter and/or exit the vapor and L+V stable fields as they ascend.

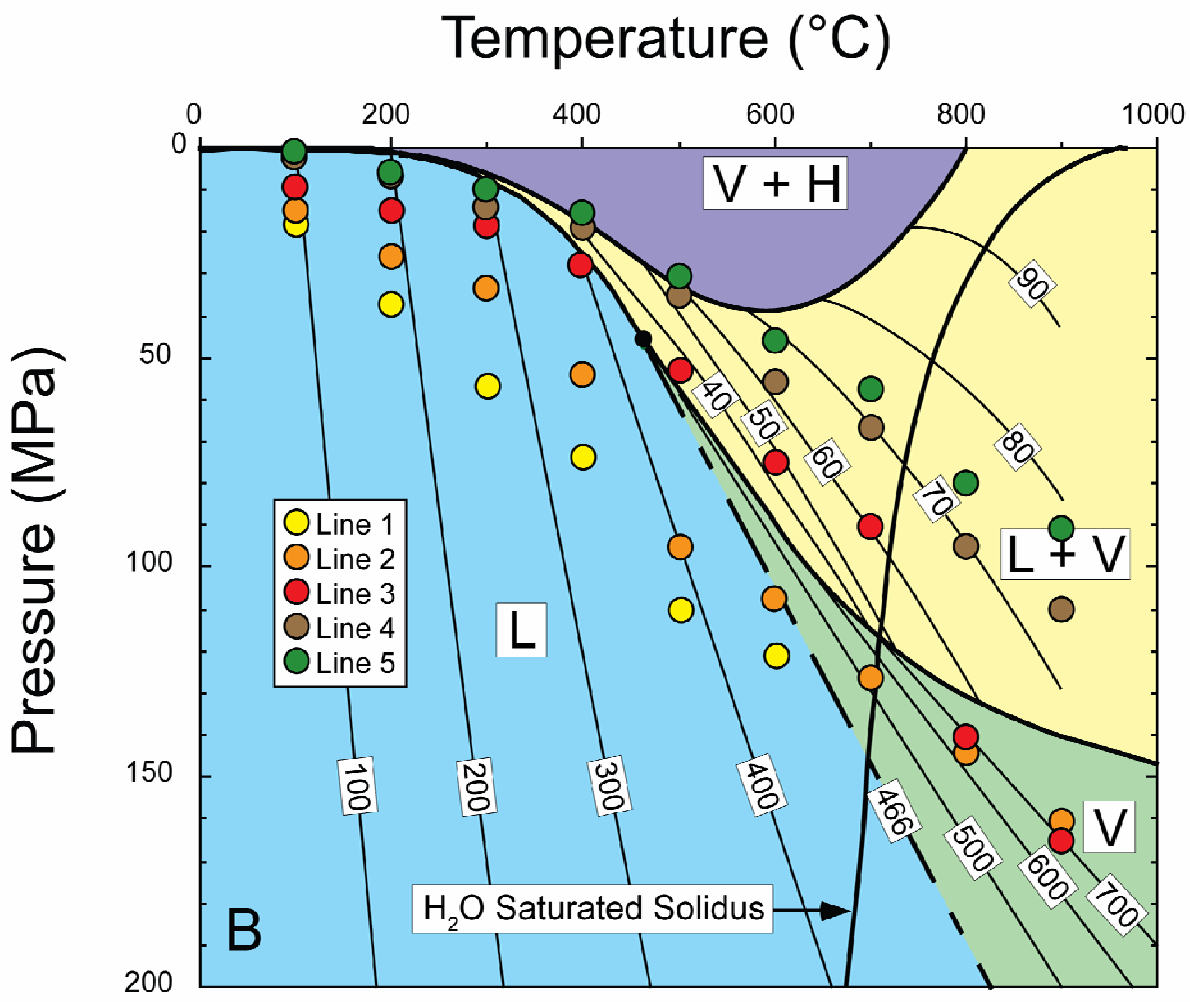

Figure 10: P-T phase diagram of the H_2O-NaCl system for a composition of 10 wt. % NaCl. P-T paths for the intersection of isotherms with lines 1-5 of "model B" (Fig. 6) have been plotted. As the crystallized margin of the pluton retreats downwards, the P-T paths begin to take a more direct path out of the L+V field, mostly bypassing the V+H field. Towards the flanks of the system, magmatic fluids lie exclusively in the single-phase vapor stable field.

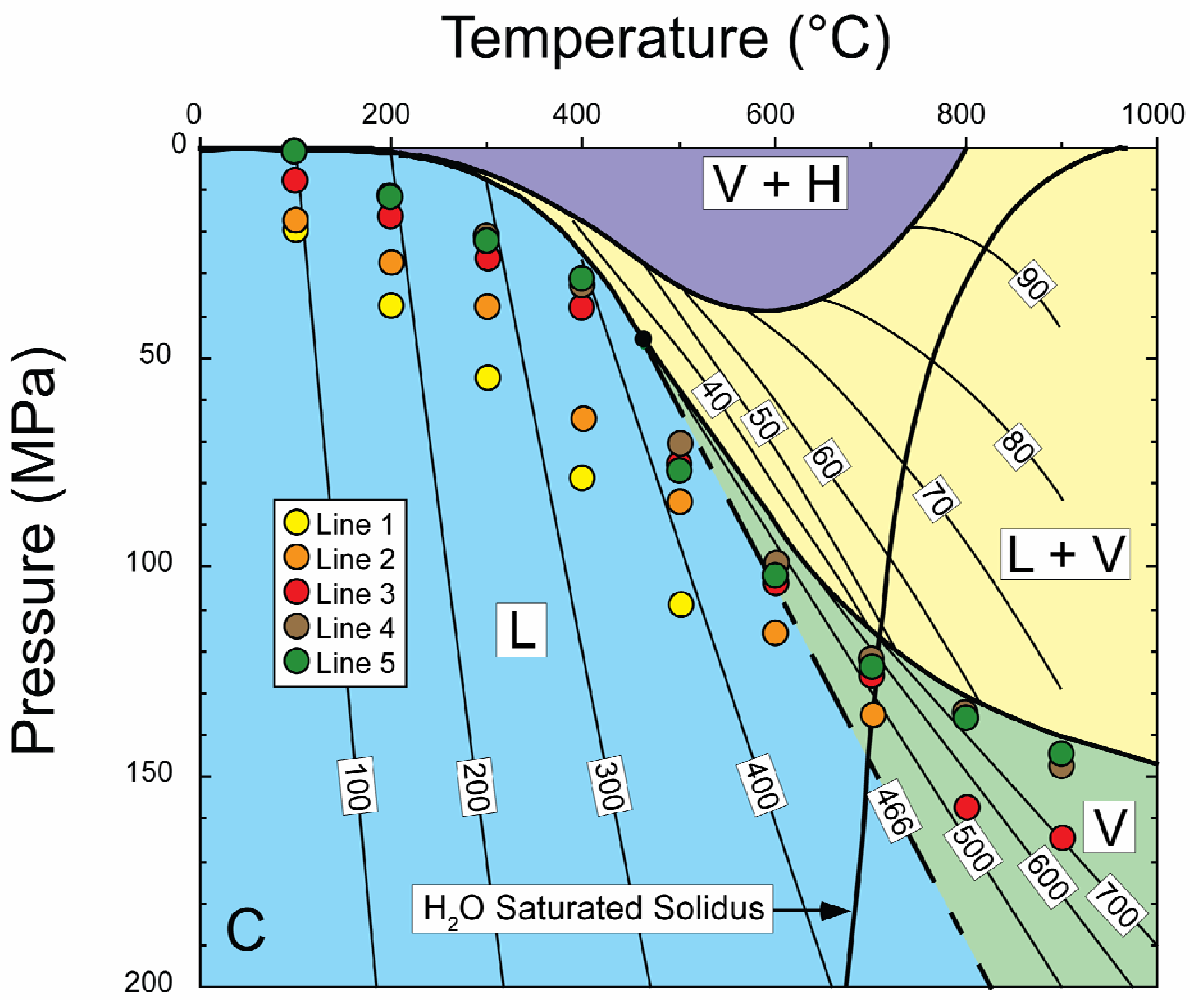

Figure 11: P-T phase diagram of the H_2O-NaCl system for a composition of 10 wt. % NaCl. P-T paths for the intersection of isotherms with lines 1-5 of "model C" (Fig. 7) have been plotted. At this time the crystallized margin of the pluton has retreated to a depth such that the P-T paths do not intersect the two-phase L+V field during ascent. Thus, the entire system remains in the one-phase field, with fluids that may have a vapor-like, liquid-like, or critical density. This has implications for later phyllic alteration by moderate to low salinity fluids having a magmatic isotopic composition (see discussion).

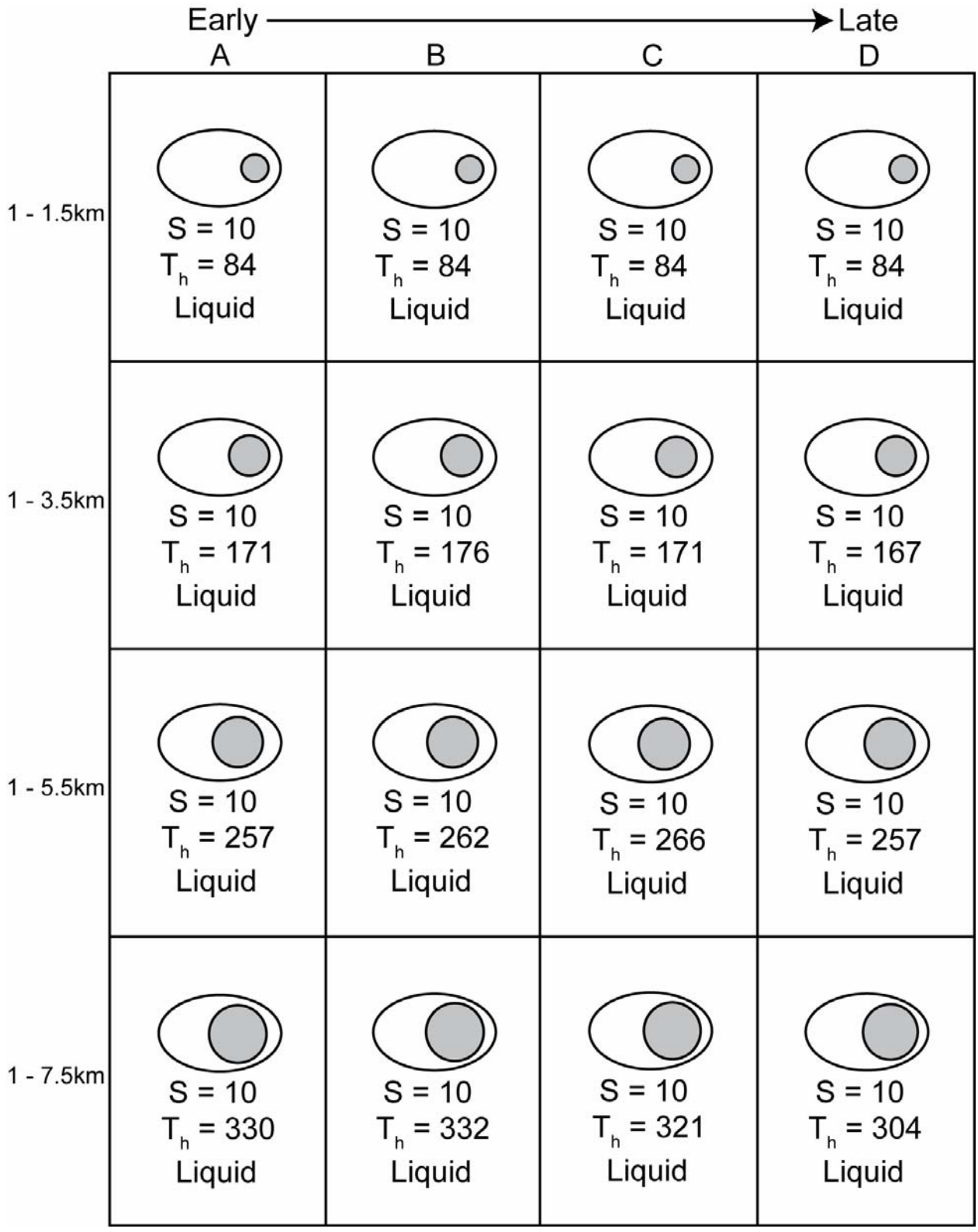

Figure 12: Chart displaying the temporal evolution of fluid inclusions at points from 1.5 to 7.5 km along "line 1" (see Figs. 5-8).

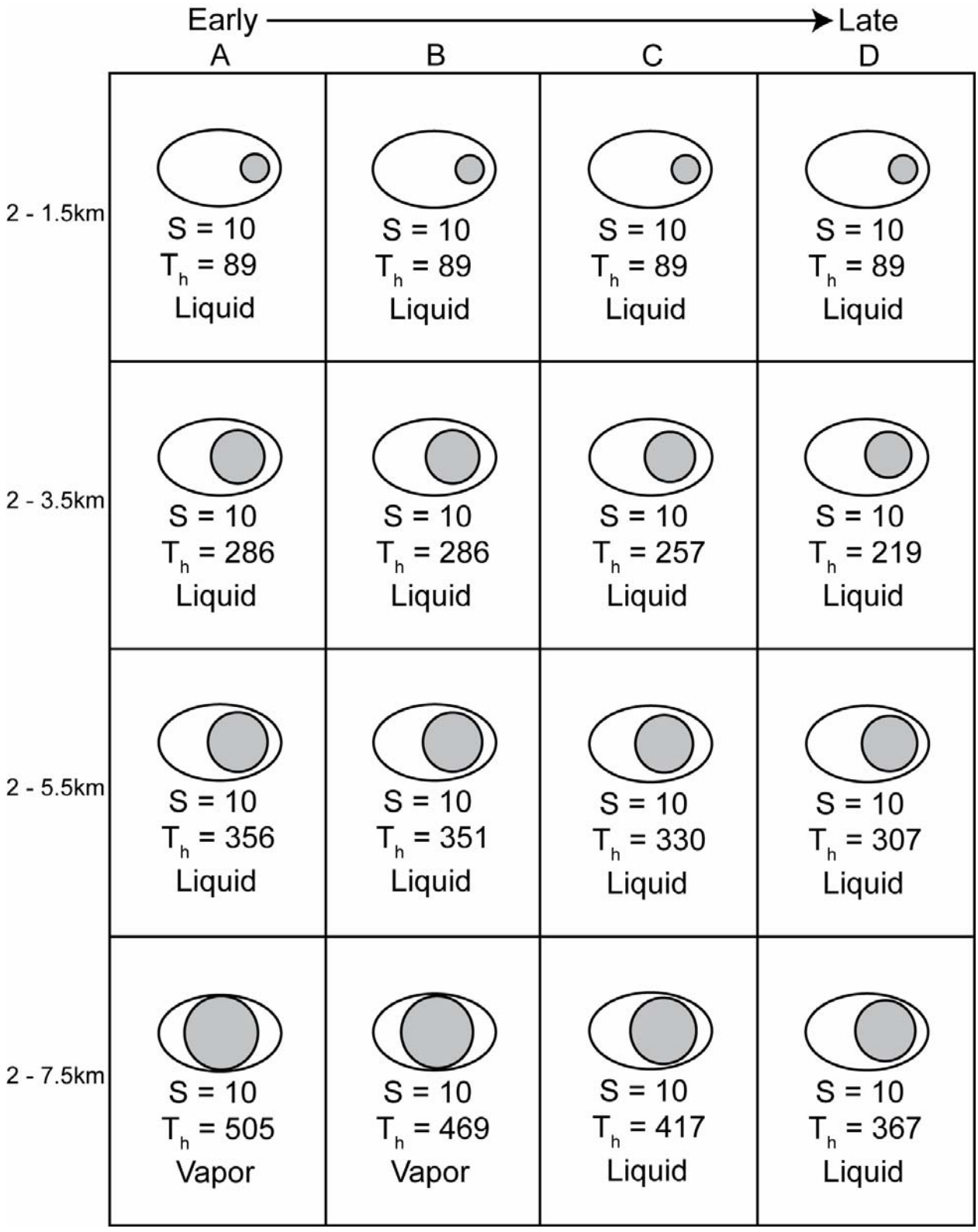

Figure 13: Chart displaying the temporal evolution of fluid inclusions at points from 1.5 to 7.5 km along "line 2" (see Figs. 5-8).

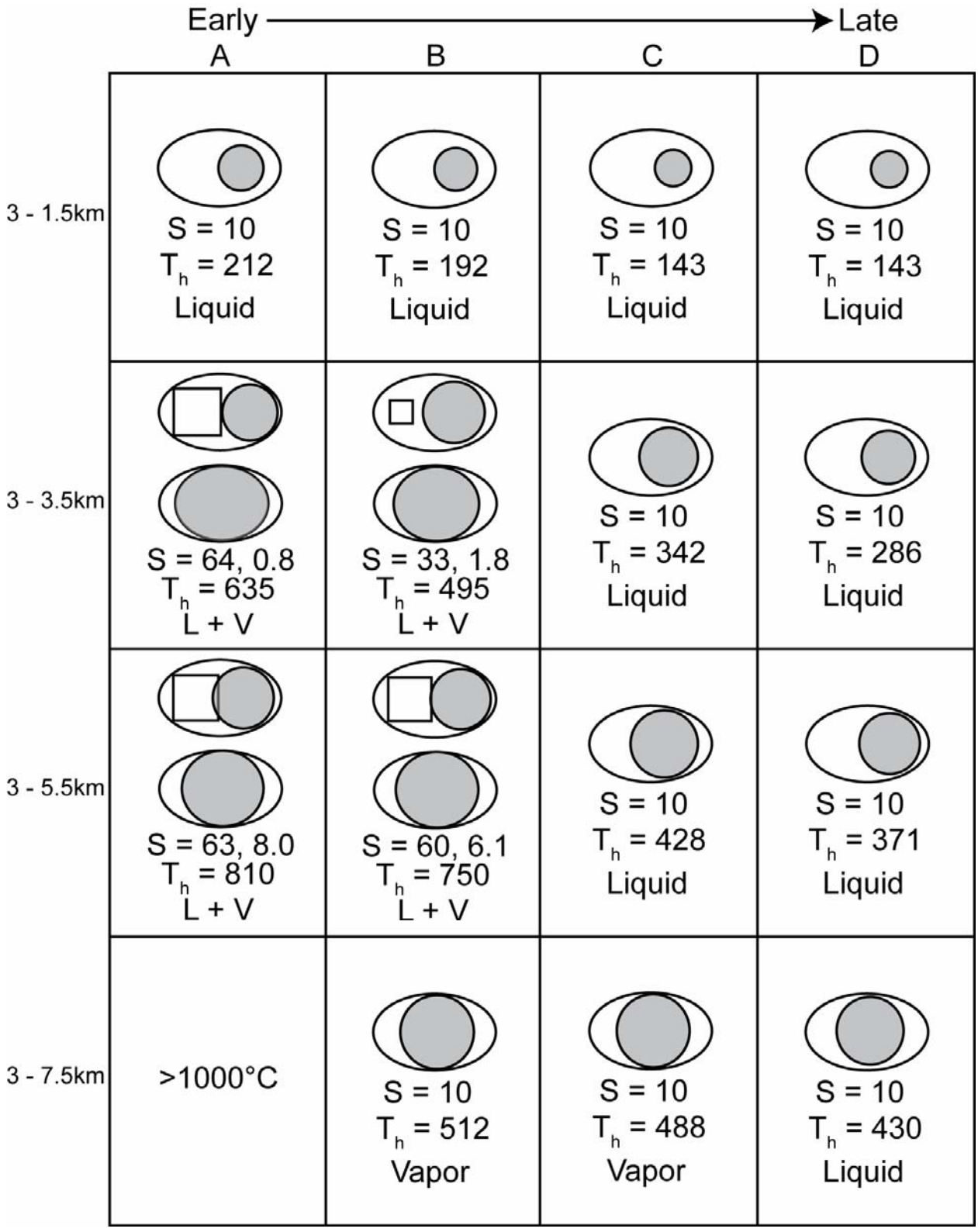

Figure 14: Chart displaying the temporal evolution of fluid inclusions at points from 1.5 to 7.5 km along "line 3" (see Figs. 5-8).

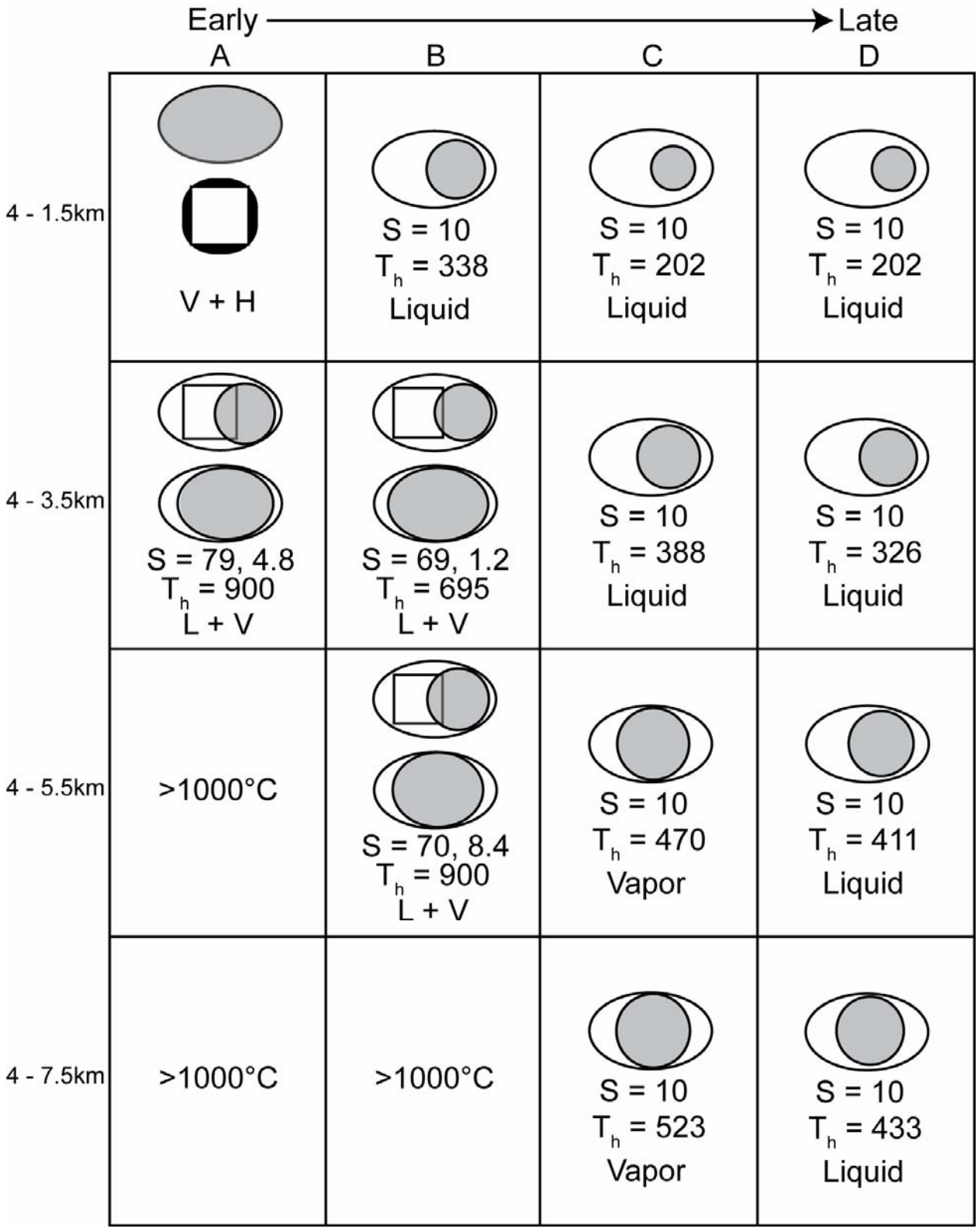

Figure 15: Chart displaying the temporal evolution of fluid inclusions at points from 1.5 to 7.5 km along "line 4" (see Figs. 5-8).

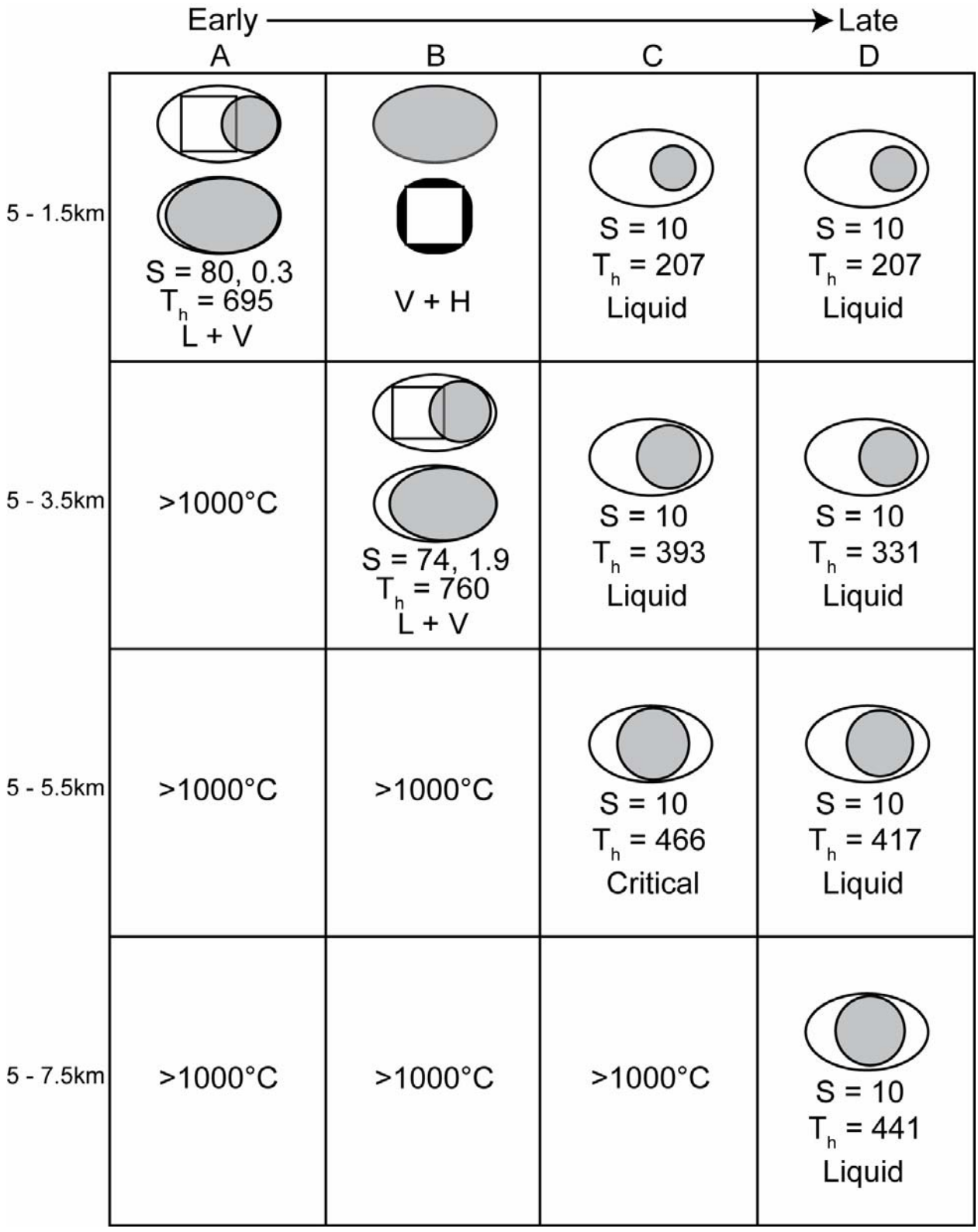

Figure 16: Chart displaying the temporal evolution of fluid inclusions at points from 1.5 to 7.5 km along "line 5" (see Figs. 5-8).

Appendix A: Published microthermometric data for fluid inclusions that homogenize by halite disappearance

The following table summarizes published studies from 1970 - 2007 that have reported microthermometry data for fluid inclusions that homogenize by halite disappearance ("Type C" inclusions, Figure 1 from the main text). The first column refers to the literature sources that are listed immediately below the table. The second column lists the geologic environment and/or deposit type that most closely matches the description given by the authors of the paper. The following abbreviations are used when appropriate: PCD = Porphyry Copper Deposit; IOCG = Iron Oxide/Copper/Gold; MVT = Mississippi Valley Type; BX = Breccia; PGE = Platinum Group Element; REE = Rare Earth Element; SEDEX = SEDimentary EXhalitive; FI = Fluid Inclusions. The third and fourth columns list ranges in Th_{L-V} and Tm_{halite} (°C), respectively. The fifth column lists the range of salinities reported, in equivalent weight percent NaCl. The sixth column lists pressures (in megapascals) reported in the publication that were determined from "Type C" inclusions, and the seventh column lists depths (in kilometers) estimated by the authors of the original publication based on pressures reported in column 6.

In general, recent publications are more abundant and report data on "Type C" inclusions in greater detail. Older publications often provide insufficient detail to identify inclusions that homogenize by halite disappearance, and generally require closer inspection to retrieve the relevant data. The higher quality of more recent data is likely due to advances in instrumentation, including the introduction of the USGS gas-flow stage in 1979 (Werre et al., 1979), and related improvements in fluid inclusion microthermometric methods and data analysis. Data in the table are listed chronologically, starting with the most recent publications on top.

This table is not intended to be a comprehensive list of all published data for inclusions that homogenize by halite disappearance. Rather it represents a list that may be a useful starting point for future researchers who encounter "Type C" fluid inclusions in their studies and wish to review the available literature. Only publications in which the investigators clearly describe inclusions that homogenize by halite disappearance or show Th_{L-V} versus Tm_{halite} and/or salinity versus homogenization temperature plots in which it is obvious that some inclusions homogenized by halite disappearance are included. Many additional publications were reviewed that described inclusions that could have been "Type C" inclusions. However, these were not included because insufficient detail was provided to be certain that the inclusions did homogenize by halite disappearance. The manner in which microthermometric data were presented ranged from tables listing data for individual inclusions, to statements of the ranges of Th_{L-V} and Tm_{halite}, to graphs showing Th_{L-V} versus Tm_{halite} and/or salinity versus homogenization temperature, to ambiguous histograms that do not necessarily indicate $Th_{L-V} < Tm_{halite}$, but with accompanying text indicating that "Type C" inclusions were observed. In those cases in which ambiguity occurs, data were not included in the table and missing data are marked with a "—" symbol. Question marks are used in cases where ranges

of data given the description in the text are questionable. Tilde (~) characters precede values that could only be approximated through visual inspection of graphical presentations of data.

References

Werre RW, Jr., Bodnar RJ, Bethke PM & Barton PB, Jr. (1979) A novel gas-flow fluid inclusion heating/freezing stage. GSA Abstracts, 11, 539.

Summary of Reported Data in Selected Publications

Reference	Geologic Environment	Th_{L-V} (°C)	Tm_{halite} (°C)	Salinity (wt. %)	Pressure (MPa)	Depth (km)
1.	IOCG	109-266	198-447	32-56	~20-250	—
2.	MVT	141-300	up to +100	—	—	—
3.	Alkaline Massif	250-315	264-325	35.5-39.8	—	—
4.	Vein	150-370	240-380	31-44	40-90	—
5.	PCD	~200-500	~275-575	36.9-65.8	>90	—
6.	Orogenic Au	161-307	198-396	31.8-46.2	—	—
7.	Veins	145-220	270-300	36-38	50-300	—
8.	PCD/Epithermal	~200-420	—	~36-46	—	—
9.	Intrusion Au	125-360	150-480	30-57	130	—
10.	IOCG	80-200	100-500	26-65	—	—
11.	PCD	291-400	421-520	49.4-60.1	~45-50	—
12.	PCD	~250-~500	321-510	33-61	—	—
13.	PCD	~190-~350	~210-~425	~30-50	60-225	—
14.	Massive Sulfide	—	~180?	30	—	—
15.	Lode Au	96-322	91-386	~29-~44	93-256	—
16.	PCD	124-449	215-530	33-64	50-200	~2
17.	PCD	267-389	310-397	38.9-47.3	60	—
18.	PGE	117-325	145-315	29.5-39.3	110-150	—
19.	PCD	~200-~600	~220-~560	33-69	—	—
20.	Unconformity U	68-188	~140-~180	—	70	4-5
21.	PCD	165-600	340->600	56±5 (avg±1□)	—	—
22.	BX Pipe	217-385	251-411	35-49	50-170	—
23.	PCD	—	320-350	~40	—	—
24.	Unconformity U	109-261	136->409	29.1->43.3	—	—
25.	PCD	~160-~500	~200-~550	29.4-55.1	80-350	5-10
26.	Intrusion Au	265-365	275-390	36-46	—	—
27.	Skarn	206-530	200->600	up to 63	—	—
28.	PCD	~100-~400	200-580	~32-~66	143-247	5.3-9

29.	Vein/Skarn	206-259	—	46.1-54.0	>300	—
30.	PCD	54-530	150-600	26-90	340	13.6
31.	PCD	101-228	140-373	29-44	—	—
32.	PCD	86-475	127-520	28.8-62	30-750	—
33.	BX Pipe	213-257	250-503	34.6-56.7	>100	—
34.	PCD	175-289	222-412	~40	—	—
35.	Lode Au	90-140	182-204	~29-~38	250?	—
36.	Lode Au	172-226	332-343	—	—	—
37.	PCD	—	up to 600?	up to 74?	—	—
38.	Veins	108-278	158-322	30-37	~100-~170	>4
39.	Skarn	220-400	238-438	34-53	60-95	—
40.	PCD	~200-~480	~275-~600	~35-~70	113-280	—
41.	PCD	—	—	31-35	—	—
42.	IOCG	—	168-270	31-36	60-150	—
43.	PCD	171-456	175-467	28.5-55.4	>50	—
44.	Greenstone Au	86-147	126-326	28.7-40.2	335-525	—
45.	Greenstone Au	75-149	165-320	25.0-26.5	100-700?	—
46.	PCD	—	~220-~360	~40-~55	—	—
47.	Lode Sn	~230-~460	~295-~520	~37-~63	50-200	—
48.	PCD	<522	~522	~63	—	—
49.	PCD	~200-~500	262-520	30-~62	—	—
50.	PCD	~110-~340	~230-~570	~33-~70	100-600	—
51.	PCD	—	343-468	41.7-56.3	—	—
52.	PCD/Epithermal	—	—	—	—	—
53.	PGE	65-263	~140-509	~24-61	110-160	4-6
54.	Oceanic Crust	—	255-418	32-47	—	—
55.	REE/Vein	—	340->600	52-83	225	—
56.	PCD	176-~525	~400-~600	~44-~82	—	—
57.	Vein Au	150-300	180-320	—	—	—
58.	IOCG	—	137->430?	29-68?	—	—
59.	Intrusion Au	122.5-181.5	217-289	30-37	130	4-6

60.	Skarn	—	264-287	31-36	—	—
61.	IOCG/REE	~225-~275	—	~33-~42	—	—
62.	PCD	—	380-550	45-60	~60-280	up to 10
63.	IOCG	83-132	209-495	33-50	250	—
64.	Veins	—	151-323	30-39.5	—	—
65.	Skarn/PCD	237-340	355-400	42-56	17-50	—
66.	Epithermal	~270-~425	~325-~480	~40-~51	—	—
67.	Epithermal	—	640	79.7	400	—
68.	PGE	~87-~275	~100-~370	up to 49.4	~20-~230	—
69.	Lode Au	—	~125-~400	~27-~50	—	—
70.	Shear Zone/Vein	170-200	<200	~30	—	—
71.	SEDEX	up to 270	up to 386	~30-~45	110	—
72.	Massive Sulfide	100-193	385-510	—	—	—
73.	Vein/PCD	~60-~170	130-240	36-48	—	—
74.	PCD	215-451	~250-~490	~35-~54	80	—
75.	Greisen	160-325	215-390	32.7-38.9	—	—
76.	Lode/Vein Au	100-125	128-138	28.9-29.2	—	—
77.	IOCG/REE	100-489?	100-489?	34.7-59.8	—	—
78.	Lode/Vein Au	~75-~175	~115-~210	—	—	—
79.	IOCG	178-405	192-430	35-68	several tens	1.2-1.7
80.	Lode/Vein	90-300	100-550	37-68	100	—
81.	Vein	—	159-311	35.6-39.6	—	—
82.	PGE	130-200	280-300	29-37	200	—
83.	Skarn	—	320-485?	38-65	—	—
84.	Ophiolite	~110-~260	~115-~300	~27-40	—	—
85.	PCD	234-392	308-491	39-59	140	5
86.	PCD	309.6-315.8	>500	>65	—	—
87.	Granite Intrusion	—	300-550	40-80	40-140	—
88.	Manto/PCD	—	~115-~300?	~27-~36	—	—
89.	PCD	130-270	250-485	~32-~65	—	—
90.	Granite Sn/W	151-197	208-256	31.7-34.8	180	—

91.	Unconformity U	100-140	170-240	31-34	—	—
92.	PCD	200-560	460-650	up to ~80	—	—
93.	Metamorphic	80-190?	170-250	>26?	—	—
94.	Lode Au	81-138	169	28-30	—	—
95.	Granite REE	~100->600	~100->600?	35-80	225	—
96.	PCD	160-310	230-340	30-60	~300	—
97.	PCD	~60-~380	~225-~475	~33-~57	80-140	—
98.	Emeralds	180-190	260-340	38	106-112	—
99.	Synthetic FI	136.8-328.7	305.0-326.3	40	18-429	—
100.	PCD/Epithermal	~100-~500	170-518	30.5-62.2	~50-~400	—
101.	Vein	135-236	215-277	~34	~10-~70	—
102.	PGE	—	260-420	35	—	—
103.	Skarn	—	200-550	35->80	—	—
104.	IOCG	157-166	198-245	31-34	—	—
105.	Stratiform Cu	200-215	298-329	~38-~40	—	—
106.	PCD	239-392	328-491	38-60	—	—
107.	PCD	~125-~250	~200-~510	~31-~61	~65	—
108.	Granite	180-225	—	40-60	—	—
109.	Granite	70-150	220-430	32-48	>100	—
110.	PCD	—	240-320	30.5-38.8	>28	—
111.	BX Pipe	260-380	280-520	40-50	—	—
112.	Veins	150	320	37-38	—	—
113.	PCD	~50-~300	146-490	30-58	50-100	—
114.	Ophiolite	300-400	400-500	46-56	~50	~5
115.	Disseminated Au	179-224	215-347	32-42	—	—
116.	PCD/Shale-hosted	~155-~290	~165-~380	~32-~53	100-200	—
117.	Unconformity U	66-150	114->220	up to 60	—	—
118.	PCD	—	210-430	33-48	—	—
119.	Talc/Metamorphic	~110	150-300	36-42	—	—
120.	PCD	—	160-600	32-71	~100	—
121.	PCD	—	320->600	33->80	<50	—

122.	Metamorphic	—	90-140	23-35	—	—
123.	Granite/REE	89-329	147-428	29.6-48.7	—	—
124.	Greisen	~100-~400	~200->600	~26-~65	—	—
125.	Stratiform Cu	110-375	246-413	45-54	<120	—
126.	Geothermal	—	150->330	—	—	—
127.	Vein/PCD	259	317-403	55-65	>13	—
128.	PCD	~235-~380	~260-~490	~32-~60	—	—
129.	PCD	210-456	260-420	34-47	—	—
130.	Vein	65-410	120-490	—	—	—
131.	PCD	—	~400->580	—	—	—
132.	Vein/BX	—	~250-~500	>40	—	—
133.	PCD/BX Pipe	—	320-480	~36-~50	—	—
134.	PCD	205-290	280-330	~35-40	—	—
135.	PCD	—	260-520	35-55	—	—
136.	BX Pipe	—	~200-~400	~33-~47	17-126	—
137.	Skarn	400	460	—	—	—
138.	Stratiform Cu	160-220	270-320	~35	—	—
139.	PCD/Skarn	325.6-399.0	341.0-401.6	37.5-52.2	30	—
140.	Greenstone Au	~42-~190	~120-~300	—	—	—
141.	PCD	~340-~500	~300-~580	~50	—	—
142.	Granite	—	~340-~500	~38-~64	>50	1.8-2.2
143.	PCD	—	~210-370	33-45	—	—
144.	PCD	~350-400	~380-540	—	—	—
145.	Skarn	~300-~570	~330-~580	40-60	—	—
146.	PCD	—	~150-~575	~30-~77	40-80	2
147.	PCD	—	300-700	32-65	30	0.3
148.	PCD	~150-~420	~210-~450	—	—	—
149.	PCD	—	200-500	~30-~53	110	—
150.	PCD/Skarn	~180-~540	up to 540?	~32-~64	<200	—
151.	PCD	~265-~395	~275-~500	50-70?	—	—
152.	Manto	150-400	~260-~700	32-60	30-270	—

153.	The Halite Trend	—	—	—	—	—
154.	PCD	—	~275-~475	31-60	5.5-250	8
155.	PCD	—	320-600?	63-75	—	—
156.	PCD	—	250-450	36-61	—	—
157.	PCD	—	—	—	60-200	—
158.	PCD	—	300-500	33-45	—	—
159.	BX Pipe	—	up to 350	>30	—	—
160.	Veins	37-120	97-225	—	—	—
161.	Intrusion Sn/W	~240-~470	~300-~600	28-47	—	—

1. Niiranen, T., Poutiainen, M., and Mänttäri, I. (2007) *Geology, geochemistry, fluid inclusion characteristics, and U–Pb age studies on iron oxide–Cu–Au deposits in the Kolari region, northern Finland.* Ore Geology Reviews. 30: p. 75-105.
2. Kesler, S.E., Reich, M., and Jean, M. (2007) *Geochemistry of fluid inclusion brines from Earth's oldest Mississippi Valley-type (MVT) deposits, Transvaal Supergroup, South Africa.* Chemical Geology. 237: p. 274-288.
3. Fall, A., et al. (2007) *Fluid evolution in the nepheline syenites of the Ditrau Alkaline Massif, Transylvania, Romania.* Lithos. 95: p. 331-345.
4. Faleiros, F.M., et al. (2007) *Fault-valve action and vein development during strike-slip faulting: an example from the Ribeira Shear Zone, Southeastern Brazil.* Tectonophysics. in press.
5. Zhang, D., et al. (2006) *High salinity fluid inclusions in the Yinshan polymetallic deposit from the Le-De metallogenic belt in Jiangxi Province, China: Their origin and implications for ore genesis.* Ore Geology Reviews. in press.
6. Yang, F., et al. (2006) *Geology and geochemistry of the Bulong quartz-barite vein-type gold deposit in the Xingjiang Uygur Autonomous Region, China.* Ore Geology Reviews. 29: p. 52-76.
7. Vapnik, Y., et al. (2006) *Fluid inclusion and mineralogical study of vein-type apatite ores in shear zones from the Singhbhum metallogenetic province, West Bengal, India.* Ore Geology Reviews. in press.
8. Scherbarth, N.L. and Spry, P.G. (2006) *Mineralogical, Petrological, Stable Isotope, and Fluid Inclusion Characteristics of the Tuvatu Gold-Silver Telluride Deposit, Fiji: Comparisons with the Emperor Deposit.* Economic Geology. 101: p. 135-158.
9. Moura, M.A., et al. (2006) *Granite-Related Paleoproterozoic, Serrinha Gold Deposit, Southern Amazonia, Brazil: Hydrothermal Alteration, Fluid Inclusion and Stable Isotope Constraints on Genesis and Evolution.* Economic Geology. 101: p. 585-605.
10. Kendrick, M.A., Phillips, D., and Miller, J.M. (2006) *Part I. Decrepitation and degassing behaviour of quartz up to 1560.* Geochimica et Cosmochimica Acta. 70: p. 2540-2561.

11. Hezarkhani, A. (2006) *Mineralogy and fluid inclusion investigations in the Reagan Porphyry System, Iran, the path to an uneconomic porphyry copper deposit.* Journal of Asian Earth Sciences. 27: p. 598-612.
12. Hezarkhani, A. (2006) *Hydrothermal evolution of the Sar-Cheshmeh porphyry Cu-Mo deposit, Iran: Evidence from fluid inclusions.* Journal of Asian Earth Sciences. 28: p. 409-422.
13. Bouzari, F. and Clark, A.H. (2006) *Prograde Evolution and Geothermal Affinities of a Major Porphyry Copper Deposit: The Cerro Colorado Hypogene Protore, I Region, Northern Chile.* Economic Geology. 101: p. 95-134.
14. Moura, A. (2005) *Fluids from the Neves Corvo massive sulphide ores, Iberian Pyrite Belt, Portugal.* Chemical Geology. 223: p. 153-169.
15. Mishra, B., Pal, N., and Sarbadhikari, A.B. (2005) *Fluid inclusion characteristics of the Uti gold deposit, Hutti-Maski greenstone belt, southern India.* Ore Geology Reviews. 26: p. 1-16.
16. Masterman, G.J., et al. (2005) *Fluid Chemistry, Structural Setting, and Emplacement History of the Rosario Cu-Mo Porphyry and Cu-Ag-Au Epithermal Veins, Collahuasi District, Northern Chile.* Economic Geology. 100: p. 835-862.
17. Landtwing, M.R., et al. (2005) *Copper deposition during quartz dissolution by cooling magmatic-hydrothermal fluids: The Bingham porphyry.* Earth and Planetary Science Letters. 235: p. 229-243.
18. Hanley, J.J., et al. (2005) *Ore metal redistribution by hydrocarbon-brine and hydrocarbon-halite melt phases, North Range footwall of the Sudbury Igneous Complex, Ontario, Canada.* Mineralium Deposita. 40: p. 237-256.
19. Frikken, P.H., et al. (2005) *Mineralogical and Isotopic Zonation in the Sur-Sur Tourmaline Breccia, Rio Blanco-Los Bronces Cu-Mo Deposit, Chile: Implications for Ore Genesis.* Economic Geology. 100: p. 935-961.
20. Derome, D., et al. (2005) *Mixing of Sodic and Calcic Brines and Uranium Deposition at McArthur River, Saskatchewan, Canada: A Raman and Laser-Induced Breakdown Spectroscopic Study of Fluid Inclusions.* Economic Geology. 100: p. 1529-1545.
21. Davidson, P., et al. (2005) *Magmatic Precursors of Hydrothermal Fluids at the Rio Blanco Cu-Mo Deposit, Chile: Links to Silicate Magmas and Metal Transport.* Economic Geology. 100: p. 963-978.
22. Yang, K. and Bodnar, R.J. (2004) *Orthomagmatic origin for the Ilkwang Cu-W breccia-pipe deposit, southeastern Kyongsang Basin, South Korea.* Journal of Asian Earth Sciences. 24: p. 259-270.
23. Seedorff, E. and Einaudi, M.T. (2004) *Henderson Porphyry Molybdenum System, Colorado: II. Decoupling of Introduction and Deposition of Metals during Geochemical Evolution of Hydrothermal Fluids.* Economic Geology. 99: p. 39-72.
24. Polito, P.A., et al. (2004) *Significance of Alteration Assemblages for the Origin and Evolution of the Proterozoic Nabarlek Unconformity-Related Uranium Deposit, Northern Territory, Australia.* Economic Geology. 99: p. 113-139.
25. Kodera, P., et al. (2004) *Fluid Evolution in a Subvolcanic Granodiorite Pluton Related to Fe and Pb-Zn Mineralization, Banska Stiavnica Ore District, Slovakia.* Economic Geology. 99: p. 1745-1770.
26. Goldfarb, R.J., et al. (2004) *The Late Cretaceous Donlin Creek Gold Deposit, Southwestern Alaska: Controls on Epizonal Ore Formation.* Economic Geology. 99: p. 643-671.

27. Chang, Z. and Meinert, L.D. (2004) *The magmatic-hydrothermal transition—evidence from quartz phenocryst textures and endoskarn abundance in Cu-Zn skarns at the Empire Mine, Idaho, USA.* Chemical Geology. 210: p. 149-171.
28. Calagari, A.A. (2004) *Fluid inclusion studies in quartz veinlets in the porphyry copper deposit at Sungun, East-Azarbaidjan, Iran.* Journal of Asian Earth Sciences. 23: p. 179-189.
29. Beuchat, S., Moritz, R., and Pettke, T. (2004) *Fluid evolution in the W-Cu-Zn-Pb San Cristobal vein, Peru: fluid inclusion and stable istope evidence.* Chemical Geology. 210: p. 201-224.
30. Wilson, A.J., Cooke, D.R., and Harper, B.L. (2003) *The Ridgeway Gold-Copper Deposit: A High-Grade Alkalic Porphyry Deposit in the Lachlan Fold Belt, New South Wales, Ausralia.* Economic Geology. 98: p. 1637-1666.
31. Wanhainen, C., Broman, C., and Martinsson, O. (2003) *The Aitik Cu-Au-Ag deposit in northern Sweden: a product of high salinity fluids.* Mineralium Deposita. 38: p. 715-726.
32. Tarkian, M., et al. (2003) *Precioius-metal distribution and fluid-inclusion petrography of the Elatsite porphyry copper deposit, Bulgaria.* Mineralium Deposita. 38: p. 261-281.
33. Skewes, A.M., Holmgren, C., and Stern, C.R. (2003) *The Donoso copper-rich, tourmaline-bearing breccia pipe in central Chile: petrologic, fluid inclusion and stable isotope evidence for an origin from magmatic fluids.* Mineralium Deposita. 38: p. 2-21.
34. Rusk, B.G., *Cathodoluminescent quartz textures and fluid inclusions in veins of the porphyry copper–molybdenum deposit in Butte, Montana: Constraints on the physical and chemical evolution of the hydrothermal system*, in *Geology*. 2003, University of Oregon. p. 235.
35. Poutiainen, M. and Partamies, S. (2003) *Fluid Inclusion Characteristics of Auriferous Quartz Veins in Archean and Paleoproterozoic Greenstone Belts of Eastern and Southern Finland.* Economic Geology. 98: p. 1355-1369.
36. Mao, J., et al. (2003) *Fluid Inclusion and Noble Gas Studies of the Dongping Gold Deposit, Hebei Province, China: A Mantle Connection for Mineralization?* Economic Geology. 98: p. 517-534.
37. Lickfold, V., et al. (2003) *Endeavour Copper-Gold Porphyry Deposits, Northparkes, New South Wales: Intrusive History and Fluid Evolution.* Economic Geology. 98: p. 1607-1636.
38. Gleeson, S.A., et al. (2003) *Infiltration of basinal fluids into high-grade basement, South Norway: sources and behaviour of waters and brines.* Geofluids. 3: p. 33-48.
39. Baker, T. and Lang, J.R. (2003) *Reconciling fluid inclusion types, fluid processes, and fluid sources in skarns: an example from the Bismark Deposit, Mexico.* Mineralium Deposita. 38: p. 474-495.
40. Ulrich, T., Gunther, D., and Heinrich, C.A. (2002) *The Evolution of a Porphyry Cu-Au Deposit, Based on LA-ICP-MS Analysis of Fluid Inclusions: Bajo de la Alumbrera, Argentina.* Economic Geology. 97: p. 1889-1920.
41. Ulrich, T., et al. (2002) *Different mineralization styles in a volcanic-hosted ore deposit: the fluid and isotopic signatures of the Mt Morgan Au-Cu deposit, Australia.* Ore Geology Reviews. 22: p. 61-90.

42. Skirrow, R.G. and Walshe, J.L. (2002) *Reduced and Oxidized Au-Cu-Bi Iron Oxide Deposits of the Tennant Creek Inlier, Australia: An Integrated Geologic and Chemical Model.* Economic Geology. 97: p. 1167-1202.
43. Ruano, S.M., Both, R.A., and Golding, S.D. (2002) *A fluid inclusion and stable isotope study of the Moonta copper-gold deposits, South Australia: evidence for fluid immiscibility in a magmatic hydrothermal system.* Chemical Geology. 192: p. 211-226.
44. Pandalai, H.S., et al. (2002) *Dissolution channels in quartz and the role of pressure changes in gold and sulfide deposition in the Archean, greenstone-hosted, Hutti gold deposit, Karnataka, India.* Mineralium Deposita. 38: p. 597-624.
45. Neumayr, P. and Hagemann, S.G. (2002) *Hydrothermal Fluid Evolution within the Cadillac Tectonic Zone, Abitibi Greenstone Belt, Canada: Relationship to Auriferous Fluids in Adjacent Second- and Third-Order Shear Zones.* Economic Geology. 97: p. 1203-1225.
46. Melfos, V., et al. (2002) *Origin and evolution of hte Tertiary Maronia porphyry copper-molybdenum deposit, Thrace, Greece.* Mineralium Deposita. 37: p. 648-668.
47. Kontak, D.J. and Clark, A.H. (2002) *Genesis of the Giant, Bonanza San Rafael Lode Tin Deposit, Peru: Origin and Significance of Pervasive Alteration.* Economic Geology. 97: p. 1741-1777.
48. Ishizuka, O., Yuasa, M., and Uto, K. (2002) *Evidence of porphyry copper-type hydrothermal activity from a submerged remnant back-arc volcano of the Izu-Bonin arc. Implications for the volcanotectonic history of back-arc seamounts.* Earth and Planetary Science Letters. 198: p. 381-399.
49. Campos, E., et al. (2002) *Overheated, Cu-bearing magmas in the Zaldivar porphyry-Cu deposit, Northern Chile. Geodynamic consequences.* Tectonophysics. 345: p. 229-251.
50. Zachariás, J., et al. (2001) *Geology and genesis of Variscan porphyry-style gold mineralization, Petrackova hora deposit, Bohemian Massif, Czech Republic.* Mineralium Deposita. 36: p. 517-541.
51. Selby, D., et al. (2001) *Evidence for a nonmagmatic component in potassic hydrothermal fluids of porphyry Cu-Au-Mo systems, Yukon, Canada.* Geochimica et Cosmochimica Acta. 64: p. 571-587.
52. Muntean, J.L. and Einaudi, M.T. (2001) *Porphyry-Epithermal Transition: Maricunga Belt, Northern Chile.* Economic Geology. 96: p. 743-772.
53. Molnár, F., Watkinson, D.H., and Jones, P.C. (2001) *Multiple Hydrothermal Processes in Footwall Units of the North Range, Sudbury Igneous Complex, Canada, and Implications for the Genesis of Vein-Type Cu-Ni-PGE Deposits.* Economic Geology. 96: p. 1645-1670.
54. Kelley, D.S. and Früh-Green, G.L. (2001) *Volatile lines of descent in submarine plutonic environments: Insights from stable isotope and fluid inclusion analyses.* Geochimica et Cosmochimica Acta. 65: p. 3325-3346.
55. Campbell, A.R., Lundberg, S.A.W., and Dunbar, N.W. (2001) *Solid inclusions of halite in quartz: evidence for the halite trend.* Chemical Geology. 173: p. 179-191.

56. Brathwaite, R.L., et al. (2001) *Telescoped porphyry Cu-Mo-Au mineralisation, advanced argillic alteration and quartz-sulphide-gold-anhydrite veins in the Thames District, New Zealand.* Mineralium Deposita. 36: p. 623-640.
57. Boiron, M., et al. (2001) *Geometry and P–V–T–X conditions of microfissural ore fluid migration: the Mokrsko gold deposit (Bohemia).* Chemical Geology. 173: p. 207-225.
58. Baker, T., et al. (2001) *Radiogenic and Stable Isotope Constraints on the Genesis of the Eloise Cu-Au Deposit, Cloncurry District, Northwest Queensland.* Economic Geology. 96: p. 723-742.
59. Baker, T. and Lang, J.R. (2001) *Fluid inclusion characteristics of intrusion-related gold mineralization, Tombstone-Tungsten magmatic belt, Yukon Territory, Canada.* Mineralium Deposita. 36: p. 563-582.
60. Xu, G. and Lin, X. (2000) *Geology and geochemistry of the Changlongshan skarn iron deposit, Anhui Province, China.* Ore Geology Reviews. 16: p. 91-106.
61. Smith, M.P. and Henderson, P. (2000) *Preliminary Fluid Inclusion Constraints on Fluid Evolution in the Bayan Obo Fe-REE-Nb Deposit, Inner Mongolia, China.* Economic Geology. 95: p. 1371-1388.
62. Selby, D., et al. (2000) *Hydrothermal Alteration and Fluid Chemistry of the Endako Porphyry Molybdenum Deposit, British Columbia.* Economic Geology. 95: p. 183-202.
63. Perring, C.S., et al. (2000) *The Lightning Creek Sill Complex, Cloncurry District, Northwest Queensland: A Source of Fluids for Fe Oxide Cu-Au Mineralization and Sodic-Calcic Alteration.* Economic Geology. 95: p. 1067-1089.
64. Gleeson, S.A., et al. (2000) *From basin to basement: the movement of surface fluids into the crust.* Journal of Geochemical Exploration. 69-70: p. 527-531.
65. Franchini, M.B., et al. (2000) *Skarns Related to Porphyry-Style Mineralization at Caicayen Hill, Neuquen, Argentina: Composition and Evolution of Hydrothermal Fluids.* Economic Geology. 95: p. 1197-1213.
66. Wang, Y., et al. (1999) *Fluid inclusion studies of the Chinkuashih high-sulfidation gold-copper deposits in Taiwan.* Chemical Geology. 154: p. 155-167.
67. Prokofiev, V., et al. (1999) *Evolution of magmatic fluids at the Banska Stiavnica precious and base metal deposit, Slovakia-evidence from melt and fluid inclusions.* Economic Geology. 1999: p. 949-956.
68. Molnár, F., Watkinson, D.H., and Everest, J.O. (1999) *Fluid-inclusion characteristics of hydrothermal Cu-Ni-PGE veins in granitic and metavolcanic rocks at the contact of the Little Stobie deposit, Sudbury, Canada.* Chemical Geology. 154: p. 279-301.
69. Mishra, B. and Panigrahi, M.K. (1999) *Fluid evolution in the Kolar Gold Field: evidence from fluid inclusion studies.* Mineralium Deposita. 34: p. 173-181.
70. Huizenga, J.M. (1999) *Fluid evolution in the Pote Shear Zone Harare-Shamva-Bindura greenstone belt (northeast Zimbabwe).* Journal of African Earth Sciences. 28: p. 311-324.
71. Xu, G. (1998) *A Fluid Inclusion Study of Syntectonic Zn-Pb-Ag Mineralization at Dugald River, Northwest Queensland, Australia.* Economic Geology. 93: p. 1165-1179.

72. Williams, P.J., Pendergast, W.J., and Dong, G. (1998) *Late Orogenic Alteration in the Wall Rocks of the Pegmont Pb-Zn Deposit, Cloncurry District, Queensland, Australia.* Economic Geology. 93: p. 1180-1189.
73. Taner, H., Williams-Jones, A.E., and Wood, S.A. (1998) *The nature, origin, and physicochemical controls of hydrothermal Mo-Bi mineralization in the Cadillac deposit, Quebec, Canada.* Mineralium Deposita. 33: p. 579-590.
74. Hezarkhani, A. and Williams-Jones, A.E. (1998) *Controls of alteration and mineralization in the Sungun porphyry copper deposit, Iran: Evidence from fluid inclusions and stable isotopes.* Economic Geology. 93: p. 651-670.
75. Halter, W.E., Williams-Jones, A.E., and Kontak, D.J. (1998) *Origin and evolution of the greisenizing fluid at the East Kemptville tin deposit, Nova Scotia, Canada.* Economic Geology. 93: p. 1026-1051.
76. Field, M.P., Kerrich, R., and Kyser, T.K. (1998) *Characteristics of Barren Quartz Veins in the Proterozoic La Ronge Domain, Saskatchewan, Canada: A Comparison With Auriferous Counterparts.* Economic Geology. 93: p. 602-616.
77. Cannell, J. and Davidson, G.J. (1998) *A Carbonate-Dominated Copper-Cobalt Breccia-Vein System at the Great Australia Deposit, Mount Isa Eastern Succession.* Economic Geology. 93: p. 1406-1421.
78. Boullier, A., Firdaous, K., and Robert, F. (1998) *On the significance of aqueous fluid inclusions in gold-bearing quartz vein deposits from the southeastern Abitibi subprovince (Quebec, Canada).* Economic Geology. 93: p. 216-223.
79. Borrok, D.M., et al. (1998) *The Vergenoeg magnetite-fluorite deposit, South Africa: Support for a hydrothermal model for massive iron oxide deposits.* Economic Geology. 93: p. 564-586.
80. Baker, T. (1998) *Alteration, Mineralization, and Fluid Evolution at the Eloise Cu-Au Deposit, Cloncurry District, Northwest Queensland, Australia.* Economic Geology. 93: p. 1213-1236.
81. Mulshaw, S.C., et al. (1997) *Genesis of Epizonal Ag Vein Mineralization at San Bartolomé in Central Ecuador: Textural Evidence, Fluid Inclusions, and Stable Isotope Geochemistry.* Economic Geology. 92: p. 210-227.
82. Molnár, F., et al. (1997) *Fluid inclusion evidence for hydrothermal enrichment of magmatic ore at the contact zone of the Ni-Cu-platinum-group element 4b deposit, Lindsley Mine, Sudbury, Canada.* Economic Geology. 92: p. 674-685.
83. Meinert, L.D., et al. (1997) *Geology, zonation, and fluid evolution of the Big Gossan Cu-Au skarn deposit, Ertsberg district, Irian Jaya.* Economic Geology. 92: p. 509-534.
84. En-Naciri, A., Barbanson, L., and Touray, J. (1997) *Brine inclusions from the Co-As(Au) Bou Azzer District, Anti-Atlas Mountains, Morocco.* Economic Geology. 92: p. 360-367.
85. Stefanini, B. and Williams-Jones, A.E. (1996) *Hydrothermal Evolution in the Calabona Porphyry Copper System (Sardinia, Italy): The Path to an Uneconomic Deposit.* Economic Geology. 91: p. 774-791.
86. Spry, P.G., et al. (1996) *Evidence for a Genetic Link Between Gold-Silver Telluride and Porphyry Molybdenum Mineralization at the Golden Sunlight Deposit, Whitehall, Montana: Fluid Inclusion and Stable Isotope Studies.* Economic Geology. 91: p. 507-526.
87. Sachan, H.K. (1996) *Cooling history of subduction related granite from the Indus Suture Zone, Ladakh, India: evidence from fluid inclusions.* Lithos. 38: p. 81-92.

88. Oyarzun, R., et al. (1996) *The Manto-Type Gold Deposits of Andacollo (Chile) Revisited: A Model Based on Fluid Inclusion and Geologic Evidence.* Economic Geology. 91: p. 1298-1309.
89. Ren, S.K., et al. (1995) *Magmatic and hydrothermal history of the porphyry-style deposits of the Ardlethan tin field, New South Wales, Australia.* Economic Geology. 90: p. 1620-1645.
90. Linnen, R.L. and Williams-Jones, A.E. (1995) *Genesis of a Magmatic Metamorphic Hydrothermal System: The Sn-W Polymetallic Deposits at Pilok, Thailand.* Economic Geology. 90: p. 1148-1166.
91. Kotzer, T.G. and Kyser, T.K. (1995) *Petrogenesis of the Proterozoic Athabasca Basin, northern Saskatchewan, Canada, and its relation to diagenesis, hydrothermal uranium mineralization and paleohydrogeology.* Chemical Geology. 120: p. 45-89.
92. Heithersay, P.S. and Walshe, J.L. (1995) *Endeavour 26 North: A porphyry copper-gold deposit in the late Ordovician, shoshonitic Goonumbla volcanic complex, New South Wales, Australia.* Economic Geology. 90: p. 1506-1532.
93. Heinrich, C.A., et al. (1995) *Fluid and Mass Transfer during Metabasalt Alteration and Copper Mineralization at Mount Isa, Australia.* Economic Geology. 90: p. 705-730.
94. Fayek, M. and Kyser, T.K. (1995) *Characteristics of Auriferous and Barren Fluids Associated with the Proterozoic Contact Lake Lode Gold Deposit, Saskatchewan, Canada.* Economic Geology. 90: p. 385-406.
95. Campbell, A.R., et al. (1995) *Geochemistry of Th-U-REE Mineralizing Magmatic Fluids, Capitan Mountains, New Mexico.* Economic Geology. 90: p. 1271-1287.
96. Yang, K. and Bodnar, R.J. (1994) *Magmatic-Hydrothermal Evolution in the "Bottoms" of Porphyry Copper Systems: Evidence from Silicate Melt and Aqueous Fluid Inclusions in Granitoid Intrusions in the Gyeongsang Basin, South Korea.* International Geology Review. 36: p. 608-628.
97. Cline, J.S. and Bodnar, R.J. (1994) *Direct evolution of a brine from crystallizing silicic melt at the Questa, New Mexico, molybdenum deposit.* Economic Geology. 89: p. 1780-1802.
98. Cheilletz, A., et al. (1994) *Time-Pressure and Temperature Constraints on the Formation of Colombian Emeralds: An 40Ar/39Ar Laser Microprobe and Fluid Inclusion Study.* Economic Geology. 89: p. 361-380.
99. Bodnar, R.J. (1994) *Synthetic fluid inclusions. XII. Experimental determination of the liquidus and isochores for a 40 wt.% H_2O-NaCl solution.* Geochimica et Cosmochimica Acta. 58: p. 1053-1063.
100. Richards, J.P. and Kerrich, R. (1993) *The Porgera Gold Mine, Papua New Guinea: Magmatic Hydrothermal to Epithermal Evolution of an Alkalic-type Precious Metal Deposit.* Economic Geology. 88: p. 1017-1052.
101. Marshall, D.D., Diamond, L.W., and Skippen, G.B. (1993) *Silver Transport and Deposition at Cobalt, Ontario, Canada: Fluid Inclusion Evidence.* Economic Geology. 88: p. 837-854.
102. Li, C. and Naldrett, A.J. (1993) *High Chlorine Alteration Minerals and Calcium-rich Brines in Fluid Inclusions from the Strathcona Deep Copper Zone, Sudbury, Ontario.* Economic Geology. 88: p. 1780-1796.
103. Jamtveit, B. and Anderson, T. (1993) *Contact Metamorphism of Layered Shale-Carbonate Sequences in the Oslo Rift: III. The Nature of Skarn-Forming Fluids.* Economic Geology. 88: p. 1830-1849.

104. Oreskes, N. and Einaudi, M.T. (1992) *Origin of Hydrothermal Fluids at Olympic Dam: Preliminary Results from Fluid Inclusions and Stable Isotopes.* Economic Geology. 87: p. 64-90.
105. Knutson, J., et al. (1992) *Hydrothermal Alteration of Middle Proterozoic Basalts, Stuart Shelf, South Australia -- a possible source for Cu mineralization.* Economic Geology. 87: p. 1054-1077.
106. Frezzotti, M.L., Ghezzo, C., and Stefanini, B. (1992) *The Calabona Intrusive Complex (Sardinia, Italy): Evidence for a Porphyry Copper System.* Economic Geology. 87: p. 425-436.
107. Dilles, J.H. and Einaudi, M.T. (1992) *Wall-Rock Alteration and Hydrothermal Flow Paths about the Ann-Mason Porphyry Copper Deposit, Nevada--A 6-Km Vertical Reconstruction.* Economic Geology. 87: p. 1963-2001.
108. Cuney, M., Marignac, C., and Weisbrod, A. (1992) *The Beauvoir Topaz-Lepidolite Albite Granite (Massif Central, France): The Disseminated Magmatic Sn-Li-Ta-Nb-Be Mineralization.* Economic Geology. 87: p. 1766-1794.
109. Pollard, P.J., Andrew, A.S., and Taylor, R.G. (1991) *Fluid Inclusion and Stable Isotope Evidence for Interaction between Granites and Magmatic Hydrothermal Fluids during Formation of Disseminated and Pipe-Style Mineralization at the Zaaiplaats Tin Mine.* Economic Geology. 86: p. 121-141.
110. Nast, H.J. and Williams-Jones, A.E. (1991) *The Role of Water-Rock Interaction and Fluid Evolution in Forming the Porphyry-Related Sisson Brook W-Cu-Mo Deposit, New Brunswick.* Economic Geology. 86: p. 302-317.
111. Baker, E.M. and Andrew, A.S. (1991) *Geologic, Fluid Inclusion, and Stable Isotope Studies of the Gold-Bearing Breccia Pipe at Kidston, Queensland, Australia.* Economic Geology. 86: p. 810-830.
112. Schreiber, D.W., Fontboté, L., and Lochmann, D. (1990) *Geologic Setting, Paragenesis, and Physicochemistry of Gold Quartz Veins Hosted by Plutonic Rocks in the Pataz Region.* Economic Geology. 85: p. 1328-1347.
113. Samson, I.M. (1990) *Fluid Evolution and Mineralization in a Subvolcanic Granite Stock: The Mount Pleasant W-Mo-Sn Deposits, New Brunswick, Canada.* Economic Geology. 85: p. 145-163.
114. Kelley, D.S. and Robinson, P.T. (1990) *Development of a brine-dominated hydrothermal system at temperatures of 400–500°C in the upper level plutonic sequence, Troodos ophiolite, Cyprus.* Geochimica et Cosmochimica Acta. 54: p. 653-661.
115. Kavalieris, I., et al. (1990) *Dome-Related Gold Mineralization in the Pani Volcanic Complex, North Sulawesi, Indonesia: A Study of Geologic Relations, Fluid Inclusions, and Chlorite Compositions.* Economic Geology. 85: p. 1208-1225.
116. Williams-Jones, A.E., Samson, I.M., and Linnen, R.L. (1989) *Fluid Evolution and Its Role in the Genesis of the Granite-Related Madeleine Copper Deposit, Gaspé, Quebec.* Economic Geology. 84: p. 1515-1524.
117. Wilde, A.R., et al. (1989) *Fluid Inclusion Evidence on the Origin of Some Australian Unconformity-Related Uranium Deposits.* Economic Geology. 84: p. 1627-1642.
118. Richards, J.P. and Spooner, E.T.C. (1989) *Evidence for Cu-(Ag) Mineralization by Magmatic-Meteoric Fluid Mixing in Keweenawan Fissure Veins, Mamainse Point, Ontario.* Economic Geology. 84: p. 360-385.

119. Moine, B., et al. (1989) *Comparative Mineralogy, Geochemistry, and Conditions of Formation of Two Metasomatic Talc and Chlorite Deposits: Trimouns (Pyrenees, France) and Rabenwald (Eastern Alps, Austria).* Economic Geology. 84: p. 1398-1416.
120. John, D.A. (1989) *Geologic Setting, Depths of Emplacement, and Regional Distribution of Fluid Inclusions in Intrusions of the Central Wasatch Mountains, Utah.* Economic Geology. 84: p. 386-409.
121. John, D.A. (1989) *Evolution of Hydrothermal Fluids in the Park Premier Stock, Central Wasatch Mountains, Utah.* Economic Geology. 84: p. 879-902.
122. Heinrich, C.A., Andrew, A.S., and Wilkins, R.W.T. (1989) *A Fluid Inclusion and Stable Isotope Study of Synmetamorphic Copper Ore Formation at Mount Isa, Australia.* Economic Geology. 84: p. 529-550.
123. Charoy, B. and Pollard, P.J. (1989) *Albite-Rich, Silica-Depleted Metasomatic Rocks at Emuford, Northeast Queensland: Mineralogical, Geochemical, and Fluid Inclusion Constraints on Hydrothermal Evolution and Tin Mineralization.* Economic Geology. 84: p. 1850-1874.
124. Witt, W.K. (1988) *Evolution of High-Temperature Hydrothermal Fluids Associated with Greisenization and Feldspathic Alteration of a Tin-Mineralized Granite, Northeast Queensland.* Economic Geology. 83: p. 310-334.
125. Richards, J.P., Krogh, T.E., and Spooner, E.T.C. (1988) *Fluid inclusion characteristics and U-Pb rutile age of late hydrothermal alteration and veining at the Musoshi stratiform copper deposit, Central Africa Copper Belt, Zaire.* Economic Geology. 83: p. 118-139.
126. McKibben, M.A., Williams, A.E., and Okubo, S. (1988) *Metamorphosed Plio-Pleistocene evaporites and the origins of hypersaline brines in the Salton Sea geothermal system, California: Fluid inclusion evidence.* Geochimica et Cosmochimica Acta. 52: p. 1047-1056.
127. Gilmer, A.L., et al. (1988) *Sierra de Santa Maria, Velardeña Mining District, Durango, Mexico.* Economic Geology. 83: p. 1802-1829.
128. Hein, U.F. and Tistl, M. (1987) *Characteristics of fluid inclusions in the porphyry copper deposit at La Granja, Peru.* Chemical Geology. 61: p. 183-192.
129. Ringrose, C.R., et al. (1986) *Stable isotope geochemistry of a porphyry-style hydrothermal system, West Silverton District, San Juan Mountains, Colorado, U.S.A.* Applied Geochemistry. 1: p. 357-373.
130. Kerrich, R., et al. (1986) *The silver deposits at Cobalt and Gowganda, Ontario. III: Hydrothermal regimes and source reservoirs-evidence from H, O, C, and Sr isotopes and fluid inclusions.* Canadian Journal of Earth Sciences. 23: p. 1519-1550.
131. Eastoe, C.J. and Eadington, P.J. (1986) *High-temperature fluid inclusions and the role of the biotite granodiorite in mineralization at the Panguna porphyry copper deposit, Bougainville, Papua New Guinea.* Economic Geology. 81: p. 478-483.
132. Thompson, T.B., Trippel, A.D., and Dwelley, P.C. (1985) *Mineralized Veins and Breccias of the Cripple Creek District, Colorado.* Economic Geology. 80: p. 1669-1688.

133. Scherkenbach, D.A., Sawkins, F.J., and Seyfied Jr., W.E. (1985) *Geologic, Fluid Inclusion, and Geochemical Studies of the Mineralized Breccias at Cumobabi, Sonora, Mexico.* Economic Geology. 80: p. 1566-1592.
134. Rice, C.M., Harmon, R.S., and Shepherd, T.J. (1985) *Central City, Colorado; The Upper Part of an Alkaline Porphyry Molybdenum System.* Economic Geology. 80: p. 1769-1796.
135. Reynolds, T.J. and Beane, R.E. (1985) *Evolution of Hydrothermal Fluid Characteristics at the Santa Rita, New Mexico, Porphyry Copper Deposit.* Economic Geology. 80: p. 1328-1347.
136. Norman, D.I. and Sawkins, F.J. (1985) *The Tribag Breccia Pipes: Precambrian Cu-Mo Deposits, Batchawana Bay, Ontario.* Economic Geology. 80: p. 1593-1621.
137. Meinert, L.D. (1984) *Mineralogy and Petrology of Iron Skarns in Western British Columbia, Canada.* Economic Geology. 79: p. 869-882.
138. Lambert, I.B., et al. (1984) *Genesis of Late Proterozoic Copper Mineralization, Copper Claim, South Australia.* Economic Geology. 79: p. 461-475.
139. Shelton, K.L. (1983) *Composition and origin of ore-forming fluids in a carbonate-hosted porphyry copper and skarn deposit: A fluid inclusions and stable isotope study of Mines Gaspé, Quebec.* Economic Geology. 78: p. 387-421.
140. Guha, J., Archambault, G., and Leroy, J. (1983) *A Correlation between the Evolution of Mineralizing Fluids and the Geomechanical Development of a Shear Zone as Illustrated by the Henderson 2 Mine, Quebec.* Economic Geology. 78: p. 1605-1618.
141. Eastoe, C.J. (1983) *Sulfur Isotope Data and the Nature of the Hydrothermal Systems at the Panguna and Frieda Porphyry Copper Deposits, Papua New Guinea.* Economic Geology. 78: p. 201-213.
142. Chryssoulis, S. and Wilkinson, N. (1983) *High Silver Content of Fluid Inclusions in Quartz from Guadalcazar Granite, San Luis Potosi, Mexico: A Contribution to Ore-Genesis Theory.* Economic Geology. 78: p. 302-318.
143. Preece, R.K. and Beane, R.E. (1982) *Contrasting Evolutions of Hydrothermal Alteration in Quartz Monzonite and Quartz Diorite Wall Rocks at the Sierrita Porphyry Copper Deposit, Arizona.* Economic Geology. 77: p. 1621-1641.
144. Eastoe, C.J. (1982) *Physics and Chemistry of the Hydrothermal System at the Panguna Porphyry Copper Deposit, Bougainville, Papua New Guinea.* Economic Geology. 77: p. 127-153.
145. Kwak, T.A.P. and Tan, T.H. (1981) *The Geochemistry of Zoning in Skarn Minerals at the King Island (Dolphin) Mine.* Economic Geology. 76: p. 468-497.
146. Bloom, M.S. (1981) *Chemistry of Inclusion Fluids: Stockwork Molybdenum Deposits from Questa, New Mexico, and Hudson Bay Mountain and Endako, British Columbia.* Economic Geology. 76: p. 1906-1920.
147. Wilson, J.W.J., et al. (1980) *Fluid inclusion geochemistry of the Granisle and Bell porphyry copper deposits, British Columbia.* Economic Geology. 75: p. 45-61.
148. Denis, M., et al. (1980) *Le porphyre cuprifere de Sierrita-Esperanza, Arizona, U.S.A.; comparaison avec quelques porphyres voisins.* Bulletin de Mineralogie. 103: p. 613-622.

149. Bodnar, R.J. and Beane, R.E. (1980) *Temporal and spatial variations in hydrothermal fluid characteristics during vein filling in preore cover overlying deeply buried porphyry copper-type mineralization at Red Mountain, Arizona.* Economic Geology. 75: p. 876-893.
150. Ahmad, S.N. and Rose, A.W. (1980) *Fluid Inclusions in Porphyry and Skarn Ore at Santa Rita, New Mexico.* Economic Geology. 75: p. 229-250.
151. Ramboz, C. (1979) *A fluid inclusion study of the copper mineralization in Southwest Tintic District (Utah).* Bulletin de Mineralogie. 102: p. 622-632.
152. Erwood, R.J., Kesler, S.E., and Cloke, P.L. (1979) *Compositionally distinct, saline hydrothermal solutions, Naica Mine, Chihuahua, Mexico.* Economic Geology. 74: p. 95-108.
153. Cloke, P.L. and Kesler, S.E. (1979) *The Halite Trend in Hydrothermal Solutions.* Economic Geology. 74: p. 1823-1831.
154. Watmuff, G. (1978) *Geology and Alteration-Mineralization Zoning in the Central Portion of the Yandera Porphyry Copper Prospect, Papua New Guinea.* Economic Geology. 73: p. 829-856.
155. Eastoe, C.J. (1978) *A fluid inclusion study of the Panguna porphyry copper deposit, Bougainville, Papua New Guinea.* Economic Geology. 73: p. 721-748.
156. Chivas, A.R. and Wilkins, R.W.T. (1977) *Fluid inclusion studies in relation to hydrothermal alteration and mineralization at the Koloula porphyry copper prospect, Guadalcanal.* Economic Geology. 72: p. 153-169.
157. Berzina, A.P. and Sotnikov, V.I. (1977) *Physicochemical Conditions of Endogene Processes in Copper-Molybdenum Deposits in Central Asia.* Economic Geology. 72: p. 25-36.
158. Takenouchi, S. and Imai, H. (1975) *Glass and Fluid Inclusions in Acidic Igneous Rocks from Some Mining Areas in Japan.* Economic Geology. 70: p. 750-769.
159. Nash, J.T. and Cunningham Jr., C.G. (1973) *Fluid-Inclusion Studies of the Fluorspar and Gold Deposits, Jamestown District, Colorado.* Economic Geology. 68: p. 1247-1262.
160. Touray, J.C. and Sabouraud, C. (1970) *Metastable Inclusion Brine in Fluorite from Ouezzanne.* Economic Geology. 65: p. 216-218.
161. Kelly, W.C. and Turneaure, F.S. (1970) *Mineralogy, Paragenesis and Geothermometry of the Tin and Tungsten Deposits of the Eastern Andes, Bolivia.* Economic Geology. 65: p. 609-680.

Appendix B: FORTRAN Code

To facilitate the manipulation and reduction of data described in chapters 2 and 3, it was necessary to use computational methods. All equations describing phase equilibria of H_2O-NaCl fluids were programmed as subroutines written in FORTRAN90 style, and are intended to be used in a dynamic library that may be accessed by the R functions listed in Appendix C. Previously published equations were used when available. Where existing equations were not available or deemed not suitable, multiple stepwise regression models were developed to produce equations using both the data obtained during the course of this research, and from previously published sources. Below are listed the source code for all FORTRAN90 subroutines used in the research described in chapters 2 and 3, and also a UNIX Makefile that may be used to produce an R shared library. This code is known to work with R version 2.5 and gfortran 4.0 or newer on MacOS version 10.4, and on Gentoo Linux for x86, amd64, and ppc architectures. However, it should compile and run on any modern UNIX-like operating system where the GNU compiler version 4 or higher is available.

Makefile

```
FC=R CMD SHLIB

all: water_halite_equilibria

water_halite_equilibria:
	$(FC) saltfunctions.f90 halite_liquidus.f90 pvtnaclh2o1kb.f90 H2O_NaCl_model.f90 -o water_halite_equilibria.so
clean:
	rm -rf *.o *.so
```

saltfunctions.f90

```
! vapor saturated NaCl-KCl-H2O solubility from Sterner et al. 1988
! This subroutine calculates fluid compositions in the halite field, given an input temperature and ratio of salt species
subroutine wt_halite_ternary (T,wt_water,wt_NaCl,wt_KCl,wt_salt,R)
implicit none
double precision wt_salt,wt_water,wt_NaCl,wt_KCl,T,R,psi
psi = T/100.0D0
wt_salt = 39.19843568D0 + 13.59271070D0*psi + -12.95646989D0*R + -22.39663458D0*R*psi + -1.52357614D0*psi**2 + 9.296722450D0*R**2*&
  psi + 6.55485254D0*R**3*psi**2 + -0.66512956D0*R**3*psi**3 + -0.39464296D0*R*psi**3 + 0.83679331D0*psi**3 + -3.61131899D0*R**4*&
```

```
  psi**2 + 0.00275314D0*R*psi**7+ 0.00822892D0*R**2*psi**6 + -0.00608193D0*R**2*psi**7 + 0.00344002D0*R**3*psi**7 + -0.00531261D0*&
  R**6*psi**6 + 0.04128563D0*R**7*psi**4 +0.00629464D0*R**9*psi**5 + -0.00488294D0*psi**6
wt_water=100.0D0-wt_salt
wt_NaCl=R*wt_salt
wt_KCl=(1.0D0-R)*wt_salt
return
end subroutine wt_halite_ternary
!
!
! vapor saturated NaCl-KCl-H2O solubility from Sterner et al. 1988
! This subroutine calculates fluid compositions in the sylvite field, given an input temperature and ratio of salt species
subroutine wt_sylvite_ternary (T,wt_water,wt_NaCl,wt_KCl,wt_salt,R)
implicit none
double precision wt_salt,wt_water,wt_NaCl,wt_KCl,T,R,psi
psi = T/100.0D0
wt_salt = 21.88644809D0 + 20.27990158D0*psi + 3.25451170D0*R + -6.43202667D0*R*psi + -9.60299248D0*psi**2 + 7.03770644D0*R**2 + &
  5.80727278D0*R*psi**2 + 6.97961319D0*R**3*psi + -0.77994533D0*R*psi**3 + 4.07787875D0*psi**3 + -0.87240194D0*psi**4 + &
  0.00037040D0*R*psi**6 + -0.31288876D0*R**8*psi**6 + -9.92786125D0*R**9*psi**2 + 0.00215197D0*R**9*psi**9 + 17.59451286D0*R**9 + &
  0.09174297D0*psi**5 + -0.00377589D0*psi**6
wt_water=100.0D0-wt_salt
wt_NaCl=R*wt_salt
wt_KCl=(1.0D0-R)*wt_salt
return
end subroutine wt_sylvite_ternary
!
!
! vapor saturated NaCl-KCl-H2O solubility from Sterner et al. 1988
! This subroutine calculates fluid compositions in the hydrohalite field, given an input temperature and ratio of salt species
subroutine wt_hydrohalite_ternary (T,wt_water,wt_NaCl,wt_KCl,wt_salt,R)
implicit none
double precision wt_salt,wt_water,wt_NaCl,wt_KCl,T,R,psi
psi = T/100.0D0
wt_salt = 40.36947594D0 + 14.80771966D0*psi + -14.08238722D0*R
wt_water=100.0D0-wt_salt
wt_NaCl=R*wt_salt
wt_KCl=(1.0D0-R)*wt_salt
return
end subroutine wt_hydrohalite_ternary
!
!
! vapor saturated NaCl-KCl-H2O solubility from Sterner et al. 1988
! This subroutine calculates fluid compositions in the ice field, given an input temperature and ratio of salt species
subroutine wt_ice_ternary (T,wt_water,wt_NaCl,wt_KCl,wt_salt,R)
implicit none
double precision wt_salt,wt_water,wt_NaCl,wt_KCl,T,R,a,b,c,e
```

```
c = 0.4597 + 0.1440*R
e = 2.227D-04 + 1.999D-04*R + 4.633D-05*R**2 + 1.123D-04*R**3
a = c/e
b = T/e
wt_salt = ((-b/2.0) + (b**2.0/4.0 + a**3.0/27.0)**(1.0/2.0))**(1.0/3.0) - (-((-b/2.0) - (b**2.0/4.0 + a**3.0/27.0)**(1.0/2.0)))**&
  (1.0/3.0)
wt_water=100.0D0-wt_salt
wt_NaCl=R*wt_salt
wt_KCl=(1.0D0-R)*wt_salt
return
end subroutine wt_ice_ternary
!
!
! The equation in this subroutine calculates pressure as a function of temperature along the three phase curve in the H2O-NaCl system.
! This equation is a regression model of available data from published sources, including National Research Council (1928),
! Keevil (1942), Sourirajan and Kennedy (1968) (which was interpolated from Keevil), and Bischoff and Pitzer (1989)
subroutine P_NaCl_tp (P,T)
implicit none
double precision T,P,c0,c3,c4,c5,c6,c8,c10
P = 5.58886351D-2 + 1.91966278D-8*T**3 + 2.88161982D-12*T**5 - 4.94939187D-20*T**8 + 9.06542134D-23*T**9 - 4.48694938D-26*T**10
return
end subroutine P_NaCl_tp
!
!
! The equation in this subroutine calculates density as a function of temperature along the three phase curve in the H2O-NaCl system
! Equation was taken from Palliser and McKibbin (1998b)
subroutine RHO_NaCl_tp (RHO,T)
implicit none
double precision RHO,T,c0,c1,c2,c3,c4,c5,c6
c0 = 1.22004D3
c1 = -6.09462D2
c2 = 3.17390D3
c3 = -1.75541D4
c4 = 4.08000D4
c5 = -3.73488D4
c6 = 1.18784D4
T = T/800.0D0
RHO = (c0 + c1*T + c2*T**2 + c3*T**3 + c4*T**4 + c5*T**5 + c6*T**6)/1000.0D0
T = T*800.0D0
return
end subroutine RHO_NaCl_tp
!
!
! This subroutine implements a stepwise regression model of data combined from Potter (1977), NBS Steam Tables, and
! Palliser and McKibbin (1998a) to calculate densities of halite undersaturated H2O-NaCl solutions from 0 to 26.4 wt% at 25C.
```

```
subroutine rho_undersat_liq_25C (RHO,X)
implicit none
double precision RHO,X
RHO = 9.97254643D-1 + 6.10301828D-3*X + 4.89015158D-4*X**2 + -8.82887737D-5*X**3 + 7.37377004D-6*X**4 + -2.80025323D-7*X**5&
  + 3.95096149D-9*X**6
return
end subroutine rho_undersat_liq_25C
!
!
! This subroutine calculates temperature along the three phase curve in the H2O-NaCl system as a function of composition
! using an iterative calculation of Sterner et al (1998)'s halite-sylvite ternary equation
subroutine T_NaCl_tp (T,X)
implicit none
double precision X,T,R,wt_water,wt_NaCl,wt_KCl,wt_salt
R=1.0D0
T = 801.0D0
wt_NaCl = 100.1D0
do while (wt_NaCl .gt. X)
  call wt_halite_ternary(T,wt_water,wt_NaCl,wt_KCl,wt_salt,R)
  T = T - 0.01D0
end do
return
end subroutine T_NaCl_tp
!
!
! Given an input temperature, this subroutine calls on other subroutines that calculate pressure, density, and composition
! as a function of temperature along the three phase curve in the H2O-NaCl system and returns a single point along the three
! phase curve in PVTX space
subroutine PVTX_threephase_inputT (P,RHO,T,X)
implicit none
double precision P,RHO,T,X,wt_water,wt_NaCl,wt_KCl,wt_salt,R
R = 1.0D0
call P_NaCl_tp(P,T)
call RHO_NaCl_tp(RHO,T)
call wt_halite_ternary(T,wt_water,X,wt_KCl,wt_salt,R)
return
end subroutine PVTX_threephase_inputT
!
!
! Given an input composition, this subroutine calls on other subroutines that calculate pressure, density, and temperature
! as a function of composition along the three phase curve in the H2O-NaCl system and returns a single point along the three
! phase curve in PVTX space
subroutine PVTX_threephase_inputX (P,RHO,T,X)
implicit none
double precision P,RHO,T,X
```

```
call T_NaCl_tp(T,X)
call P_NaCl_tp(P,T)
call RHO_NaCl_tp(RHO,T)
return
end subroutine PVTX_threephase_inputX
!
!
! This subroutine calculates the slopes of isochores (or iso-Th lines) in the one phase field up to 40wt% NaCl using the
! equation of Bodnar and Vityk (1994).
subroutine dPdT_isoTh (Th,X,dPdT)
implicit none
double precision Th,X,aS,bS,cS,dPdT
aS = 18.28D0 + 1.4413D0*X + 0.0047241D0*X**2 - 0.0024213D0*X**3 + 0.000038064D0*X**4
bS = 0.019041D0 - 1.5268D-2*X + 5.6012D-4*X**2 - 4.2329D-6*X**3 - 3.0354D-8*X**4
cS = -1.5988D-4 + 3.6892D-5*X - 1.9473D-6*X**2 + 4.1674D-8*X**3 - 3.3008D-10*X**4
dPdT = (aS + bS*Th + cS*Th**2)/10.0D0
return
end subroutine dPdT_isoTh
!
!
! This subroutine calculates composition as a function of temperature along the critical curve; polynomial equation is a least
! squares regression analysis of data published by Bischoff and Pitzer (1989) and Anderko and Pitzer (1993).
subroutine X_NaCl_crit (T,X)
implicit none
double precision T,X,a0,a1,a2,a3,a4,a5,a6,a7,a8
a0 = 3.4755243099853838D03
a1 = -3.3663497788132124D-01
a2 = 2.5051585402794175D-03
a3 = -8.8458147276760685D-06
a4 = 1.8255291883173676D-08
a5 = -2.3264073779066090D-11
a6 = 1.8104813946953516D-14
a7 = -7.9168194925808462D-18
a8 =  1.4947170350415975D-21
X = a0 + a1*T**2 + a2*T**3 + a3*T**4 + a4*T**5 + a5*T**6 + a6*T**7 + a7*T**8 + a8*T**9
return
end subroutine X_NaCl_crit
!
!
! This subroutine calculates temperature as a function of composition along the critical curve; polynomial equation is a least
! squares regression analysis of data published by Bischoff and Pitzer (1989) and Anderko and Pitzer (1993).
subroutine T_NaCl_crit (T,X)
implicit none
double precision T,X,b0,b1,b2,b3,b4,b5,b6,b7,b8
b0 = 3.751762181713335D02
```

```
b1 = 1.117465777099634D01
b2 = -3.948964385446949D-02
b3 = 7.600000369734997D-03
b4 = -5.618098542440292D-04
b5 = 2.022438011392561D-05
b6 = -3.570251240149986D-07
b7 = 2.482912405538307D-09
T = b0 + b1*X + b2*X**4 + b3*X**5 + b4*X**6 + b5*X**7 + b6*X**8 + b7*X**9
return
end subroutine T_NaCl_crit
!
!
! This subroutine calculates density as a function of temperature along the critical curve in the H2O-NaCl system.  This equation
! is from Palliser and McKibbin (1998b)
subroutine RHO_NaCl_crit (RHO,T)
implicit none
double precision RHO,T,e0,e1,e2,e3
e0 = -1.35369D3
e1 = 1.09119D3
e2 = -8.80332D-5
e3 = -1.58302D4
RHO = (e0 + e1*T**0.1D0 + e2*T**2.0D0 + e3/(T - 320D0))/1000.0D0
return
end subroutine RHO_NaCl_crit
!
!
! This subroutine calculates pressure as a function of temperature and composition along the liquid-vapor surface in the H2O-NaCl
! system between 0 and 90 wt.% NaCl and between 80C to 900C; the equation is a stepwise regression model of data from Haas (1976),
! Bischoff and Pitzer (1989), and Anderko and Pitzer (1993)
subroutine H2ONACL_VPLV (P,T,X)
implicit none
double precision P,T,X,a0,a1,a2,a3,a4,a5,a6,a7,a8,a9,a10,a11,a12,a13,a14,a15,a16,a17,a18,a19,a20,a21,a22,a23,a24,a25,a26,a27,a28,a29
double precision a30,a31,a32,a33,a34,a35,a36,a37,a38,a39,a40,a41,a42,a43,a44,a45,a46,a47,a48,a49,a50,a51,a52,a53,a54,a55,a56,a57,a58
double precision a59,a60,a61,a62,a63,a64,a65,a66,a67,a68,a69,a70,a71,a72,a73,a74,a75,a76,a77,a78,a79,a80,a81,a82,a83,a84,a85,a86,a87
double precision a88,a89,a90,a91,a92,a93,a94,a95,a96,a97,a98,a99,a100,a101,a102,a103,a104,a105,a106,a107,a108,a109,a110,a111,a112
double precision a113,a114,a115,a116,a117,a118,a119,a120,a121,a122,a123,a124,a125,a126,a127,a128,a129,a130,a131,a132,a133,a134,a135
double precision a136,a137,a138,a139,a140,a141,a142,a143,a144
a0 = -1.546704103496906 6D04
a1 = -8.902862442663758 0D03
a2 = 5.067208603137917 2D02
a3 = -2.338488355549611 3D01
a4 = 8.223841134223788 3D-01
a5 = -2.109247482060982 7D-02
a6 = 3.789052429172987 1D-04
a7 = -4.356238522786384 2D-06
```

a8 = 2.3886557254327497D-08
a9 = -1.0571171965708819D00
a10 = 5.4705002228834813D-03
a11 = -1.279088473527900 1D-05
a12 = 1.4128876984820643D-08
a13 = -2.0472723742927036D-14
a14 = 2.5911534369932299D-17
a15 = -1.4321252030162424D-20
a16 = 3.1142114056307995D-24
a17 = 4.0597539354542910D01
a18 = -2.0268219235514300D00
a19 = 1.0407517713492526D-01
a20 = -4.2260368770752751D-03
a21 = 1.2273329666897414D-04
a22 = -2.5336085017669062D-06
a23 = 3.5844213189154493D-08
a24 = -2.8576390210593231D-10
a25 = 1.0557692420416255D-12
a26 = -4.8636236734360881D-15
a27 = 4.9616789616717290D-02
a28 = -5.2635259468764538D-03
a29 = 1.3076234005981744D-04
a30 = -7.5834128094795537D-08
a31 = 2.4424957426937338D-09
a32 = -4.9448128462557563D-11
a33 = 4.1120864763782769D-13
a34 = -8.4193142109788365D-16
a35 = 1.2564935749777674D-17
a36 = -6.0254577726395753D-04
a37 = 4.0929842201442640D-05
a38 = -1.2323637194154687D-06
a39 = 2.1857384562046434D-08
a40 = -2.9078649140659645D-10
a41 = 3.5324389466187402D-12
a42 = -3.6307920020528511D-18
a43 = -8.3888359636588165D-21
a44 = 1.5810763541821686D-06
a45 = -1.0252555671644502D-07
a46 = 2.7750217489240758D-09
a47 = -4.1278081421338645D-11
a48 = 4.3659297632904394D-13
a49 = -7.1802863122859497D-15
a50 = 1.9593710977132586D-17
a51 = 4.9768517385053834D-21
a52 = -1.7867187878149753D-09

a53 = 1.3717845039632832D-10
a54 = -3.2408501393865643D-12
a55 = 3.2264768571924560D-14
a56 = 3.8665481171869305D-18
a57 = -2.5278050992243331D-22
a58 = -1.3122276841961337D-24
a59 = -9.6683330856882442D-14
a60 = 2.0379277854150891D-15
a61 = -9.2344813291973269D-18
a62 = -3.8661176262039655D-19
a63 = 2.5033968447541801D-15
a64 = 2.0920210406254093D-17
a65 = -5.4126192360632430D-19
a66 = 2.2371518290429727D-22
a67 = 9.2816205337880962D-29
a68 = -3.0535349208723164D-18
a69 = 1.4443551835863471D-20
a70 = -7.2423307724618204D-28
a71 = -2.0506456034370369D-34
a72 = 6.3903615967675223D-37
a73 = 1.6076697477970711D-21
a74 = -7.6438663083904912D-24
a75 = -7.9123966626611658D-26
a76 = -3.2832568981984218D-25
a77 = 7.7948682794241322D-29
a78 = -5.3974863754984775D-31
a79 = 6.7862681977184883D-35
a80 = -6.0087903625393952D-42
a81 = 2.1057475263778586D05
a82 = -1.9152495139705657D06
a83 = 9.9300257561525702D06
a84 = -3.3590206975922488D07
a85 = 7.7026919430952162D07
a86 = -1.2084825619561587D08
a87 = 1.2796415012538801D08
a88 = -8.7569312885794640D07
a89 = 3.5009947737071708D07
a90 = -6.2127350875978656D06
a91 = 6.9317006467689590D09
a92 = -1.8103993213935684D12
a93 = 2.3741324736585181D14
a94 = -1.5529699989529190D16
a95 = 8.7181497953218216D19
a96 = -7.1316531664851367D21
a97 = 2.6019717838666694D23

a98 = -3.8082974580344852D24
a99 = 1.5897771298605198D08
a100 = -2.2532225616201539D09
a101 = 1.0520511536210300D10
a102 = -2.6469318805151897D10
a103 = 4.2359793942916862D10
a104 = -4.4591726424003448D10
a105 = 3.0216219038885242D10
a106 = -1.2060101508590298D10
a107 = 2.1629575099609647D09
a108 = -1.4118820072948032D11
a109 = 3.4301606939109186D11
a110 = -4.4275710041089368D11
a111 = 8.9722655546448413D11
a112 = -1.3422879816376135D12
a113 = 8.6330558829438196D11
a114 = -2.0807125401662372D11
a115 = 3.5684604183433430D13
a116 = -7.3655192149938422D13
a117 = 7.9960072511599250D13
a118 = -1.0525984900546364D14
a119 = 1.2374317040800288D14
a120 = -5.5680820329978148D13
a121 = 3.8323861195088569D12
a122 = -5.3824647732829300D15
a123 = 8.7033664945482380D15
a124 = -7.2737227870363900D15
a125 = 1.1654112109185122D15
a126 = 1.1952441044640902D15
a127 = 1.1005122025149556D14
a128 = 5.3592083133502573D17
a129 = -6.1790846769804083D17
a130 = 2.9974450894004864D17
a131 = -4.8696735705624320D16
a132 = -3.5819708926875619D19
a133 = 2.5294543561872359D19
a134 = -2.3747671225545779D18
a135 = 1.5608893731719246D21
a136 = -4.8389865745697230D20
a137 = -4.4213930212975772D20
a138 = -4.0421581146135743D22
a139 = 1.2058651089607837D22
a140 = 1.0114461428031647D22
a141 = 4.7561959638970802D23
a142 = 8.6487952445730311D22

```
a143 = -3.2919376453533884D23
a144 = -9.9284190347919552D-16
P = a0 + a1*X + a2*X**2 + a3*X**3 + a4*X**4 + a5*X**5 + a6*X**6 + a7*X**7 + a8*X**8 + a9*T**2 + a10*T**3 + a11*T**4 + a12*T**5 + &
  a13*T**7 + a14*T**8 + a15*T**9 + a16*T**10 + a17*T*X + a18*T*X**2 + a19*T*X**3 + a20*T*X**4 + a21*T*X**5 + a22*T*X**6 + &
  a23*T*X**7 + a24*T*X**8 + a25*T*X**9 + a26*T*X**10 + a27*T**2*X + a28*T**2*X**2 + a29*T**2*X**3 + a30*T**2*X**5 + a31*T**2*X**6 &
  + a32*T**2*X**7 + a33*T**2*X**8 + a34*T**2*X**9 + a35*T**2*X**10 + a36*T**3*X + a37*T**3*X**2 + a38*T**3*X**3 + a39*T**3*X**4 + &
  a40*T**3*X**5 + a41*T**3*X**6 + a42*T**3*X**9 + a43*T**3*X**10 + a44*T**4*X + a45*T**4*X**2 + a46*T**4*X**3 + a47*T**4*X**4 + &
  a48*T**4*X**5 + a49*T**4*X**6 + a50*T**4*X**7 + a51*T**4*X**9 + a52*T**5*X + a53*T**5*X**2 + a54*T**5*X**3 + a55*T**5*X**4 + &
  a56*T**5*X**6 + a57*T**5*X**8 + a58*T**5*X**9 + a59*T**6*X**2 + a60*T**6*X**3 + a61*T**6*X**4 + a62*T**6*X**5 + a63*T**7*X + &
  a64*T**7*X**2 + a65*T**7*X**3 + a66*T**7*X**5 + a67*T**7*X**8 + a68*T**8*X + a69*T**8*X**2 + a70*T**8*X**6 + a71*T**8*X**9 + &
  a72*T**8*X**10 + a73*T**9*X + a74*T**9*X**2 + a75*T**9*X**3 + a76*T**10*X + a77*T**10*X**3 + a78*T**10*X**4 + a79*T**10*X**6 + &
  a80*T**10*X**9 + a81*(X+1)**-1 + a82*(X+1)**-2 + a83*(X+1)**-3 + a84*(X+1)**-4 + a85*(X+1)**-5 + a86*(X+1)**-6 + a87*(X+1)**-7 &
  + a88*(X+1)**-8 + a89*(X+1)**-9 + a90*(X+1)**-10 + a91*T**-2 + a92*T**-3 + a93*T**-4 + a94*T**-5 + a95*T**-7 + a96*T**-8 + &
  a97*T**-9 + a98*T**-10 + a99*T**-1*(X+1)**-1 + a100*T**-1*(X+1)**-3 + a101*T**-1*(X+1)**-4 + a102*T**-1*(X+1)**-5 + &
  a103*T**-1*(X+1)**-6 + a104*T**-1*(X+1)**-7 + a105*T**-1*(X+1)**-8 + a106*T**-1*(X+1)**-9 + a107*T**-1*(X+1)**-10 + &
  a108*T**-2*(X+1)**-1 + a109*T**-2*(X+1)**-2 + a110*T**-2*(X+1)**-3 + a111*T**-2*(X+1)**-5 + a112*T**-2*(X+1)**-6 + &
  a113*T**-2*(X+1)**-7 + a114*T**-2*(X+1)**-8 + a115*T**-3*(X+1)**-1 + a116*T**-3*(X+1)**-2 + a117*T**-3*(X+1)**-3 + &
  a118*T**-3*(X+1)**-5 + a119*T**-3*(X+1)**-6 + a120*T**-3*(X+1)**-7 + a121*T**-3*(X+1)**-9 + a122*T**-4*(X+1)**-1 + &
  a123*T**-4*(X+1)**-2 + a124*T**-4*(X+1)**-3 + a125*T**-4*(X+1)**-4 + a126*T**-4*(X+1)**-5 + a127*T**-4*(X+1)**-10 + &
  a128*T**-5*(X+1)**-1 + a129*T**-5*(X+1)**-2 + a130*T**-5*(X+1)**-3 + a131*T**-5*(X+1)**-7 + a132*T**-6*(X+1)**-1 + &
  a133*T**-6*(X+1)**-2 + a134*T**-6*(X+1)**-4 + a135*T**-7*(X+1)**-1 + a136*T**-7*(X+1)**-2 + a137*T**-7*(X+1)**-3 + &
  a138*T**-8*(X+1)**-1 + a139*T**-8*(X+1)**-3 + a140*T**-8*(X+1)**-6 + a141*T**-9*(X+1)**-1 + a142*T**-9*(X+1)**-2 + &
  a143*T**-9*(X+1)**-10 + a144*exp(36.59-X**4)
return
end subroutine H2ONACL_VPLV
```

halite_liquidus.f90

```
! This subroutine calculates the slopes of isotherms through halite liquidi in X versus P space
subroutine slopes_xpisotherm (T,dXdP)
implicit none
double precision T,dXdP
dXdP = 2.63843078D-03 + 3.17527215D-05*T - 1.00879549D-07*T**2 + 2.50753145D-12*T**4 - 1.79046553D-14*T**5 + 6.02013429D-17*T**6 - &
  1.21987990D-19*T**7 + 1.50601773D-22*T**8 - 1.01941549D-25*T**9 + 2.86133271D-29*T**10
return
end subroutine slopes_xpisotherm
!
!
! This subroutine calculates the paths of isotherms through halite liquidi in X versus P space
subroutine xpisotherm (T,numloops,ptx)
implicit none
double precision T,Torig,P,wt_water,wt_NaCl,wt_KCl,wt_salt,R,m,ptx(2000,3)
```

```
integer numloops
P = 0.0D0
R=1.0D0
Torig = T
do while (P .lt. 600.0D0)
  numloops = numloops + 1
  call wt_halite_ternary(T,wt_water,wt_NaCl,wt_KCl,wt_salt,R)
  call P_NaCl_tp(P,T)
  m = 100.0D0/(-38.38D0 + 0.90D0*wt_NaCl - 0.0029D0*wt_NaCl**2)
  if (wt_NaCl.gt.100) then
        return
  elseif (Torig .lt. 431.6D0) then
        P = m*(Torig - T) + P
        T = T + 0.1D0
        ptx(numloops,1) = P
        ptx(numloops,2) = Torig
        ptx(numloops,3) = wt_NaCl
  elseif (Torig .gt. 431.7D0) then
        P = m*(Torig - T) + P
        T = T - 0.1D0
        ptx(numloops,1) = P
        ptx(numloops,2) = Torig
        ptx(numloops,3) = wt_NaCl
  else
        ptx(numloops,1) = P
        ptx(numloops,2) = T
        ptx(numloops,3) = wt_NaCL
        ptx(numloops+1,1) = 600.0D0
        ptx(numloops+1,2) = T
        ptx(numloops+1,3) = wt_NaCl
        P = 700.0D0
  endif
end do
return
end subroutine xpisotherm
!
!
! This subroutine is a regression model of experimental data of the isobars in Th L-V versus Tm halite space for fluid inclusions
! that homogenize by halite disappearance.  It may be used to estimate the minimum trapping pressure of fluid inclusions that
! homogenize by halite disappearance.
subroutine ThTmisobars (P,Th,Tm)
implicit none
double precision P,Th,Tm
P = -1.81686045D5 - 2.99745046D2*Th + 2.69412137D-1*Th**2 - 1.70660033D2*Tm + 9.21003065D-2*Tm**2 + 6.59084234D-1*Th*Tm&
  - 4.76501015D-4*Th*Tm**2 - 7.93265819D-4*Th**2*Tm + 6.48940949D-7*Th**2*Tm**2 - 1.46975329D4*Dlog(Tm)&
```

```
  + 5.37493440D4*Dlog(Th + Tm)
return
end subroutine ThTmisobars
!
!
! This subroutine will calculate isobars in Th L-V versus Tm halite space using the regression model developed from experimental
! data for fluid inclusions that homogenize by halite disappearance.
subroutine calc_isobar (P_calc,Th_low,Th_high,Tm_low,Tm_high,ThTm,count)
implicit none
double precision Ptemp,P_calc,Th_low,Th_high,Tm_low,Tm_high,ThTm(1000,3),i,j
integer count
count=0
Ptemp=0.0D0
do i = Th_low,Th_high,0.1D0
  do j = Tm_low,Tm_high,0.1D0
    call ThTmisobars(Ptemp,i,j)
    if(abs(Ptemp-P_calc).le.0.01D0 .and. i.lt.j) then
          count=count+1
          ThTm(count,1)=Ptemp
          ThTm(count,2)=i
          ThTm(count,3)=j
    endif
  end do
end do
return
end subroutine calc_isobar
!
!
! Given an input pressure and temperature, this subroutine calculates the composition of the halite liquidus that passes through
! the input P-T point.
subroutine liquiduspredict (P,T,X)
implicit none
double precision P,T,X,wt_water,wt_NaCl,wt_KCl,wt_salt,R,P1,T1,dXdP
P1=P
T1=T
R=1.0D0
call wt_halite_ternary(T,wt_water,wt_NaCl,wt_KCl,wt_salt,R)
call P_NaCl_tp(P,T)
call slopes_xpisotherm(T,dXdP)
X = dXdP*(P1-P)+wt_NaCl
P = P1
T = T1
return
end subroutine liquiduspredict
```

pvtnaclh2o1kb.f90

```
! original code by Robert J. Bodnar, modified by Stephen P. Becker
! given an input temperature, pressure (between 100 and 500 MPa), and composition, this subroutine will calculate the density
! of H2O-NaCl solutions in the one phase field
subroutine point (tdegc, pmpa, wtpct, RHO)
implicit none
double precision tdegc,pmpa,wtpct,a1,a2,a3,a4,a5,a6,a7,a8,a9,a10,a11,a12,a13,a14,a15,a16,a17,a18,a19,a20,a21,a22,a23,a24,a25,a26
double precision a27,a28,a29,a30,a31,a32,a33,a34,a35,a36,a37,a38,a39,a40,a41,a42,a43,a44,a45,a46,a47,a48,a49,a50,a51,a52,a53,a54,a55
double precision a56,a57,a58,a59,a60,a61,a62,a63,a64,xmwh2o,xmwnac,p,p1,p2,p3,t1,t2,t3,xmfrac,x,x1,x2,x3,u1,u2,u,vmm,xh2o,xmmwt,sv
double precision rho
integer icor,quit
A1=2.75947593D0
A2=0.28650796D0
A3=-0.36237767D0
A4=0.60946727D0
A5=-0.04692496D0
A6=0.02742480D0
A7=-0.00232088D0
A8=0.26256810D0
A9=-0.00303048D0
A10=-0.04833583D0
A11=0.41349416D0
A12=-0.10846906D0
A13=0.01137573D0
A14=-0.86695835D0
A15=0.30628044D0
A16=-0.02636009D0
A17=0.33150762D0
A18=-0.12080244D0
A19=0.01066505D0
A20=-1.28677581D0
A21=0.36815735D0
A22=0.17535112D0
A23=3.79162211D0
A24=-1.91089093D0
A25=-0.20405928D0
A26=-2.69527171D0
A27=1.50663086D0
A28=0.07221570D0
A29=0.48103209D0
A30=-0.18501497D0
```

```
A31=0.01380743D0
A32=-1.04248226D0
A33=0.41996651D0
A34=-0.03084556D0
A35=0.61443067D0
A36=-0.26174124D0
A37=0.01944934D0
A38=-1.53625679D0
A39=0.54683773D0
A40=-0.04870083D0
A41=3.54591673D0
A42=-1.40911463D0
A43=0.11629529D0
A44=-1.41632449D0
A45=0.53639001D0
A46=-0.04547063D0
A47=2.75937879D0
A48=-1.12001081D0
A49=0.09413710D0
A50=-6.01838044D0
A51=2.41621380D0
A52=-0.20058972D0
A53=2.49279025D0
A54=-0.89656506D0
A55=0.07735061D0
A56=-1.59237589D0
A57=0.67975497D0
A58=-0.05726004D0
A59=3.25270091D0
A60=-1.31412558D0
A61=0.11208802D0
A62=-1.35729003D0
A63=0.48236162D0
A64=-0.04349736D0
XMWH2O=18.0152D0
XMWNAC=58.4428D0
P=PMPA/100.0D0
P1=1.0D0/P
P2=(1.0D0/P)**2
P3=(1.0D0/P)**3
T1=(TDEGC/100.0D0)
T2=(TDEGC/100.0D0)**2
T3=(TDEGC/100.0D0)**3
XMFRAC=(WTPCT/XMWNAC)/((WTPCT/XMWNAC)+((100.0D0-WTPCT)/XMWH2O))
X=XMFRAC+0.01D0
```

```
X1=DSQRT(X)
X2=(DSQRT(X))**2
X3=(DSQRT(X))**3
U1=A1+(A2*X1)+(A3*X2)+(A4*X3)+(A5*T1)+(A6*T2)+(A7*T3)+(A8*P1)+(A9*P2)+(A10*P3)+(A11*T1*P1)+(A12*T2*P1)+(A13*T3*P1)+(A14*T1*P2)+(&
  A15*T2*P2)+(A16*T3*P2)+(A17*T1*P3)+(A18*T2*P3)+(A19*T3*P3)+(A20*P1*X1)+(A21*P2*X1)+(A22*P3*X1)+(A23*P1*X2)+(A24*P2*X2)+(A25*&
  P3*X2)+(A26*P1*X3)+(A27*P2*X3)+(A28*P3*X3)+(A29*T1*X1)+(A30*T2*X1)+(A31*T3*X1)+(A32*T1*X2)+(A33*T2*X2)+(A34*T3*X2)+(A35*T1*X3&
  )+(A36*T2*X3)+(A37*T3*X3)+(A38*T1*P1*X1)+(A39*T2*P1*X1)+(A40*T3*P1*X1)+(A41*T1*P2*X1)+(A42*T2*P2*X1)+(A43*T3*P2*X1)+(A44*T1*&
  P3*X1)+(A45*T2*P3*X1)+(A46*T3*P3*X1)+(A47*T1*P1*X2)
U2=(A48*T2*P1*X2)+(A49*T3*P1*X2)+(A50*T1*P2*X2)+(A51*T2*P2*X2)+(A52*T3*P2*X2)+(A53*T1*P3*X2)+(A54*T2*P3*X2)+(A55*T3*P3*X2)+(A56*&
  T1*P1*X3)+(A57*T2*P1*X3)+(A58*T3*P1*X3)+(A59*T1*P2*X3)+(A60*T2*P2*X3)+(A61*T3*P2*X3)+(A62*T1*P3*X3)+(A63*T2*P3*X3)+(A64*T3*P3&
  *X3)
U=U1+U2
VMM=(DEXP(U))-1.0D0
XH2O=1.0D0-XMFRAC
XMMWT=(XMFRAC*XMWNAC)+(XH2O*XMWH2O)
SV=VMM/XMMWT
RHO=1.0D0/SV
return
end subroutine point
!
!
! given a starting PVTX point in the one phase field (e.g. output from subroutine "point"), this subroutine will extrapolate an isocore
! up to 500 MPa or 1000C, whichever comes first
subroutine isocor (tdegc,pmpa,wtpct,RHO,numloops,ptxd)
implicit none
double precision tdegc,pmpa,wtpct,a1,a2,a3,a4,a5,a6,a7,a8,a9,a10,a11,a12,a13,a14,a15,a16,a17,a18,a19,a20,a21,a22,a23,a24,a25,a26
double precision a27,a28,a29,a30,a31,a32,a33,a34,a35,a36,a37,a38,a39,a40,a41,a42,a43,a44,a45,a46,a47,a48,a49,a50,a51,a52,a53,a54,a55
double precision a56,a57,a58,a59,a60,a61,a62,a63,a64,xmwh2o,xmwnac,p,p1,p2,p3,t1,t2,t3,tmax,tmin,tnew,xmfrac,x,x1,x2,x3,u1,u2,u,vmm
double precision xh2o,xmmwt,sv,rho,rhonew,diff,ptxd(1000,4)
integer niter, numloops, j
logical iterate
ptxd(1,1) = pmpa
ptxd(1,2) = tdegc
ptxd(1,3) = wtpct
ptxd(1,4) = RHO
A1=2.75947593D0
A2=0.28650796D0
A3=-0.36237767D0
A4=0.60946727D0
A5=-0.04692496D0
A6=0.02742480D0
A7=-0.00232088D0
A8=0.26256810D0
A9=-0.00303048D0
A10=-0.04833583D0
```

```
A11=0.41349416D0
A12=-0.10846906D0
A13=0.01137573D0
A14=-0.86695835D0
A15=0.30628044D0
A16=-0.02636009D0
A17=0.33150762D0
A18=-0.12080244D0
A19=0.01066505D0
A20=-1.28677581D0
A21=0.36815735D0
A22=0.17535112D0
A23=3.79162211D0
A24=-1.91089093D0
A25=-0.20405928D0
A26=-2.69527171D0
A27=1.50663086D0
A28=0.07221570D0
A29=0.48103209D0
A30=-0.18501497D0
A31=0.01380743D0
A32=-1.04248226D0
A33=0.41996651D0
A34=-0.03084556D0
A35=0.61443067D0
A36=-0.26174124D0
A37=0.01944934D0
A38=-1.53625679D0
A39=0.54683773D0
A40=-0.04870083D0
A41=3.54591673D0
A42=-1.40911463D0
A43=0.11629529D0
A44=-1.41632449D0
A45=0.53639001D0
A46=-0.04547063D0
A47=2.75937879D0
A48=-1.12001081D0
A49=0.09413710D0
A50=-6.01838044D0
A51=2.41621380D0
A52=-0.20058972D0
A53=2.49279025D0
A54=-0.89656506D0
A55=0.07735061D0
```

```
A56=-1.59237589D0
A57=0.67975497D0
A58=-0.05726004D0
A59=3.25270091D0
A60=-1.31412558D0
A61=0.11208802D0
A62=-1.35729003D0
A63=0.48236162D0
A64=-0.04349736D0
XMWH2O=18.0152D0
XMWNAC=58.4428D0
do while (pmpa.lt.500.0D0)
  PMPA=PMPA+10.0D0
  numloops = numloops + 1
  P=PMPA/100.0D0
  P1=1.0D0/P
  P2=(1.0D0/P)**2
  P3=(1.0D0/P)**3
  TMAX=1000.0D0
  TMIN=TDEGC
  TNEW=TDEGC+((1000.0D0-TDEGC)/2.0D0)
  if(TNEW.GE.999.9) then
    return
  endif
  NITER=0
  iterate = .true.
  do while (iterate .eqv. .true.)
    NITER=NITER+1
    IF(NITER.GT.100) then
      return
    endif
    T1=(TNEW/100.0D0)
    T2=(TNEW/100.0D0)**2
    T3=(TNEW/100.0D0)**3
    XMFRAC=(WTPCT/XMWNAC)/((WTPCT/XMWNAC)+((100.0D0-WTPCT)/XMWH2O))
    X=XMFRAC+0.01D0
    X1=DSQRT(X)
    X2=(DSQRT(X))**2
    X3=(DSQRT(X))**3
    U1=A1+(A2*X1)+(A3*X2)+(A4*X3)+(A5*T1)+(A6*T2)+(A7*T3)+(A8*P1)+(A9*P2)+(A10*P3)+(A11*T1*P1)+(A12*T2*P1)+(A13*T3*P1)+(A14*T1*P2&
      )+(A15*T2*P2)+(A16*T3*P2)+(A17*T1*P3)+(A18*T2*P3)+(A19*T3*P3)+(A20*P1*X1)+(A21*P2*X1)+(A22*P3*X1)+(A23*P1*X2)+(A24*P2*X2)+&
      (A25*P3*X2)+(A26*P1*X3)+(A27*P2*X3)+(A28*P3*X3)+(A29*T1*X1)+(A30*T2*X1)+(A31*T3*X1)+(A32*T1*X2)+(A33*T2*X2)+(A34*T3*X2)+(&
      A35*T1*X3)+(A36*T2*X3)+(A37*T3*X3)+(A38*T1*P1*X1)+(A39*T2*P1*X1)+(A40*T3*P1*X1)+(A41*T1*P2*X1)+(A42*T2*P2*X1)+(A43*T3*P2*&
      X1)+(A44*T1*P3*X1)+(A45*T2*P3*X1)+(A46*T3*P3*X1)+(A47*T1*P1*X2)
    U2=(A48*T2*P1*X2)+(A49*T3*P1*X2)+(A50*T1*P2*X2)+(A51*T2*P2*X2)+(A52*T3*P2*X2)+(A53*T1*P3*X2)+(A54*T2*P3*X2)+(A55*T3*P3*X2)+(&
```

```
      A56*T1*P1*X3)+(A57*T2*P1*X3)+(A58*T3*P1*X3)+(A59*T1*P2*X3)+(A60*T2*P2*X3)+(A61*T3*P2*X3)+(A62*T1*P3*X3)+(A63*T2*P3*X3)+(&
      A64*T3*P3*X3)
    U=U1+U2
    VMM=(DEXP(U))-1.0D0
    XH2O=1.0D0-XMFRAC
    XMMWT=(XMFRAC*XMWNAC)+(XH2O*XMWH2O)
    SV=VMM/XMMWT
    RHONEW=1.0D0/SV
    DIFF=RHO-RHONEW
    if(DIFF.GT.0.001) then
      TMAX=TNEW
      TNEW=TNEW-((TMAX-TMIN)/2.0D0)
      iterate = .true.
    elseif(DIFF.LT.-0.001) then
      TMIN=TNEW
      TNEW=TNEW+((TMAX-TMIN)/2.0D0)
      iterate = .true.
    else
      ptxd(numloops+1,1) = PMPA
      ptxd(numloops+1,2) = TNEW
            ptxd(numloops+1,3) = WTPCT
            ptxd(numloops+1,4) = RHONEW
      iterate = .false.
    endif
  end do
end do
return
end subroutine isocor
```

H2O_NaCl_model.f90

```
!This subroutine will predict the homogenization temperature for fluid inclusions trapped at PTX conditions in the one phase field
!that would homogenize by vapor bubble disappearance up to ~40wt% NaCl, and will predict the composition of coexisting phases in the two
!phase field up to 900C.
subroutine predict_Th (Pt,Tt,X_bulk,X_brine,X_vapor,Th,VAPOR_PLUS_HALITE)
implicit none
double precision Pt,Tt,X,Plv,Tlv,dPdT,Th,P_temp,X_bulk,X_brine,X_vapor,X_temp1,X_temp2,wt_water,wt_KCl,wt_salt,R,P_threephase,minPt
double precision VAPOR_PLUS_HALITE
Plv = 0.0D0
Tlv = 80.0D0
dPdT = 0.0D0
call P_NaCl_tp(P_threephase,Tt)
```

```
if (Pt .lt. P_threephase+0.2D0) then
  VAPOR_PLUS_HALITE = 1.0D0
  return
endif
if (Tt .gt. 500.0D0) then
  minPt = 40.0D0
  if (Pt .lt. minPt) then
    Pt = minPt
  endif
endif
call H2ONACL_VPLV(P_temp,Tt,X_bulk)
if ((Pt-P_temp).gt.1.0D0) then
  !one phase field
  do while (abs(((Pt-Plv)/(Tt-Tlv)) - dPdT) .gt. 0.01D0)
    call H2ONACL_VPLV(Plv,Tlv,X_bulk)
    call dPdT_isoTh (Tlv,X_bulk,dPdT)
    Tlv = Tlv + 0.01D0
  end do
  Th = Tlv
else if (abs(Pt-P_temp).lt.1.0D0) then
  !two phase field, along l-v curve of bulk composition
  Th = Tt
else if ((Pt-P_temp).lt.-1.0D0) then
  !two phase field, coexisting higher salinity brine and lower salinity vapor
  Th = Tt
  R=1.0D0
  call wt_halite_ternary(Th,wt_water,X_temp1,wt_KCl,wt_salt,R)
  P_temp = 0.0D0
  do while (abs(Pt-P_temp).gt.0.10D0)
    call H2ONACL_VPLV (P_temp,Th,X_temp1)
    X_temp1=X_temp1-0.001D0
  end do
  P_temp = 0.0D0
  call X_NaCl_crit(Th,X_temp2)
  do while (abs(Pt-P_temp).gt.0.10D0)
   call H2ONACL_VPLV (P_temp,Th,X_temp2)
   X_temp2=X_temp2-0.001D0
  end do
  if (X_bulk.eq.0.0D0) then
    X_brine = 0.0D0
  else
    X_brine = X_temp1
  end if
  if (X_temp2 .lt. 0.0D0 .or. Th .lt. 380.0D0) then
    X_vapor = 0.0D0
```

```
  else
    X_vapor = X_temp2
  endif
endif
return
end subroutine predict_Th
!
!
! Given a bulk density and composition, this subroutine will calculate the relative percentages of halite, liquid, and
! vapor within a fluid inclusion at 25C.
subroutine phasrat (X_NACL_BULK,RHO_BULK,VPERCENT_HALITE,VPERCENT_SOL,VPERCENT_BUBBLE)
implicit none
double precision Pt,Tt,X_NACL_BULK,volume,RHO_BULK,MASS_BULK,X_H2O_BULK,MASS_H2O_BULK,MASS_NACL_BULK,MASS_NACL_SOL_TCALC
double precision VPERCENT_HALITE,VPERCENT_SOL,VPERCENT_BUBBLE,wt_water,wt_NaCl_TCALC,wt_KCl,wt_salt,R,RHO_UNDERSAT_LIQ_RT
double precision MASS_NACL_HAL_TCALC,TCALC
TCALC=25.0D0
volume = 1000.0D0
MASS_BULK = RHO_BULK*volume
X_H2O_BULK = 1.0D0 - (X_NACL_BULK/100.0D0)
MASS_H2O_BULK = X_H2O_BULK*MASS_BULK
MASS_NACL_BULK = (X_NACL_BULK/100.0D0)*MASS_BULK
if(X_NACL_BULK.ge.26.4) then
  !use water-Nacl system
  R = 1.0D0
  call wt_halite_ternary(TCALC,wt_water,wt_NaCl_TCALC,wt_KCl,wt_salt,R)
  MASS_NACL_SOL_TCALC = (wt_NaCl_TCALC/100.0D0)*MASS_H2O_BULK/(1.0D0-(wt_NaCl_TCALC/100.0D0))
  MASS_NACL_HAL_TCALC = MASS_NACL_BULK - MASS_NACL_SOL_TCALC
  VPERCENT_HALITE = 100.0D0*((MASS_NACL_HAL_TCALC/2.163D0)/1000.0D0)
  VPERCENT_SOL = 100.0D0*((MASS_NACL_SOL_TCALC + MASS_H2O_BULK)/1.20D0)/1000.0D0
  VPERCENT_BUBBLE = 100 - (VPERCENT_HALITE + VPERCENT_SOL)
else
  call rho_undersat_liq_25C(RHO_UNDERSAT_LIQ_RT,X_NACL_BULK)
  VPERCENT_HALITE = 0.0D0
  VPERCENT_BUBBLE = 100.0D0*(RHO_UNDERSAT_LIQ_RT - RHO_BULK)/RHO_UNDERSAT_LIQ_RT
  VPERCENT_SOL = 100.0D0 - VPERCENT_BUBBLE
endif
return
end subroutine phasrat
!
!
!this subroutine calculates pressure based on hydrostatic and lithostatic gradients of 10MPa/Km and 30MPa/Km,
!respectively; input is total depth and brittle-ductile transition depth
subroutine litho_hydro_P (depth_total,depth_BD,P)
implicit none
double precision depth_total,depth_BD,P,dPdZ_litho,dPdZ_hydro
```

```
dPdZ_hydro = 10.0D0
dPdZ_litho = 30.0D0
if (depth_total.le.depth_BD) then
        P = dPdZ_hydro*depth_total
else
        P = depth_BD*dPdZ_hydro + (depth_total-depth_BD)*dPdZ_litho
endif
return
end subroutine litho_hydro_P
```

Appendix C: R Code

Listed below are a series of R functions used to manipulate and reduce data, and to calculate phase equilibria of H_2O-NaCl fluids in Chapters 2 and 3. While R handles all of the manipulation and displaying of data, most of the intensive calculations are handled by a shared library produced from the FORTRAN90 code listed in Appendix B. While certain of these functions were specifically developed for the purpose of the research presented in Chapters 2 and 3, also included are other useful functions for calculating phase relationships that might be of interest to many fluid inclusionists.

saltfunctions.R

```
# This function calculates the final ice melting temperature in the water-NaCl-KCl system given wt% total salt, X, and the ratio of NaCl to
# NaCl+KCl, R
FPD <- function(X, R) {
  XT <- NULL
    for (i in R) {
          c <- 0.4597 + 0.1440*i
          e <- 2.227e-04 + 1.999e-04*i + 4.633e-05*i^2 + 1.123e-04*i^3
          XT <- data.frame(cbind(XT,T=-(0.000 + c*X + e*X^3),X=X,R=i))
    }
}
#
#
# Given a final ice-melting temperature and the ration of Nacl to NaCl+KCl, this function calculates weight percent salt in the
# water-NaCl-KCl system over the range of -22.9 to 0.01C
ice_ternary <- function(T, R) {
  dyn.load("fortran/water_halite_equilibria.so")
  tdata <- NULL
  for (i in T) {
    for (j in R) {
          tdata <-
rbind(tdata,data.frame(.Fortran("wt_ice_ternary",T=as.double(i),wt_water=as.double(1),wt_NaCl=as.double(1),wt_KCl=as.double(1),wt_salt=as.double(1),R=as
.double(j))))
    }
  }
}
#
```

```
#
# This function uses the equation of Sterner et al., 1988 to calculate X as a function of T for halite in the water-NaCl-KCl ternary
# over the range of -2.3<=T<=801C
halite_ternary <- function(T, R) {
  dyn.load("fortran/water_halite_equilibria.so")
  tdata <- NULL
  for (i in T) {
    for (j in R) {
          tdata <-
rbind(tdata,data.frame(.Fortran("wt_halite_ternary",T=as.double(i),wt_water=as.double(1),wt_NaCl=as.double(1),wt_KCl=as.double(1),wt_salt=as.double(1),R=
as.double(j))))
    }
  }
}
#
#
# This function uses the equation of Sterner et al., 1988 to calculate X as a function of T for sylvite in the water-NaCl-KCl ternary
# over the range of -22.9<=T<=770C
sylvite_ternary <- function(T,R) {
  dyn.load("fortran/water_halite_equilibria.so")
  tdata <- NULL
  for (i in T) {
    for (j in R) {
          tdata <-
rbind(tdata,data.frame(.Fortran("wt_sylvite_ternary",T=as.double(i),wt_water=as.double(1),wt_NaCl=as.double(1),wt_KCl=as.double(1),wt_salt=as.double(1),R
=as.double(j))))
    }
  }
}
#
#
# This function uses the equation of Sterner et al., 1988 to calculate X as a function of T for hydrohalite in the water-NaCl-KCl ternary
# over the range of -22.9 <=T<=0.1C
hydrohalite_ternary <- function(T,R) {
  dyn.load("fortran/water_halite_equilibria.so")
  tdata <- NULL
  for (i in T) {
    for (j in R) {
```

```
            tdata <-
rbind(tdata,data.frame(.Fortran("wt_hydrohalite_ternary",T=as.double(i),wt_water=as.double(1),wt_NaCl=as.double(1),wt_KCl=as.double(1),wt_salt=as.double
(1),R=as.double(j))))
      }
   }
}
#
#
# This function calculates vapor pressure along the vapor-saturated halite solubility curve as a function of temperature.
P_NaCl_tp <- function(T) {
   dyn.load("fortran/water_halite_equilibria.so")
   tdata <- NULL
   for (i in T) {
      tdata <- rbind(tdata,data.frame(.Fortran("P_NaCl_tp",P=as.double(1),T=as.double(i))))
   }
}
#
#
# This function calculates temperature along the vapor-saturate halite solubility curve as a function of composition.
T_NaCl_tp <- function(X) {
   dyn.load("fortran/water_halite_equilibria.so")
   Temp <- NULL
   for (i in X) {
            Temp <- rbind(Temp,data.frame(T=.Fortran("T_NaCL_tp",T=as.double(1),X=as.double(i))$T,X=i))
   }
}
#
#
# Given some composition X, this function calculates the equation of a halite liquidus in the P-T projection of the water-NaCl system
liquidus <- function(X) {
   dyn.load("fortran/water_halite_equilibria.so")
   T1 <- .Fortran("T_NaCl_tp",T=as.double(1),X=as.double(X))$T
   P1 <- .Fortran("P_NaCl_tp",P=as.double(1),T=as.double(T1))$P
   liq <- NULL
   m <- 100/(-38.38+0.90*X-0.0029*X^2)
   for (P in seq(P1, 500, by=50)) {
      T <- (P-P1)/m + T1
      liq<-rbind(liq,data.frame(P=P,T=T))
   }
}
```

```
#
#
# This function plots isotherms through halite liquidi in P versus X space up to 500 MPa
plot_isotherm_PX <- function(Temp) {
  options(digits=12)
  dyn.load("fortran/water_halite_equilibria.so")
  loops <- 0
  for (i in Temp) {
    loops <- loops + 1
    tdata <- data.frame(.Fortran("xpisotherm",T=as.double(i),numloops=as.integer(0),ptx=matrix(0,2000,3)))
    plotdata <- data.frame(P=as.double(tdata$ptx.1[1:tdata$numloops[1]]),X=as.double(tdata$ptx.3[1:tdata$numloops[1]]))
    plot(plotdata,xlim=c(0,500),ylim=c(20,100),type="l",xlab="Pressure (MPa)",ylab="Salinity (wt%)",col=loops)
    par(new=T)
  }
  par(new=F)
}
#
#
# This function calculates the slopes of isotherms through halite liquidi in P versus X space
isotherm_slopes <- function(T) {
  options(digits=12)
  dyn.load("fortran/water_halite_equilibria.so")
  sdata <- NULL
  for (i in T) {
    tdata <- data.frame(.Fortran("xpisotherm",T=as.double(i),numloops=as.integer(0),ptx=matrix(0,2000,3)))
    isothermdata <- data.frame(P=as.double(tdata$ptx.1[1:tdata$numloops[1]]),X=as.double(tdata$ptx.3[1:tdata$numloops[1]]))
    coefs <- lm(X ~ P, data=isothermdata)$coef
    sdata <- rbind(sdata,cbind(T=i,dXdT=as.matrix(coefs)[2,1]))
  }
}
#
#
# This function calculates the compositions of halite saturated liquids along an isobar between 0 and 800C
isobar <- function(P) {
  dyn.load("fortran/water_halite_equilibria.so")
  tdata <- NULL
  Porig <- P
  for (i in seq(0,800,by=50)) {
        tdata <- rbind(tdata,data.frame(.Fortran("liquiduspredict",P=Porig,T=i,X=1)))
  }
```

```
}
#
#
# Given Th L-V and Tm halite for a fluid inclusion that homogenizes by halite disappearance, this function calculates the minimum
# trapping pressure and the bulk composition of the inclusion.
halitedissol_predictPX <- function(Th, Tm) {
  dyn.load("fortran/water_halite_equilibria.so")
  answer <- NULL
  data <- data.frame(Th=Th,Tm=Tm)
  for (i in 1:length(data$Th)) {
    if(data[i,1] >= data[i,2]) {
          dummy <- NULL
    }
    else {
          one <- data.frame(.Fortran("ThTmisobars",P=as.double(1),Th=as.double(data[i,1]),Tm=as.double(data[i,2])))
          two <- data.frame(.Fortran("liquiduspredict",P=as.double(one$P),T=as.double(data[i,2]),X=as.double(1)))
          answer <- rbind(answer,data.frame(Th=data[i,1],Tm=data[i,2],P=one$P,X=two$X))
    }
  }
}
#
#
# Given an array of homogenization data (column 1 = sample designation, column 2 = Th L-V, column 3 = Tm halite), this function returns
# an array with the minimum trapping pressure and bulk composition for each input value (column 1 = sample designation, column 2 =
# Th L-V, column 3 = Tm halite, column 4 = P, column 5 = X)
halitedissol_predictPX2 <- function(data) {
  dyn.load("fortran/water_halite_equilibria.so")
  answer <- NULL
  for (i in 1:length(data$Th)) {
    if(data[i,2] >= data[i,3]) {
          dummy <- NULL
    }
    else {
          one <- data.frame(.Fortran("ThTmisobars",P=as.double(1),Th=as.double(data[i,2]),Tm=as.double(data[i,3])))
          two <- data.frame(.Fortran("liquiduspredict",P=as.double(one$P),T=as.double(data[i,3]),X=as.double(1)))
          answer <- rbind(answer,data.frame(Label=data[i,1],Th=data[i,2],Tm=data[i,3],P=one$P,X=two$X))
    }
  }
}
#
```

```
#
# This function plots the three-phase curve and halite liquidi in the water-NaCl system given input composition(s).  Tr and Pr
# are temperature and pressure ranges of the format "c(lowerlimit,upperlimit)"
plothaliteliquidi <- function(X,Tr,Pr) {
  tpcurve <- P_NaCl_tp(0:800)
  par(mar=c(5,5,1,1),ps=18)
  plot(tpcurve$T,tpcurve$P,xlim=Tr,ylim=Pr,type="l",xlab=expression("Temperature ("*degree*"C)"),ylab="Pressure (MPa)",lwd=4)
  for (i in X) {
    temp1 <- liquidus(i)
        points(temp1$T,temp1$P,type="l",lwd=2)
  }
}
#
#
# This function uses a Fortran subroutine to calculate the P-T projection of a liquid-vapor curve for
# some composition X in the water-NaCl system, up to 900C.
lvcurve <- function(X, T) {
  dyn.load("fortran/water_halite_equilibria.so")
  tdata <- NULL
  for (i in T) {
    tdata <- rbind(tdata,data.frame(.Fortran("H2ONACL_VPLV",P=as.double(1),T=as.double(i),X=as.double(X))))
  }
}
#
#
# This function uses the loess function to predict a pressure at any temperature and composition on the L-V surface
# for the water-NaCl system using data from Haas, Bischoff and Pitzer, and Anderko and Pitzer.  Input is
# temperature in degrees C and composition in weight% NaCl.
LVpred <- function(T1, X1) {
  tdata <- NULL
  # Read in the data from an input file
  ptxdata <- read.csv(file="../../Documents/porphyry\ model/PVTXdata.csv",head=TRUE)
  # Use data from the input file to create a loess object for the water-NaCl system
  P.loess <- loess(P ~ T + X, span=0.058, data.frame(P=ptxdata$P, T=ptxdata$T, X=ptxdata$X))
  # Use the loess object to predict a pressure with the T and X passed to this function
  for (i in T1) {
    tdata <- rbind(tdata,data.frame(P=predict(P.loess, data.frame(T=i,X=X1)), T=i))
  }
}
#
```

```
#
# This function uses a Fortran shared library to calculate an isocore (line of constant volume or density)
# for any given PTX condition.  Input is temperature in degrees C, pressure in Megapascals, and composition
# in weight% NaCl.
isocore <- function(tdegc, pmpa, wtpct) {
  # Load the fortran shared library.  See pvtnaclh2o1kb.f90 for more information.
  dyn.load("fortran/water_halite_equilibria.so")
  # Set the number of significant figures.
  options(digits=12)
  # Use the "point" subroutine from the pvtnaclh2o1kb Fortran shared library to calculate the density of the
  # fluid at the given PTX condition.
  temp <- data.frame(.Fortran("point", tdegc=as.double(tdegc), pmpa=as.double(pmpa), wtpct=as.double(wtpct), RHO=as.double(1)))
  # Use the "isocor" subroutine from the pvtnaclh2o1kb Fortran shared library to calculate an isocore for
  # the density calculated from the "point" subroutine up to 500Mpa or 1000C, whichever comes first.
  temp2 <- data.frame(.Fortran("isocor", tdegc=temp$tdegc, pmpa=temp$pmpa, wtpct=temp$wtpct, RHO=temp$RHO, numloops=as.integer(0),
ptxd=matrix(0,1000,4)))
  # The next few lines take the relevant information from the temp2 object (which contains the output from the "isocor"
  # subroutine), and combine it into a readable and useful object.
  P <- as.double(temp2$ptxd.1[1:temp2$numloops[1]])
  T <- as.double(temp2$ptxd.2[1:temp2$numloops[1]])
  X <- as.double(temp2$ptxd.3[1:temp2$numloops[1]])
  RHO <- as.double(temp2$ptxd.4[1:temp2$numloops[1]])
  PTXD <- cbind(data.frame(P,T,X,RHO))
  # Print the output of our calculations.
  print(PTXD)
  # Calculate the equation for the isocore in P-T space
  #lm(I(P*10.0) ~ T)
  # Print a summary of the isocore linear model object
  #summary(isocor)
}
```

porphyry_model.R

```
# Given a PTX point in the H2O-NaCl system, this function calculates the phase stability and fluid inclusion characteristics for inclusions
# trapped at the input conditions.
Predict_flinc_pressure <- function(P,T,X) {
  dyn.load("fortran/water_halite_equilibria.so")
  phaseratios <- NULL
```

```
  data<-read.csv(file="../../Documents/porphyry\ model/PVTXdata.csv",head=TRUE)
  RHO.loess <- loess(RHO ~ T + X, span=0.059, data.frame(RHO=data$RHO,T=data$T,X=data$X))
  data1 <-
data.frame(.Fortran("predict_Th",Pt=as.double(P),Tt=as.double(T),X_bulk=as.double(X),X_brine=as.double(0),X_vapor=as.double(0),Th=as.double(0),VAPOR
_PLUS_HALITE=as.double(0)))
  print(data1)

  if (data1$VAPOR_PLUS_HALITE == 1) {
    print("two-phase field: vapor + halite")
  }
  else if (data1$VAPOR_PLUS_HALITE == 0) {
    if (data1$X_brine < data1$X_bulk) {
        RHO <- predict(RHO.loess,data.frame(T=data1$Th,X=data1$X_bulk))
        T_CRIT <- data.frame(.Fortran("T_NaCl_crit",T=as.double(0),X=as.double(X)))$T
        RHO_CRIT <- data.frame(.Fortran("RHO_NaCl_crit",RHO=as.double(0),T=as.double(T_CRIT)))$RHO

        phaseratios <-
data.frame(.Fortran("phasrat",X_NACL_BULK=as.double(data1$X_bulk),RHO_BULK=as.double(RHO),VPERCENT_HALITE=as.double(0),VPERCENT_S
OL=as.double(0),VPERCENT_BUBBLE=as.double(0)))
        print(phaseratios)
        if (RHO > RHO_CRIT) {
          print("one-phase field: liquid")
        }
        else if (RHO == RHO_CRIT) {
          print("critical density")
        }
        else if (RHO < RHO_CRIT) {
          print("one-phase field: vapor")
        }
    }
    else {
        RHO_brine <- predict(RHO.loess,data.frame(T=data1$Th,X=data1$X_brine))
        RHO_vapor <- predict(RHO.loess,data.frame(T=data1$Th,X=data1$X_vapor))
        phaseratios <-
rbind(data.frame(.Fortran("phasrat",X_NACL_BULK=as.double(data1$X_brine),RHO_BULK=as.double(RHO_brine),VPERCENT_HALITE=as.double(0),VP
ERCENT_SOL=as.double(0),VPERCENT_BUBBLE=as.double(0))),data.frame(.Fortran("phasrat",X_NACL_BULK=as.double(data1$X_vapor),RHO_BULK=
as.double(RHO_vapor),VPERCENT_HALITE=as.double(0),VPERCENT_SOL=as.double(0),VPERCENT_BUBBLE=as.double(0))))
        print(phaseratios)
    }
  }
```

```
}
#
#
# Given total depth, depth to the brittle-ductile transition, temperature, and bulk composition of aqueous fluids in the H2O-NaCl system,
# this function calculates the phase stability and fluid inclusion characteristics for inclusions trapped at the input conditions.
Predict_flinc_depth <- function(depth_total,depth_BD,T,X) {
  dyn.load("fortran/water_halite_equilibria.so")
  phaseratios <- NULL
  data<-read.csv(file="../../Documents/porphyry\ model/PVTXdata.csv",head=TRUE)
  RHO.loess <- loess(RHO ~ T + X, span=0.059, data.frame(RHO=data$RHO,T=data$T,X=data$X))
  P <- data.frame(.Fortran("litho_hydro_P",depth_total=as.double(depth_total),depth_BD=as.double(depth_BD),P=as.double(0)))$P
  data1 <-
data.frame(.Fortran("predict_Th",Pt=as.double(P),Tt=as.double(T),X_bulk=as.double(X),X_brine=as.double(0),X_vapor=as.double(0),Th=as.double(0),VAPOR
_PLUS_HALITE=as.double(0)))
  print(data1)
  if (data1$VAPOR_PLUS_HALITE == 1) {
    print("two-phase field: vapor + halite")
  }
  else if (data1$VAPOR_PLUS_HALITE == 0) {
    if (data1$X_brine < data1$X_bulk) {
          RHO <- predict(RHO.loess,data.frame(T=data1$Th,X=data1$X_bulk))
          T_CRIT <- data.frame(.Fortran("T_NaCl_crit",T=as.double(0),X=as.double(X)))$T
          RHO_CRIT <- data.frame(.Fortran("RHO_NaCl_crit",RHO=as.double(0),T=as.double(T_CRIT)))$RHO
          phaseratios <-
data.frame(.Fortran("phasrat",X_NACL_BULK=as.double(data1$X_bulk),RHO_BULK=as.double(RHO),VPERCENT_HALITE=as.double(0),VPERCENT_S
OL=as.double(0),VPERCENT_BUBBLE=as.double(0)))
          print(phaseratios)
          if (RHO > RHO_CRIT) {
            print("one-phase field: liquid")
          }
          else if (RHO == RHO_CRIT) {
            print("critical density")
          }
          else if (RHO < RHO_CRIT) {
            print("one-phase field: vapor")
          }
    }
    else {
          RHO_brine <- predict(RHO.loess,data.frame(T=data1$Th,X=data1$X_brine))
          RHO_vapor <- predict(RHO.loess,data.frame(T=data1$Th,X=data1$X_vapor))
```

```
        phaseratios <-
rbind(data.frame(.Fortran("phasrat",X_NACL_BULK=as.double(data1$X_brine),RHO_BULK=as.double(RHO_brine),VPERCENT_HALITE=as.double(0),VP
ERCENT_SOL=as.double(0),VPERCENT_BUBBLE=as.double(0))),data.frame(.Fortran("phasrat",X_NACL_BULK=as.double(data1$X_vapor),RHO_BULK=
as.double(RHO_vapor),VPERCENT_HALITE=as.double(0),VPERCENT_SOL=as.double(0),VPERCENT_BUBBLE=as.double(0))))
        print(phaseratios)
    }
  }
}
#
#
# Given total depth, depth to the brittle-ductile transition, temperature, and bulk composition of aqueous fluids in the H2O-NaCl system,
# this function calculates the phase stability and fluid inclusion characteristics for inclusions trapped at the input conditions.  The input format is an
# array of data in the following format: column 1 = label or designation, column 2 = total depth, column 3 = depth the to brittle-ductile transition,
# column 4 = temperature, and column 5 = bulk composition
# The function then writes two output files in csv format, the first describing the phase equilibria of fluids at the input points, and the second describing
# the characteristics of fluid inclusions trapped at the input conditions.
Predict_flinc_depth2 <- function(data) {
  dyn.load("fortran/water_halite_equilibria.so")
  phaseratios <- NULL
  data1 <- NULL
  phases <- NULL
  densitydata<-read.csv(file="../../Documents/porphyry\ model/PVTXdata.csv",head=TRUE)
  RHO.loess <- loess(RHO ~ T + X, span=0.059, data.frame(RHO=densitydata$RHO,T=densitydata$T,X=densitydata$X))
  for (i in 1:length(data$line)) {
    P <- data.frame(.Fortran("litho_hydro_P",depth_total=as.double(data[i,2]),depth_BD=as.double(data[i,3]),P=as.double(0)))$P
    data1 <-
rbind(data1,data.frame(.Fortran("predict_Th",Pt=as.double(P),Tt=as.double(data[i,4]),X_bulk=as.double(data[i,5]),X_brine=as.double(0),X_vapor=as.double(0),
Th=as.double(0),VAPOR_PLUS_HALITE=as.double(0))))
    if (data1[i,7] == 1) {
        phases <- rbind(phases,phases="V+H")
    }
    else if (data1[i,7] == 0) {
        if (data1[i,4] < data1[i,3]) {
          RHO <- predict(RHO.loess,data.frame(T=data1[i,6],X=data1[i,3]))
          T_CRIT <- data.frame(.Fortran("T_NaCl_crit",T=as.double(0),X=as.double(data1[i,3])))$T
          RHO_CRIT <- data.frame(.Fortran("RHO_NaCl_crit",RHO=as.double(0),T=as.double(T_CRIT)))$RHO

          phaseratios <-
rbind(phaseratios,data.frame(line=data[i,1],T=data[i,4],.Fortran("phasrat",X_NACL_BULK=as.double(data1[i,3]),RHO_BULK=as.double(RHO),VPERCENT_
HALITE=as.double(0),VPERCENT_SOL=as.double(0),VPERCENT_BUBBLE=as.double(0))))
```

```
            if (RHO > RHO_CRIT) {
              phases <- rbind(phases,phases="L")
            }
            else if (RHO == RHO_CRIT) {
              phases <- rbind(phases,phases="CRITICAL")
            }
            else if (RHO < RHO_CRIT) {
              phases <- rbind(phases,phases="V")
            }
          }
          else {
            phases <- rbind(phases,phases="L+V")
            RHO_brine <- predict(RHO.loess,data.frame(T=data1[i,6],X=data1[i,4]))
            RHO_vapor <- predict(RHO.loess,data.frame(T=data1[i,6],X=data1[i,5]))
            phaseratios <-
rbind(phaseratios,rbind(data.frame(line=data[i,1],T=data[i,4],.Fortran("phasrat",X_NACL_BULK=as.double(data1[i,4]),RHO_BULK=as.double(RHO_brine),V
PERCENT_HALITE=as.double(0),VPERCENT_SOL=as.double(0),VPERCENT_BUBBLE=as.double(0))),data.frame(line=data[i,1],T=data[i,4],.Fortran("phas
rat",X_NACL_BULK=as.double(data1[i,5]),RHO_BULK=as.double(RHO_vapor),VPERCENT_HALITE=as.double(0),VPERCENT_SOL=as.double(0),VPER
CENT_BUBBLE=as.double(0)))))
          }
      }
    }
    write.csv(cbind(line=data$line,data1,phases), file="porphyry_model_out.csv")
    write.csv(phaseratios,file="phaseratios_out.csv")
}
```